

**Insights to Magmatic–Hydrothermal Processes in the Manus back–arc Basin as
Recorded by Anhydrite**

Paul R. Craddock^{a,1*} and Wolfgang Bach^b

^a *Department of Marine Chemistry and Geochemistry, Woods Hole Oceanographic
Institution, 360 Woods Hole Road, McLean 201, MS#8, Woods Hole, MA 02543, USA*

^b *University of Bremen, Geosciences Department, Klagenfurter Straße, 28359 Bremen,
Germany.*

¹ *Present address: Origins Laboratory, Department of the Geophysical Sciences,
University of Chicago, 5734 South Ellis Avenue, Chicago, IL 60637, USA*

** Corresponding author. Email: craddock@uchicago.edu, Tel: (773) 834–3997*

Submitted to *Geochimica et Cosmochimica Acta*, July 12, 2009.

Submitted in revised version June 16, 2010.

ABSTRACT

1
2
3 Microchemical analyses of rare earth element (REE) concentrations and Sr and S isotope
4 ratios of anhydrite are used to identify sub-seafloor processes governing the formation of
5 hydrothermal fluids in the convergent margin Manus Basin, Papua New Guinea. Samples
6 comprise drill-core vein anhydrite and seafloor massive anhydrite from the PACMANUS
7 (Roman Ruins, Snowcap and Fenway) and SuSu Knolls (North Su) active hydrothermal
8 fields. Chondrite-normalized REE patterns in anhydrite show remarkable heterogeneity on
9 the scale of individual grains, different from the near uniform REE_N patterns measured in
10 anhydrite from mid-ocean ridge deposits. The REE_N patterns in anhydrite are correlated
11 with REE distributions measured in hydrothermal fluids venting at the seafloor at these
12 vent fields and are interpreted to record episodes of hydrothermal fluid formation affected
13 by magmatic volatile degassing. ⁸⁷Sr/⁸⁶Sr ratios vary dramatically within individual grains
14 between that of contemporary seawater and that of endmember hydrothermal fluid.
15 Anhydrite was precipitated from a highly variable mixture of the two. The intra-grain
16 heterogeneity implies that anhydrite preserves periods of contrasting hydrothermal- versus
17 seawater-dominant near-seafloor fluid circulation. Most sulfate δ³⁴S values of anhydrite
18 cluster around that of contemporary seawater, consistent with anhydrite precipitating from
19 hydrothermal fluid mixed with locally entrained seawater. Sulfate δ³⁴S isotope ratios in
20 some anhydrites are, however, lighter than that of seawater interpreted as recording a
21 source of sulfate derived from magmatic SO₂ degassed from underlying felsic magmas in
22 the Manus. The range of elemental and isotopic signatures observed in anhydrite records a

23 range of sub-seafloor processes including high-temperature hydrothermal fluid
24 circulation, varying extents of magmatic volatile degassing, seawater entrainment and fluid
25 mixing. The chemical and isotopic heterogeneity recorded in anhydrite at the inter- and
26 intra-grain scale captures the dynamics of hydrothermal fluid formation and sub-seafloor
27 circulation that is highly variable both spatially and temporally on timescales over which
28 hydrothermal deposits are formed. Microchemical analysis of hydrothermal minerals can
29 provide information about the temporal history of submarine hydrothermal systems that are
30 variable over time and cannot necessarily be inferred only from the study of vent fluids.

31

1. INTRODUCTION

32

33

34 The formation and composition of submarine hydrothermal fluids and related mineral
35 deposits at mid-ocean ridges and in island-arc/back-arc basins are variably affected by a
36 range of sub-seafloor geochemical processes including (1) fluid-rock interaction (Bischoff
37 and Dickson, 1975; Humphris and Thompson, 1978; Mottl and Holland, 1978; Seyfried,
38 1987), (2) fluid phase separation-segregation, which is function of local pressure and
39 temperature conditions and the evolutionary state of the hydrothermal system (Von Damm,
40 1995; Von Damm et al., 1997), (3) sub-surface mixing between rising high-temperature
41 hydrothermal fluid and locally entrained seawater (Edmond et al., 1995; Tivey et al.,
42 1995), and (4) input of magmatic volatiles with a range of composition from CO₂ at mid-
43 ocean ridges to SO₂-CO₂-HCl-HF at back-arc basins (Butterfield et al., 1990; Gamo et
44 al., 1997; Seewald et al., 2006). Owing to limited access beneath the sub-seafloor, our
45 understanding of these processes occurring at depth is inferred, in large part, from
46 geochemical studies of vent fluids and/or related mineral deposits recovered at, or close to,
47 the seafloor. Anhydrite (CaSO₄) is recognized as an important constituent of submarine
48 hydrothermal deposits, occurring within individual vent chimneys (Goldfarb, 1982;
49 Haymon, 1983) and as veins and massive concretions in seafloor sulfide deposits
50 (Humphris et al., 1995; Tivey et al., 1995). Anhydrite exhibits retrograde solubility and
51 precipitates from seawater at temperatures above ~ 150 °C (at seafloor pressures) from
52 either conductive heating of seawater or mixing between seawater and high-temperature
53 hydrothermal fluid (Bischoff and Seyfried, 1978). Widespread sub-seafloor precipitation

54 of anhydrite owing to fluid mixing can provide a record of hydrothermal fluid evolution
55 and circulation in the absence of contemporary fluid activity.

56

57 Abundant massive anhydrite was first observed and sampled along a mid-ocean ridge
58 spreading center at the Trans-Atlantic Geotraverse (TAG) active hydrothermal mound, 26
59 °N, Mid-Atlantic Ridge (Thompson et al., 1988). Drilling of the mound (Ocean Drilling
60 Program, Leg 158) recovered abundant anhydrite to depths of ~ 200 meters below the
61 seafloor (mbsf) (Humphris et al., 1995). Trace element (e.g., rare earth element, REE),
62 isotopic (e.g., Sr, S) and fluid inclusion studies of anhydrite provided evidence for
63 substantial entrainment of seawater in the mound, conductive heating of seawater and
64 mixing between rising hydrothermal fluid and entrained seawater (Chiba et al., 1998;
65 Humphris, 1998; Mills et al., 1998; Teagle et al., 1998; Tivey et al., 1998; Humphris and
66 Bach, 2005). Sub-seafloor mixing has influenced significantly sulfide mineralization and
67 composition of the TAG mound, owing to precipitation of Fe- and Cu-Fe-sulfides and
68 generation of secondary fluid acidity during fluid mixing, coupled with dissolution of
69 previously deposited Zn-sulfides in a process of zone-refinement (Tivey et al., 1995).

70

71 More recently, anhydrite has been recovered from the Papua New Guinea-Canada-
72 Australia-Manus (PACMANUS) hydrothermal system located within a convergent margin
73 (Manus back-arc basin, Papua New Guinea). Anhydrite samples were recovered sub-
74 seafloor to depths ~ 300 meters via drilling (Ocean Drilling Program, Leg 193) of the
75 PACMANUS hydrothermal system and include anhydrite as matrix within hydrothermal

76 breccia, as well-developed veins often greater than 10 mm thick, and locally as more
77 massive anhydrite in pore space (Binns et al., 2007). Whole-rock element (REE) and
78 isotopic ($^{87}\text{Sr}/^{86}\text{Sr}$, $\delta^{34}\text{S}$) studies of different anhydrite separates have enabled the sub-
79 seafloor processes associated with formation of hydrothermal fluids and mineral deposits
80 in back-arc basins and at mid-ocean ridge spreading centers to be compared and
81 contrasted (Bach et al., 2003; Roberts et al., 2003; Bach et al., 2005). The wide range of
82 whole-rock REE patterns and S isotopic compositions recorded in anhydrite at
83 PACMANUS differs markedly to near uniform REE patterns and S isotopic compositions
84 preserved in anhydrite from the TAG mound. These signatures have been interpreted to
85 reflect variable degassing of magmatic acid volatiles (H_2O – CO_2 – SO_2 – HCl – HF) from
86 water-rich and relatively oxidized magmas above subducted plate margins.

87

88 To date, most studies of anhydrite have used whole-rock chemical measurements of
89 homogenized samples obtained from mineral separates. This approach has two limitations;
90 (1) it is difficult to integrate multiple geochemical data obtained from bulk analysis of
91 mineral separates because these data may be obtained from genetically unrelated mineral
92 grains and (2) mineral separation and sample homogenization may destroy potential
93 chemical heterogeneity and information about the history of mineral formation. This study
94 presents directly coupled and texturally-constrained microchemical analytical data to
95 better characterize the processes governing hydrothermal fluid and vent deposit formation
96 in the Manus Basin. Geochemical data for seafloor hydrothermal fluids sampled at the
97 same time and same areas as anhydrite are used as a reference point for evaluating mineral

98 chemical signatures. The ability to use minerals as a recorder of sub-seafloor hydrothermal
99 processes has particular importance for studies of relict systems where fluids are no longer
100 present and information pertaining to the evolution of the deposit is preserved only in
101 minerals.

102

103

2. GEOLOGIC SETTING

104

2.1. Regional Setting

105

106
107 The Manus Basin in the Bismarck Sea, Papua New Guinea (Fig. 1) is a rapidly-opening (~
108 100 mm/yr) back-arc basin associated with subduction of the Solomon Microplate beneath
109 the New Britain arc (Taylor, 1979; Davies et al., 1987; Martinez and Taylor, 1996). Crustal
110 rifting and spreading occurs along several distinct lineations, including the Extensional
111 Transform Zone, Manus Spreading Center and the Eastern Manus Basin (Martinez and
112 Taylor, 1996). The Eastern Manus Basin (EMB) is bounded by the Djaul and Weitin
113 Transform Faults. Rapid spreading in the EMB is accommodated primarily by rifting and
114 extension of pre-existing island arc crust. Lavas are erupted as a series of discrete *en*
115 *echelon* neovolcanic ridges and volcanic cones of felsic composition (andesite-to-rhyolite)
116 exhibiting distinct arc-affinity (Sinton et al., 2003). The EMB hosts several active
117 hydrothermal systems, including PACMANUS (Binns and Scott, 1993; Scott and Binns,
118 1995) and SuSu Knolls (Binns et al., 1997), the deposits of which are examined in this
119 study.

120

121 **2.2. PACMANUS Hydrothermal Field**

122

123 The PACMANUS hydrothermal system (Fig. 2a) is located on the crest of the 35–km long,
124 500–m high Pual Ridge at water depths between 1650 and 1740 m (Binns and Scott, 1993).

125 Hydrothermal activity occurs at several discrete fields, each of the order 50 to 200 m in

126 diameter, along a 3 km long section of Pual Ridge (Binns and Scott, 1993; Binns et al.,

127 2007; Tivey et al., 2007). Abundant anhydrite has been recovered from three vent fields.

128 Samples of anhydrite were recovered sub–seafloor from Roman Ruins and Snowcap by

129 drilling during ODP Leg 193 (Binns et al., 2007). Samples of massive anhydrite currently

130 exposed on the seafloor at Fenway were recovered by surface grab sampling using ROV

131 Jason II during cruise MGLN06MV (Tivey et al., 2007).

132

133 The Roman Ruins vent field (~1680 m depth) is characterized by numerous discrete

134 columnar chimneys and clusters of multi–spired chimneys typically 5 to 7 m in height,

135 overlying mostly fresh volcanic outcrop. Fluids discharging from black- and gray-smoker

136 chimneys have measured temperatures between 270 and 341 °C and pH (25 °C) in the

137 range 2.3 to 2.6 (Seewald et al., 2006; Craddock et al., 2010; Reeves, 2010). Diffuse fluids,

138 with temperatures ranging from 54 to 106 °C, discharge from fissures within the volcanic

139 basement and through chimney and volcanic talus in areas surrounding sulfide deposits.

140 Mineralization of sampled sulfides is dominated by chalcopyrite in open conduit, black

141 smoker chimneys venting the highest temperature (≥ 300 °C) fluids and by Cu–Fe sulfides

142 (chalcopyrite + bornite ± covellite), Cu-sulfosalts (tennantite) and relatively minor Zn-
143 sulfides (sphalerite) in diffuser-type chimneys venting lower temperature (~270 °C) fluids
144 (Craddock, 2009). Drilling of the Roman Ruins deposit and underlying basement (Holes
145 1189A and 1189B) recovered volcanic rocks and hydrothermal material to a depth of ~200
146 mbsf (Binns et al., 2007). Except for relatively fresh lava flows recovered near the seafloor
147 (< 30 mbsf), most volcanic rocks display moderate-to-extensive alteration that continues
148 to the base of drill core. Alteration is primarily argillaceous (smectite-chlorite ± illite)
149 (Yeats et al., 2001; Lackschewitz et al., 2004). Hydrothermal stockwork is present to
150 depths ~120 mbsf and is dominated by disseminated and locally veined pyrite (Binns et al.,
151 2007). Anhydrite is a minor mineral interspersed throughout drill core, occurring mostly as
152 fine-grained disseminated matrix and locally as more massive anhydrite veins in both
153 hydrothermal stockwork and alteration assemblages (Fig. 3a).

154

155 Present day hydrothermal activity at Snowcap (~1645 m depth) is characterized by low
156 temperature fluid discharge (152 and 180 °C) through bulbous, diffuser-type chimneys
157 across heavily-sedimented and altered terrain (Tivey et al., 2007). The pH (25 °C) of
158 sampled vent fluids ranges from 3.4 to 4.6 (Seewald et al., 2006; Craddock et al., 2010;
159 Reeves, 2010). The sulfide composition of chimneys venting low temperature fluids is
160 predominantly bornite (± chalcopyrite) and tennantite with minor sphalerite (Craddock,
161 2009). Surface outcrops of fresh massive lava flows are rare. Instead, hyaloclastite flows,
162 volcanoclastic sediments, rocks affected by advanced argillic alteration, native sulfur and
163 presumed microbial mats are common (Yeats et al., 2000; Tivey et al., 2007). Drilling

164 recovered core from two holes (Holes 1188A and 1188F) down to depths of 210 and 390
165 mbsf, respectively (Binns et al., 2007). Petrographic analyses indicate extensive and multi-
166 stage alteration, including alternating argillaceous (smectite–chlorite–albite) and feldspar-
167 destructive (illite–pyrophyllite–quartz/cristobalite) alteration (Yeats et al., 2001;
168 Lackschewitz et al., 2004). The occurrence of illite–pyrophyllite and native sulfur at the
169 seafloor at Snowcap (Yeats et al., 2000; Tivey et al., 2007) implies crustal rock alteration
170 by highly acidic (pH < 2 to 3) and sulfate–rich fluids (Meyer and Hemley, 1967; Hemley et
171 al., 1969; Brimhall and Ghiorso, 1983). Anhydrite occurs throughout drill core to depths of
172 at least 350 mbsf as both composite veins and as matrix within brecciated and
173 hydrothermally altered rocks and does not appear associated within any single stage of
174 alteration.

175

176 At Fenway, the seafloor is dominated by a central, two–tiered mound approximately 40 m
177 in diameter and 18 m in relief (Tivey et al., 2007). The summit of the mound at a water
178 depth ~1705 m is composed of an extensive black smoker complex with fluids venting
179 vigorously at temperatures up to 358 °C (boiling temperature at ambient pressures) and pH
180 (25 °C) ~2.3 to 2.7 (Seewald et al., 2006; Craddock et al., 2010; Reeves, 2010). Rock
181 sampling of the black smoker complex recovered chalcopyrite–rich open conduit chimneys
182 (Craddock, 2009). The slopes of mound are covered by extensive sulfide chimney debris
183 and talus, outcrops of massive anhydrite, and coarse anhydrite rubble within hydrothermal
184 sediment (Fig 3b). Lower temperature focused fluid venting from chimneys (~284 °C) and
185 diffuse fluid venting from fissures and brecciated sediment (~78 °C) are common from

186 lower tiers and slopes of the mound. Several samples of massive anhydrite were recovered
187 from the seafloor (Tivey et al., 2007). Samples from Fenway are large (~5 to 10 kg) and
188 coarse-grained with no obvious crystallographic zoning. The large size and coarse-grained
189 texture suggest that massive anhydrite was likely precipitated within a large cavity that was
190 open to hydrothermal flow from beneath and capped by less porous and permeable sulfide-
191 sulfate. Collapse of the overlying cap (as supported by the extent of sulfide-sulfate debris
192 across the Fenway mound) exposed massive anhydrite as the seafloor. No anhydrite has
193 been sampled from beneath the seafloor at this vent field.

194

195 **2.3. SuSu Knolls Hydrothermal Field**

196

197 The SuSu Knolls vent area (Fig 2b) is located ~45 km east of PACMANUS and consists of
198 three primary areas of activity (North Su, South Su and Suzette) located on individual
199 volcanic structures at water depths between ~1140 and 1510 m (Binns et al., 1997).
200 Seafloor rocks are composed of vesicular dacite flows and hyaloclastite, overlain by
201 hydrothermal talus and sediment, native sulfur flows and locally extensive sulfide deposits
202 (Binns et al., 1997; Tivey et al., 2007). At North Su, hydrothermal activity on the flanks of
203 the volcano (~1260 m depth) is dominated by vigorous discharge of yellow-white fluids
204 (Seewald et al., 2006; Craddock et al., 2010; Reeves, 2010). In the vicinity of active
205 venting, native sulfur oozes through volcanic and hydrothermal sediments. The fluids have
206 exit temperatures between 48 and 215 °C, are highly acidic with measured pH (25 °C)
207 ranging from 0.9 to 1.8, and are rich in sulfate. This acid-sulfate fluid venting contrasts

208 markedly with fluid discharge at the summit of the North Su mound (~1160 m depth),
209 which is dominated by venting of high-temperature black smoker fluids (T = 296 to 325
210 °C; pH (25 °C) = 2.8 to 3.4) from multi-spired sulfide chimney complexes up to ~11 m tall
211 (Seewald et al., 2006; Craddock, 2009; Reeves, 2010). The composition of chimneys
212 sampled from the black smoker complex is predominantly monomineralic chalcopyrite
213 lining open conduits, whereas tennantite, bornite and lesser chalcopyrite are present in the
214 few diffuser-type chimneys recovered from the North Su vent field (Craddock, 2009).
215 Exposed massive anhydrite was sampled near the base of the black smoker summit
216 complex (water depth ~1190 m) from which 325 °C black smoker fluids were sampled.
217 This sample exhibits complex textures, including crustiform layering of anhydrite veins
218 (Fig. 3c).

219

220

3. METHODS

221

3.1. Sample Collection and Preparation

222

223
224 Anhydrite analyzed during this study was recovered from beneath the seafloor at Roman Ruins and
225 Snowcap (Binns et al., 2007) and at the seafloor from Fenway and North Su (Tivey et al., 2007).
226 Twelve drill core samples were selected from Roman Ruins and Snowcap to provide a
227 representative down core profile of anhydrite from different lithologic units and textural settings,
228 including a variety of veins, composite and cross-cutting growth bands and more massive
229 anhydrite filling vugs and pore spaces. Eight seafloor massive anhydrite samples were also studied

230 and include seven samples from the flanks of the Fenway mound and a single sample from the base
231 of the black smoker complex at North Su.

232

233 Samples were prepared by one of two methods. Massive anhydrite samples were initially sub-
234 sampled using a tile saw and/or a Buehler Micromet saw. Working sections were impregnated with
235 epoxy resin and cut into thin (~ 2 mm) wafers. These wafers were polished on both sides and
236 mounted onto standard 45 x 25 mm petrographic slides for analysis. Six drill-core anhydrite
237 samples were provided by D. Vanko at the University of Towson, Maryland and were prepared
238 using the method described above. A further six small samples of drill-core anhydrite were
239 mounted with epoxy in 25 mm aluminum rings, cut to obtain a flat surface and polished on the flat
240 side for analysis.

241

242 **3.2 Analytical methods**

243

244 *3.2.1 Cathodoluminescence Imaging*

245

246 Cathodoluminescence (CL) reconnaissance imaging was performed to obtain semi-quantitative
247 trace element distributions within each sample. In particular, CL imaging was used to differentiate
248 chemical heterogeneities (e.g., crystal zoning) occurring within and between individual anhydrite
249 crystals, which would be a focus for subsequent quantitative microchemical analyses. Under
250 excitation by a cathode beam, trivalent REEs (Sm^{3+} and Dy^{3+}) fluoresce and emit intense spectra
251 within visible wavelengths with varying shades of tan (Marshall, 1988). CL was mapped using a
252 Nuclide Corporation ELM-2B cold cathode generator, operated at ~ 10 keV and 0.8 mA and with a
253 vacuum of 70 – 85 μtorr . Sample were photographed using a Nikon D1x digital camera, mounted

254 to a Nuclide Corporation ELM-2E microscope with 10x – 40x magnification. Photographs were
255 captured using white balance set to fluorescent light and exposure times of 30 seconds.
256 Photomosaics were generated using digital imaging software (Adobe Photoshop CS2).

257

258 *3.2.2. Rare Earth Element Analysis by in situ LA-ICPMS*

259

260 Analyses were coordinated so that elemental and isotopic data were collected from adjacent areas
261 within the same heterogeneous domains as identified by CL. Elemental and isotopic data are
262 directly related spatially and texturally, and the full chemical heterogeneity as identified by CL
263 imaging is captured. Microchemical rare earth element (REE) analyses of anhydrite were
264 performed using laser ablation-inductively coupled plasma-mass spectrometry (LA-ICPMS) at
265 both the Woods Hole Oceanographic Institution (WHOI) and the University of Bremen. Identical
266 LA-ICPMS protocols were used at both institutions (Table 1). Samples were loaded onto a
267 NewWave UP213 laser microprobe coupled to a Thermo Scientific ELEMENT2 ICPMS. ICPMS
268 parameters were configured each session to obtain optimum signal stability and intensity. The laser
269 was operated in apertured mode with a beam diameter of 30 μm . The area of sample ablated
270 measured 80 by 180 μm with a line spacing of 15 μm (total of 13 lines). Beam scan speeds of 60
271 $\mu\text{m}/\text{sec}$ and 20 $\mu\text{m}/\text{sec}$ were used in pre-ablation and ablation modes, respectively. Total analysis
272 time for a single measurement, including baseline analysis, pre-ablation/ablation data acquisition
273 and wash-out, was on the order of 4 minutes. The area of ablation and the spatial resolution
274 obtained by elemental analysis was constrained to be the same as the minimum area of ablation
275 required for precise Sr and S isotopic analysis; a smaller area of ablation for elemental analysis
276 (less than 80 \times 80 μm) could be used in the absence of coupled in situ isotopic analysis.

277

278 Rare earth elements were measured in low mass resolution mode on the following isotopes: ^{139}La ,
279 ^{140}Ce , ^{146}Nd , ^{147}Sm , ^{151}Eu , ^{153}Eu , ^{158}Gd , ^{163}Dy , ^{167}Er and ^{173}Yb . Data were not collected for Pr, Tb,
280 Tm and Lu owing to their relatively low abundance, but typically similar geochemical behavior,
281 relative to neighboring REEs (i.e., their abundance can be estimated by interpolation between
282 neighboring REEs on a chondrite-normalized plot). Instrumental sensitivity varied among REEs
283 but was on the order $\sim 9,000$ to $10,000$ cps per ppm REE. The following other elements were
284 measured simultaneously with the REEs in low mass resolution: ^{25}Mg , ^{43}Ca , ^{48}Ca , ^{86}Sr , ^{135}Ba and
285 ^{137}Ba . Owing to the high concentration of Ca in both anhydrite and the normalizing standard
286 SRM612, Ca was measured on low abundance isotopes free of isobaric interference (e.g., ^{40}Ar on
287 abundant ^{40}Ca). The formation of interfering oxides of the REEs (e.g., $^{143}\text{Nd}^{16}\text{O}^+$ on $^{159}\text{Tb}^+$) and
288 other elements (e.g., $^{135}\text{Ba}^{16}\text{O}^+$ on $^{151}\text{Eu}^+$, $^{137}\text{Ba}^{16}\text{O}^+$ on $^{153}\text{Eu}^+$) can impede the accurate
289 measurement of REEs. The formation of REE-oxides was suppressed under dry plasma conditions
290 as confirmed by the measurement of mono-elemental Ce standard solution by ICPMS using a
291 Cetac Aridus® desolvating unit ($\text{CeO}^+/\text{Ce}^+ < 0.01$ to 0.04) (see also Craddock et al., 2010).
292 Possible interferences on Eu from BaO^+ were assessed by monitoring simultaneously isotopes ^{151}Eu
293 and ^{153}Eu . Significant interference from Ba would decrease the measured $^{151}\text{Eu}/^{153}\text{Eu}$ ratio from the
294 natural ratio ~ 0.916 toward the natural $^{135}\text{Ba}/^{137}\text{Ba}$ ratio ~ 0.587 . There was no correlation
295 observed between either Ba concentration versus Eu concentration or Ba concentration versus
296 $^{151}\text{Eu}/^{153}\text{Eu}$ ratio, indicating that Ba-oxide did not interfere on or affect Eu analysis. The measured
297 $^{151}\text{Eu}/^{153}\text{Eu}$ ratios of all (~ 500) analyses show a normal distribution with mean (μ) = 0.928 ± 0.012
298 (2σ). The certified reference material NIST SRM612 was used as the standard for trace element
299 calibration (Pearce et al., 1997; Kent et al., 2004). The absolute concentration of REEs in SRM612
300 are similar (~ 40 ppm), but typically higher than that measured in anhydrite. The concentrations of
301 REE in the standard are, however, within the overall range of REE concentrations measured.

302 Internal normalization was carried out by measuring Ca in both the standard and samples. The Ca
303 concentrations of the NIST SRM612 standard and of anhydrite samples are 11.93 ± 0.22 wt% CaO
304 (8.53 ± 0.16 wt% Ca) (Pearce et al., 1997) and 41.18 wt% CaO (29.44 wt% Ca), respectively.
305 Chondritic data used for external REE normalization are from Anders and Grevesse (1989).
306 Reproducibility of the method is typically 10 % (1σ).

307

308 *3.2.3. Strontium and sulfur isotope analysis by in situ LA-MC-ICPMS*

309

310 In situ S and Sr isotope analyses were performed at WHOI using a Thermo Scientific NEPTUNE
311 multi-collector ICPMS coupled to a NewWave UP213 laser microprobe. Sulfur isotopes ($\delta^{34}\text{S}$)
312 were measured using the analytical procedure developed by Craddock et al. (2008), with typical
313 instrumental operating parameters as listed in Table 1. The area of sample ablated measured 80 by
314 $180 \mu\text{m}$ with a line spacing of $15 \mu\text{m}$ (total of 13 lines). Beam scan speeds of $30 \mu\text{m}/\text{sec}$ and 5
315 $\mu\text{m}/\text{sec}$ were used in pre-ablation and ablation modes, respectively. Data acquisition was started
316 once a stable S ablation signal was obtained and consisted of 20 cycles with each cycle having 8.5
317 second integration corresponding to an acquisition time of ~ 170 seconds. Total analysis time for a
318 single measurement, including baseline analysis, pre-ablation/ablation and wash-out, was on the
319 order of 8 minutes. Sulfur isotopes were measured on masses ^{32}S , ^{33}S and ^{34}S . Isobaric interferences
320 (principally from molecular O_2^+ species) were resolved by operating the instrument with high mass
321 resolution. Background contributions were measured by aspirating 2% nitric acid blanks and
322 corrected by on-peak baseline subtraction. The standard-sample bracketing method (Belshaw et
323 al., 1998) was employed to calibrate unknown samples against isotopically characterized sulfur
324 standards. Instrumental mass bias was calculated for the S isotopic standard using the exponential
325 mass law and a correction applied to the unknown sample using linear interpolation of calculated

326 mass biases from bracketing standards. The signal intensities of samples and bracketing standards
327 were optimized within $\pm 10\%$ to minimize the corrections necessary from background
328 contributions. External reproducibility of the reported $\delta^{34}\text{S}$ value is $\pm 0.45\%$ (2σ) for laser ablation
329 analysis.

330

331 Strontium isotopic ratios ($^{87}\text{Sr}/^{86}\text{Sr}$) in anhydrite were measured following a modified procedure
332 from Hart et al. (2005). Sample ablation and data acquisition parameters for analysis of Sr isotopes
333 were identical as that for the analysis of S isotopes described above (Table 1). Strontium isotopes
334 (^{84}Sr , ^{86}Sr , ^{87}Sr and ^{88}Sr) were measured in low mass resolution mode. Possible isobaric
335 interferences on masses ^{84}Sr , ^{86}Sr and ^{87}Sr from ^{84}Kr , ^{86}Kr and ^{87}Rb , respectively, were monitored
336 and corrected by measuring Kr on mass 82 and 83 and Rb on mass 85 (Hart et al., 2005). In all
337 cases, ^{82}Kr , ^{83}Kr and ^{85}Rb signals were < 1 mV and corrections were negligible. The reference
338 material NIST SRM987 was used as the external Sr isotopic standard (consensus $^{87}\text{Sr}/^{86}\text{Sr}$ ratio =
339 0.710248 ± 0.000003). Instrumental mass bias was calculated from deviation of the measured
340 $^{86}\text{Sr}/^{88}\text{Sr}$ ratio from the canonical isotopic ratio in the standard ($^{86}\text{Sr}/^{88}\text{Sr} = 0.119400$) and a mass
341 bias correction applied to measured $^{87}\text{Sr}/^{86}\text{Sr}$ ratios using the exponential mass law. The calculated
342 mass bias correction was then applied to the unknown anhydrite sample assuming linear
343 interpolation of mass bias between replicate standards. Background contributions were measured
344 periodically as on-peak baselines and were sufficiently low that blank corrections were
345 significantly less than analytical uncertainties. Long-term reproducibility of $^{87}\text{Sr}/^{86}\text{Sr}$ isotope ratios,
346 as determined by repeat analysis of an aragonite coral (Sclerosponge 'in-house' standard), was
347 better than 20 ppm ($^{87}\text{Sr}/^{86}\text{Sr}_{\text{consensus}} = 0.70918 \pm 0.00002$ vs. $^{87}\text{Sr}/^{86}\text{Sr}_{\text{measured}} = 0.70919 \pm 0.00002$; n
348 = 15, 2σ uncertainty).

349

4. RESULTS

350

351

352 Elemental (rare earth element, Mg, Sr, Ba) and isotopic ($^{87}\text{Sr}/^{86}\text{Sr}$, $\delta^{34}\text{S}$) data are reported
353 for twelve drill core anhydrites (8 from Snowcap, 4 from Roman Ruins) and eight seafloor
354 massive anhydrites (7 from Fenway, 1 from North Su). In total, approximately 500 multi-
355 element analyses and 300 isotopic analyses were carried out. A complete data report is
356 provided in the Supporting Online Material (Table S1).

357

4.1. Rare Earth Element Contents in Anhydrite

358

359
360 Microchemical laser-ablation ICPMS and cathodoluminescence mapping of anhydrite
361 document significant heterogeneity in both REE concentrations and chondrite-normalized
362 REE_N distribution patterns (Figs. 4–7). This heterogeneity contrasts markedly with near
363 uniform REE_N distribution patterns of anhydrite sampled from mid-ocean ridge
364 hydrothermal systems, which show a general light-REE enrichment and positive Eu-
365 anomaly (e.g., Humphris, 1998; Mills et al., 1998; Humphris and Bach, 2005). Notably,
366 the variability in REE concentration and pattern occurs on multiple spatial scales, from
367 large-scale differences between anhydrite recovered from different hydrothermal areas to
368 sub-millimeter intra-grain heterogeneity (Figs. 8–10). This fine-scale variability cannot be
369 resolved from whole-rock chemical analysis.

370

371 Chondrite-normalized REE_N patterns of anhydrite samples from Roman Ruins (ODP Hole
372 1189A, B) are variably light-REE enriched. Most grains exhibit a positive Eu-anomaly,
373 but some REE-rich grain domains have a pronounced negative Eu-anomaly ($La_N/Yb_N =$
374 $7.8 - 108$, $Sm_N/Yb_N = 2.8 - 23$, $Eu_N/Eu_N^* = 0.4 - 6.5$; Figs. 4, 8). REE_N patterns are similar
375 among samples recovered from a range of depths from 20 to 158 meters below seafloor
376 (mbsf), except for the pronounced negative Eu-anomaly that is restricted to anhydrite
377 recovered from 158 m depth.

378

379 Anhydrite samples from Snowcap (ODP Hole 1188A, F) exhibit a range of REE_N patterns
380 including light-REE enrichment, light-REE depletion/heavy-REE enrichment and flat
381 REE_N patterns with both positive and negative Eu-anomalies ($La_N/Yb_N = 0.3 - 74$,
382 $Sm_N/Yb_N = 0.9 - 12.5$, $Eu_N/Eu_N^* = 0.5 - 14.3$; Fig. 5). REE_N patterns are generally similar
383 on the sub-millimeter scale within individual grains, but differ markedly between grains
384 and samples recovered from different depths. There is no clear correlation, however,
385 between the REE composition of anhydrite and the depth or lithologic unit from which
386 anhydrite was recovered.

387

388 Seven massive anhydrites recovered from Fenway all exhibit a similar REE_N pattern
389 characterized by light-REE enrichment and a positive Eu-anomaly ($La_N/Yb_N = 3.2 - 76$,
390 $Sm_N/Yb_N = 3.0 - 32$, $Eu_N/Eu_N^* = 2.6 - 23$; three of seven examples are shown in Fig. 6).
391 This relative homogeneity is preserved at both the inter- and intra-grain scale (Fig. 10).
392 The range of individual REE concentrations measured in massive anhydrite spans nearly

393 two orders of magnitude, but is considerably less than the range observed in drill core
394 samples. In contrast, the REE_N pattern of the composite layered massive anhydrite
395 recovered from North Su (SuSu Knolls) is variable, ranging from slightly light-REE
396 enriched to notable heavy-REE enriched both with a range of positive Eu-anomalies
397 ($\text{La}_N/\text{Yb}_N = 0.1 - 1.8$, $\text{Sm}_N/\text{Yb}_N = 0.6 - 4.6$, $\text{Eu}_N/\text{Eu}_N^* = 1.4 - 8.0$; Fig. 7). This
398 heterogeneity is recorded primarily between different grains, but some heterogeneity is
399 also apparent at the intra-grain scale (Fig. 10).

400

401 **4.2. Strontium Isotope Ratios**

402

403 Overall, Sr isotope ratios in anhydrite ($^{87}\text{Sr}/^{86}\text{Sr}$) range from 0.70429 to 0.70881 (Fig. 11)
404 and show significant variability on the inter- and intra-grain scale in both PACMANUS
405 and SuSu Knolls samples. The wide range of Sr isotopic ratios imply anhydrite
406 precipitated from a wide range of seawater ($^{87}\text{Sr}/^{86}\text{Sr} = 0.70918$) and end-member
407 hydrothermal fluid mixtures. The Sr isotope ratio of end-member black-smoker vent
408 fluids is significantly less radiogenic than seawater ($^{87}\text{Sr}/^{86}\text{Sr} \sim 0.7042$ at Roman Ruins and
409 Fenway, $^{87}\text{Sr}/^{86}\text{Sr} \sim 0.7044$ at North Su; Table 2) consistent with extensive reaction and Sr
410 isotopic exchange with underlying crustal rocks ($^{87}\text{Sr}/^{86}\text{Sr} \sim 0.7035$; Sinton et al., 2003).
411 Where data exist, microchemical data are compared against Sr isotope ratios for the same
412 anhydrite samples determined using whole-rock isotopic analysis (Roberts et al., 2003;
413 Bach et al., 2005). In general, the data show excellent agreement (Fig. 11). However,
414 microchemical analyses reveal significant intra-grain variability that could not be

415 identified by whole-rock isotope analysis, and extend the overall range of Sr isotope ratios
416 measured. The relative proportions of hydrothermal fluid and seawater in fluids from
417 which anhydrite was precipitated at PACMANUS and SuSu Knolls can be calculated
418 following standard isotope mixing calculations using measured Sr isotopic ratios (e.g.,
419 Mills et al., 1998). These calculations assume that uptake of Sr into anhydrite follows
420 batch mixing and does not fractionate Sr isotopes, and that Sr compositions of modern
421 seawater and hydrothermal fluid used in mixing calculations (Table 2) are representative of
422 fluids from which anhydrite precipitated.

423

424 Strontium isotope ratios of drill-core anhydrites from Roman Ruins cluster mostly
425 between 0.7055 and 0.7080, but range from 0.70429 to 0.70822 (Fig. 11). Significant Sr
426 isotopic heterogeneity is observed at the intra-grain scale (Fig 8). Isotope mixing
427 calculations indicate that anhydrite precipitated mostly from fluid mixtures containing
428 between 17 and 68 vol. % hydrothermal fluid. However, the heterogeneous distribution of
429 Sr isotope ratios at the intra-grain scale implies that hydrothermal fluids in some instances
430 contributed up to 95 vol. % of fluid from which anhydrite was precipitated, particularly in
431 samples recovered near the base of drill core (~ 158 mbsf). Strontium isotopic
432 compositions are typically well correlated with REE concentrations of the same grains
433 (Fig. 8); REEs in anhydrite are contributed by hydrothermal fluid.

434

435 At Snowcap, Sr isotope ratios of drill-core anhydrite recovered from < 50 mbsf are near
436 that of seawater (sample 193-1188A-7R-1; $^{87}\text{Sr}/^{86}\text{Sr} \sim 0.7088$), but in samples recovered

437 from greater depths cluster around lower ratios ($^{87}\text{Sr}/^{86}\text{Sr} \sim 0.7050$ to 0.7075 ; Fig. 11).
438 Although the total range of $^{87}\text{Sr}/^{86}\text{Sr}$ ratios is less than that documented at Roman Ruins,
439 significant variability is observed on sub-centimeter scales within many samples. The Sr
440 isotopic compositions of most Snowcap anhydrite samples correspond to between 35 and
441 77 vol. % of hydrothermal fluid in the aqueous mixture. The exception is the shallow
442 sample (193-1188A-7R-1), whose radiogenic Sr isotopic composition indicates
443 precipitation of anhydrite from a fluid contributed by < 10 vol. % hydrothermal fluid.
444
445 Massive anhydrites from Fenway have Sr isotopic compositions between 0.7060 and
446 0.7082 (Fig. 11). In most instances, the data indicate anhydrite precipitation from fluid
447 mixtures dominated by seawater (~ 55 to 84 vol. %). Locally, greater contribution of
448 hydrothermal fluid to the fluid mix precipitating anhydrite (up to vol. 60 % hydrothermal
449 fluid) is observed. At North Su (SuSu Knolls), Sr isotope ratios recorded in a single
450 anhydrite sample are remarkably variable, ranging from 0.7046 to 0.7085 (Fig. 11) and
451 indicating precipitation of anhydrite from a fluid containing 23 to 96 vol. % seawater (4 to
452 76 vol. % hydrothermal fluid).

453

454 **4.3. Sulfur Isotope Ratios**

455

456 Measured sulfur isotope compositions of drill core anhydrite from Roman Ruins range
457 from $\delta^{34}\text{S}\text{-SO}_4 = +19.6$ to $+23.1$ ‰, with most isotope ratios equal to or slightly heavier
458 than seawater sulfate ($\delta^{34}\text{S}\text{-SO}_4 = +21.0$ ‰, Rees et al., 1978) (Fig. 11). There is no clear

459 downhole trend beneath Roman Ruins of sulfur isotope compositions. Drill core anhydrite
460 samples from Snowcap display a wide range of sulfur isotope compositions, from $\delta^{34}\text{S}$ -
461 $\text{SO}_4 = +16.6 \text{‰}$ to $+21.9 \text{‰}$ (Fig. 11). Microchemical sulfur isotope data are consistent
462 with that measured by whole-rock analysis on the same Roman Ruins and Snowcap
463 samples (Roberts et al., 2003), although microchemical data reveal some intra-grain
464 heterogeneity and extend the range of sulfur isotope compositions by more than one per
465 mil. Anhydrites from Snowcap are the only samples to record $\delta^{34}\text{S}$ - SO_4 significantly
466 lighter than that of seawater. In general, sulfur isotope ratios trend toward lighter isotope
467 composition with increasing depth (Fig. 11).

468

469 Sulfur isotope compositions of seafloor massive anhydrites sampled from Fenway ($\delta^{34}\text{S}$ -
470 $\text{SO}_4 = +20.1 \text{‰}$ to $+22.0 \text{‰}$) cluster around that of seawater and are absent of light sulfur
471 isotopic ratios as seen at Snowcap. At North Su, sulfur isotope compositions of seafloor
472 massive anhydrite fall within a relatively narrow range, heavier than that of seawater
473 sulfate, with $\delta^{34}\text{S}$ - SO_4 between $+22.4$ and $+23.6 \text{‰}$ (Fig. 11).

474

475

5. DISCUSSION

476

5.1. Microchemical Heterogeneity Recorded by Anhydrite

478

479 The microchemical data for anhydrite samples presented here provide significant
480 information used to identify the sub-seafloor processes affecting formation of

481 hydrothermal fluids in the Manus back-arc basin, which can be compared and contrasted
482 with previous whole-rock data obtained for the same samples (e.g., Bach et al., 2003;
483 Roberts et al., 2003; Bach et al., 2005). The data reveal significant chemical (REE) and
484 isotopic (Sr, S) heterogeneity on the scale of individual anhydrite grains that are
485 unresolved by whole-rock analysis. Moreover, microchemical analyses also allow
486 interpretation of chemical data based on textural evidence. The textural characteristics of
487 all samples documented by petrographic and cathodoluminescence imaging, including
488 regular grain/crystal structures and sharply bounded chemical domains, support primary
489 growth of anhydrite without ‘diagenetic’ overprint. We interpret the fine-scale
490 heterogeneity as recording primary chemical signatures of the fluids from which anhydrite
491 was precipitated. Trace element and isotopic exchange or reequilibration, which might be a
492 post-depositional artifact as a result of anhydrite dissolution or replacement owing to
493 changes in fluid temperature and composition, do not affect the chemical signatures
494 preserved in our samples.

495

496 The REE and Sr and S isotope data suggest that anhydrite records evidence for
497 hydrothermal fluid formation affected by varying input of magmatic acid volatiles (H₂O–
498 CO₂–SO₂–HCl–HF) and for marked changes in near-seafloor hydrothermal fluid
499 circulation and mixing with locally entrained seawater, all of which impact the
500 composition of vent fluids and associated vent deposits. The microchemical analyses also
501 demonstrate that the relative influence of these processes varied dramatically on timescales
502 over which anhydrite was deposited. Detailed microchemical analyses can provide novel

503 insights to complex hydrothermal processes that might not be obtained only from whole-
504 rock studies.

505

506 *5.1.1. Anhydrite REE Patterns: Indicators of Hydrothermal Fluid Formation, Aqueous*
507 *REE Distributions and Conditions of Anhydrite Precipitation*

508

509 Anhydrite sampled from active hydrothermal fields in the Manus Basin (PACMANUS,
510 SuSu Knolls) exhibits a wide range of chondrite-normalized REE_N patterns (Figs. 4–7)
511 that are significantly more varied than relatively uniform REE_N patterns observed in
512 anhydrite sampled at mid-ocean ridge spreading centers (e.g., Mills and Elderfield, 1995;
513 Humphris, 1998; Humphris and Bach, 2005). Microchemical analysis reveals that this
514 heterogeneity is recorded at the intra-grain scale in many samples (Figs. 8–10), which was
515 not revealed by previous whole-rock analysis. The range of REE_N patterns measured likely
516 reflects control from one or several processes, including differences in absolute and
517 relative REE abundances in parent hydrothermal fluid, crystal lattice constraints on ion
518 substitution and solution controls (composition, temperature, oxygen fugacity) on REE
519 concentration and complexation. These controls have been discussed previously in context
520 of anhydrite precipitation at the TAG active mound (e.g., Mills and Elderfield, 1995;
521 Humphris, 1998; Humphris and Bach, 2005). At TAG, high-temperature black smoker
522 fluids and anhydrites have a very similar REE_N pattern, which has been interpreted as
523 reflecting partitioning of REEs, with the possible exception of Eu, into anhydrite without
524 significant fractionation (e.g., Mills and Elderfield, 1995). Discrimination against Eu, as

525 evidenced from negative Eu anomalies in fluid-normalized REE patterns, likely results
526 from the unique redox behavior of Eu in high temperature aqueous environments. At high
527 temperatures and reducing conditions, Eu is stable as Eu^{2+} instead of typical Eu^{3+}
528 (Sverjensky, 1984). The larger ionic radius of Eu^{2+} versus Eu^{3+} and resulting ionic radii
529 mismatch with Ca^{2+} can inhibit substitution of Eu^{2+} into anhydrite relative to neighboring
530 REE^{3+} . Variable Eu anomalies may indicate changes in temperature and redox conditions
531 under which anhydrite is precipitated as a result of mixing of hydrothermal fluid and
532 entrained seawater in different proportions. In more detail, subtle differences between
533 REE_N patterns measured in TAG hydrothermal fluids and anhydrite have been interpreted
534 to reflect minor fractionation between the REEs owing to formation of different aqueous
535 REE complexes resulting from differences in fluid composition (e.g., T , $f\text{O}_2$) during
536 hydrothermal fluid mixing with seawater (e.g., Humphris and Bach, 2005). In particular,
537 formation of REE-chloride complexes is predicted to enhance the stability to light-REEs
538 relative to mid- and heavy-REEs and so result in anhydrite with REE patterns that are
539 moderately light-REE depleted when normalized to REE composition of parent black-
540 smoker fluids (e.g., Humphris and Bach, 2005).

541

542 Seafloor massive anhydrites sampled at Fenway have the most uniform REE_N pattern of all
543 anhydrites examined in this study. REE_N patterns are sub-parallel and characterized by a
544 light-REE enrichment and positive Eu anomaly (Fig. 6). This pattern is very similar to that
545 recorded in anhydrite from mid-ocean ridge spreading centers and is also similar to that of
546 modern high-temperature black-smoker fluids sampled at Fenway (Fig. 12). If the

547 composition of contemporary hydrothermal fluids is representative of that from which
548 anhydrite at Fenway was precipitated, then the similar REE_N patterns imply that ion
549 substitution of REE into anhydrite occurred largely without intra-group fractionation (i.e.,
550 crystal lattice and solution chemistry did not fractionate significantly among the REEs).
551 This is demonstrated on a plot of La/Yb and Eu/Eu* ratios in anhydrite normalized to that
552 of endmember hydrothermal fluid when $(La/Yb)_{Anh-BSF} \sim 1$ and $(Eu/Eu^*)_{Anh-BSF} \sim 1$ (Fig.
553 13a). REE_N patterns of drill-core anhydrites sampled beneath Roman Ruins are broadly
554 uniform and also similar to that of anhydrite sampled at Fenway, except for a pronounced
555 negative Eu anomaly in some anhydrite grains formed at depths > 150 mbsf (Fig. 4).
556 Relative to REE abundances in modern high-temperature hydrothermal fluids sampled at
557 Roman Ruins (Fig. 12), REE patterns are broadly flat, $(La/Yb)_{Anh-BSF} \sim 1$, but show a
558 collective negative Eu anomaly, $(Eu/Eu^*)_{Anh-BSF} < 0.03$ to 0.5 (Fig. 13b). The broadly
559 uniform REE_N patterns (e.g., La/Yb ratios) preserved in anhydrites from Fenway and
560 Roman Ruins are interpreted as reflecting precipitation from parental hydrothermal fluids
561 with a REE composition that was uniform over periods of anhydrite formation.
562 Contemporary hydrothermal fluids sampled at Fenway and Roman Ruins are notable for
563 their low pH and relatively high volatile (e.g., CO₂, fluoride) concentrations relative to
564 high-temperature black smoker fluids sampled from mid-ocean ridge spreading centers,
565 and are considered a result of magmatic acid volatile degassing from felsic magmas
566 overlying the subduction margin coupled to high-temperature fluid-rock interaction
567 (Seewald et al., 2006; Reeves, 2010). On the basis of the REE data, we suggest that these
568 processes governing the sub-seafloor formation of high-temperature hydrothermal fluids

569 at Fenway and Roman Ruins have been maintained over the timescales on which anhydrite
570 was deposited.

571

572 The variable behavior of Eu during precipitation of anhydrite sampled from Fenway and
573 Roman Ruins argues that, although hydrothermal fluid compositions were likely similar,
574 the conditions of anhydrite precipitation from parent fluids differed. The lack of a large Eu
575 anomaly in REE_N patterns of Fenway anhydrites normalized to that of endmember
576 hydrothermal fluid suggests that Eu behaved similarly to neighboring Sm and Gd during
577 fluid–mineral partitioning. Likely, this reflects Eu present in trivalent form owing to lower
578 temperatures and more oxidizing conditions as a result of extensive mixing between
579 endmember hydrothermal fluid and seawater at the seafloor where massive anhydrite was
580 precipitated. Strontium isotopic (⁸⁷Sr/⁸⁶Sr) ratios measured in these anhydrites range
581 mostly from ~0.7065 to 0.7080 suggesting precipitation from a fluid mix contributed by
582 more than 55 to 60 vol. % seawater. Isoenthalpic mixing between ~40 vol. % hydrothermal
583 fluids at Fenway with temperatures ~ 340 to 360 °C (Seewald et al., 2006; Reeves, 2010)
584 and 60 vol. % seawater yields a mixed fluid with a temperature of ~150 °C. At this or
585 lower temperatures and corresponding oxygen fugacities, Eu can exist in trivalent form,
586 which is consistent with our interpretation that Eu behaved similarly to neighboring REEs.
587 In contrast, the pronounced negative Eu anomaly apparent in REE_N patterns of Roman
588 Ruins drill–core anhydrites suggests higher temperatures (≥ 250 °C) and more reducing
589 conditions during precipitation of most anhydrite beneath the seafloor at this vent field.
590 Strontium isotopic (⁸⁷Sr/⁸⁶Sr) ratios measured within individual samples range from

591 ~0.7050 to ~0.7080 (~20–75 vol. % hydrothermal fluid) and in anhydrite sampled from >
592 150 mbsf can extend to ~ 0.7042, similar to that of endmember hydrothermal fluids (> 95
593 vol. % hydrothermal fluid; Fig. 11). Isoenthalpic mixing between < 40 vol. % seawater and
594 > 60 vol. % endmember hydrothermal fluid with a temperature ~ 340 °C (Seewald et al.,
595 2006; Reeves, 2010) as implied by most measured $^{87}\text{Sr}/^{86}\text{Sr}$ ratios, yields temperatures of
596 precipitation in excess of 250 °C. Anhydrite deposition beneath Roman Ruins under
597 hydrothermal–dominant conditions is directly supported by fluid inclusion analysis of the
598 same samples (Vanko et al., 2004), which indicate temperatures of precipitation between
599 250 and 370 °C.

600

601 Microscale chemical heterogeneity and textural characteristics of drill–core anhydrites
602 from Roman Ruins and massive anhydrites from Fenway are also used to compare and
603 contrast conditions under which anhydrite precipitated at and beneath the seafloor.

604 Cathodoluminescence mapping and microchemical analyses demonstrate that significant
605 heterogeneity in terms of absolute REE concentrations is recorded at the intra–grain scale
606 in many Roman Ruins anhydrites, particularly in those deposited at depth (Figs. 4, 8).

607 Mapping indicates that boundaries between chemically distinct domains are sharp, which
608 likely preserve primary growth. The chemical heterogeneity is interpreted as recording
609 dramatic shifts between hydrothermal–dominant and seawater–dominant conditions under
610 which anhydrite was precipitated and might reflect intermittent pulsing of hydrothermal
611 fluid from depth and changes in pathways for fluid flow through permeable shallow crustal
612 rocks. The range of $^{87}\text{Sr}/^{86}\text{Sr}$ ratios recorded on the scale of individual anhydrite grains

613 (Fig. 8) further supports dramatic changes between hydrothermal–dominant and seawater–
614 dominant fluid regimes in the sub–seafloor hydrothermal environment. Although there is
615 no direct information as to crystal growth rates, the sub–millimeter scale at which chemical
616 heterogeneity in anhydrite grains is recorded at Roman Ruins suggests that changes in fluid
617 flow were rapid. By comparison, massive anhydrites sampled at Fenway exhibit uniform
618 REE distributions and small Sr isotopic variability on the scale of individual grains (Fig.
619 10). This chemical and isotopic homogeneity implies that mixing between hydrothermal
620 fluid and entrained seawater was both extensive and sustained at the seafloor within the
621 Fenway mound relative to that inferred within the crust.

622

623 A very different history of hydrothermal fluid formation and sub–seafloor mixing beneath
624 Snowcap is recognized from REE compositions of anhydrite. Drill–core anhydrite sampled
625 beneath Snowcap exhibit a wide range of chondrite–normalized REE_N distribution patterns
626 (Fig. 5), different from that documented in anhydrite from both Roman Ruins and Fenway.
627 The REE_N patterns of Snowcap anhydrites are markedly different from those of modern
628 hydrothermal fluids sampled at this vent field (Fig. 12), which are characterized by
629 uniform light–REE enrichment and a positive Eu anomaly (Craddock et al., 2010).
630 Accordingly, when normalized to REE concentrations in modern hydrothermal fluid, the
631 REE patterns of Snowcap anhydrites show distinct and fractionated patterns ($(La/Yb)_{Anh-BSF}$
632 $= 0.02–15.4$ and $(Eu/Eu^*)_{Anh-BSF} = 0.06–1.8$; Fig. 13). If the REEs are partitioned into
633 Snowcap anhydrites without fractionation from parent hydrothermal fluid composition,
634 then the range of REE_N patterns recorded in anhydrite imply that anhydrite was

635 precipitated in the past from generations of hydrothermal fluids having very different
636 chemistry compared to that of modern fluids. Alternatively, solution effects and REE
637 complexation controlled REE partitioning between fluid (with a composition the same as
638 contemporary fluids) and anhydrite, resulting in significant intra-group fractionation
639 during anhydrite deposition. Ion complexation, however, appears inconsistent with the
640 range of both light-REE and heavy-REE enrichments and of positive and negative Eu
641 anomalies measured in Snowcap anhydrites. If ion complexation were the dominant
642 control on measured REE_N patterns in anhydrite, then partitioning of REE between fluid
643 and anhydrite should behave in a predictable manner as a function of fluid composition
644 (e.g., ligand concentration, pH). Endmember compositions of the highest temperature vent
645 fluids sampled from Fenway, Roman Ruins and Snowcap are similar, particularly with
646 respect to chondrite-normalized REE_N distributions and Cl⁻, F⁻ and SO₄²⁻ ligand
647 concentrations (Table 2). The resulting speciation of REEs in these sampled fluids is
648 therefore very similar (Craddock et al., 2010), and the partitioning behavior of REEs
649 between fluid and anhydrite, if governed primarily by solution complexation, should be the
650 same. REE complexation in modern hydrothermal fluids sampled from Fenway, Roman
651 Ruins and Snowcap is controlled primarily by chloride (Craddock et al., 2010) and is
652 similar to that predicted at mid-ocean ridge hydrothermal systems (e.g., Humphris and
653 Bach, 2005). Chloride-dominated REE complexation has been interpreted to cause minor
654 discrimination against the light-REEs and Eu²⁺ during precipitation of some anhydrites at
655 TAG (Humphris and Bach, 2005). The same solution chemistry effects cannot also explain

656 the wide range of REE_N patterns observed in Snowcap anhydrites, ranging from light-REE
657 to heavy-REE enriched to flat, with both positive and negative Eu anomalies.

658

659 We infer that anhydrite deposited beneath Snowcap likely records the past presence of
660 distinct hydrothermal fluids at this field with very different REE concentrations and
661 relative distributions. In particular, the relatively flat and heavy-REE enriched REE_N
662 patterns documented in Snowcap anhydrites (Fig. 5) are inferred to reflect the existence of
663 low pH “acid-sulfate” fluids at this field in the recent past, because these flat REE_N
664 patterns are most similar to those of modern acid-sulfate fluids sampled at the nearby
665 DESMOS and SuSu Knolls hydrothermal systems (Fig. 12) (Craddock et al., 2010). The
666 composition of acid-sulfate fluids (e.g., low pH, high SO₄²⁻ concentration) sampled at
667 DESMOS and SuSu Knolls (Table 2) is best explained by substantial injection of
668 magmatic acid volatiles (H₂O–CO₂–SO₂–HCl–HF) from underlying felsic magmas and
669 mixing with seawater in the shallow crust, in the absence of typical high-temperature
670 convective hydrothermal fluid circulation and reaction with fresh crustal rocks (e.g.,
671 Seewald et al., 2006). This represents a fundamentally different style of hydrothermal fluid
672 formation compared to that proposed for high-temperature, black smoker-type fluids
673 sampled at mid-ocean ridge spreading centers. REE_N patterns preserved in Snowcap
674 anhydrite record evidence of acid-sulfate type magmatic-hydrothermal activity, even
675 though modern hydrothermal fluids sampled from PACMANUS vent fields do not. The
676 existence of acid-sulfate fluids at Snowcap in the past is supported by feldspar destructive
677 alteration characteristic of fluid-rock interaction at very low pH ≤ 2 (e.g., illite–

678 pyrophyllite–cristobalite + native sulfur) in the same drill–cores from which anhydrite was
679 recovered (Lackschewitz et al., 2004; Binns et al., 2007). The absence of similar anhydrite
680 REE_N patterns and feldspar destructive alteration in drill core samples from Roman Ruins
681 or in seafloor samples from Fenway do not support acid–sulfate type magmatic–
682 hydrothermal activity at these areas only several km away from Snowcap. The intra–grain
683 scale at which variations in REE_N patterns are observed within Snowcap anhydrites implies
684 that magmatic acid volatile input and pathways for hydrothermal fluid circulation and
685 near–seafloor mixing with entrained seawater beneath seafloor hydrothermal systems in
686 subduction margin environments varies substantially on rapid timescales.

687

688 Massive anhydrite at North Su (SuSu Knolls) records a range of REE_N patterns that are
689 similar to those measured in drill–core anhydrites from Snowcap. These REE_N patterns
690 range from light–REE, to mid–REE, to heavy–REE enriched and are not generally similar
691 to that of contemporary smoker–type fluids venting nearby ($(La/Yb)_{Anh-BSF} \neq 1$,
692 $(Eu/Eu^*)_{Anh-BSF} \neq 1$; Figs. 13). REE_N patterns in some grains are similar, although not
693 identical, to that of acid–sulfate fluids exiting the seafloor on the flanks of the North Su
694 volcano and that of fluoride–rich hydrothermal fluids venting at the neighboring Suzette
695 and South Su vent fields (Fig. 12) (Craddock et al., 2010). The data are interpreted as
696 reflecting precipitation of massive anhydrite at North Su from hydrothermal fluid
697 influenced by acid–sulfate–type activity, similar to that inferred in the past at Snowcap.
698 The fine–scale REE heterogeneity in North Su massive anhydrite documented by
699 microchemical analysis contrasts markedly with relatively homogeneous REE distributions

700 in seafloor massive anhydrites from Fenway, suggesting a complex history of
701 hydrothermal fluid formation at the seafloor at North Su. Petrographic and
702 cathodoluminescence imaging highlights the complex textures related to formation of
703 anhydrite at North Su, including composite banding, possible veining and a range of grain
704 sizes (Figs. 3, 10). These textures likely reflect discrete episodes of anhydrite deposition.
705 The different REE signatures recorded among these domains (Fig. 10) imply that episodes
706 of anhydrite precipitation were influenced by fluids of differing composition, which were
707 possibly related to fundamentally different styles of hydrothermal fluid formation
708 including dramatic shifts between black–smoker and acid–sulfate fluid formation.
709 Differences in the physical and chemical characteristics of hydrothermal fluid formation
710 within individual vent fields in the Manus Basin is well illustrated by active venting of
711 both black smoker and acid–sulfate fluids less than 25 m apart at the seafloor at North Su.

712

713 *5.1.2. Microchemical Analysis of Sulfur and Strontium Isotope Ratios: Constraints on*
714 *Magmatic Contributions in Submarine Hydrothermal Systems*

715

716 Sulfur isotopic compositions ($\delta^{34}\text{S}\text{-SO}_4$) of anhydrite samples measured by microchemical
717 analysis cluster mostly around that of contemporary seawater sulfate (+21 ‰ Rees et al.,
718 1978), or extend to heavier values, up to +24 ‰ (Fig. 11). Where whole–rock sulfur
719 isotope analyses were carried out on the same drill–core samples (Roberts et al., 2003),
720 microchemical and whole–rock data are similar. Sulfate in anhydrite from all vent fields
721 was contributed predominantly by seawater. Sulfur isotopic ratios in anhydrite heavier than

722 that of seawater can be explained by partial reduction of seawater sulfate to H₂S by action
723 of ferrous iron in hydrothermal fluid (e.g., Shanks et al., 1981; Janecky and Shanks, 1988).
724 Strontium isotope (⁸⁷Sr/⁸⁶Sr) ratios measured on the same grains fall between that of
725 endmember hydrothermal fluid (⁸⁷Sr/⁸⁶Sr ~ 0.7042) and seawater (⁸⁷Sr/⁸⁶Sr ~ 0.70918; Fig.
726 11) supporting that anhydrite was precipitated from a mix of hydrothermal fluid with a
727 significant fraction of locally entrained and admixed sulfate-rich seawater. As previously
728 emphasized, the intra-grain scale on which strontium isotopic heterogeneity is recorded in
729 most samples implies that there were dramatic, and likely rapid, shifts between distinctly
730 hydrothermal- and seawater-dominant fluid regimes, possibly reflecting pulsing of
731 hydrothermal fluid from depth and changes in pathways for fluid flow through permeable
732 shallow crustal rocks.

733

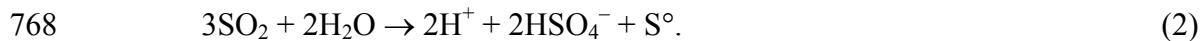
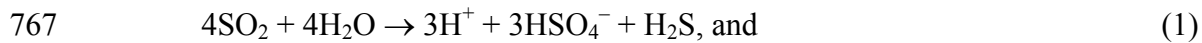
734 Sulfur isotopic compositions extend to light values ($\delta^{34}\text{S}\text{-SO}_4 \leq 17 \text{ ‰}$) in some grains of
735 drill-core anhydrites recovered from depths ~ 300 mbsf beneath Snowcap. Potential
736 sources of sulfate with S isotopic ratios lower than seawater include (1) oxidation of
737 aqueous H₂S in hydrothermal fluid (Shanks et al., 1995; Shanks, 2001), (2) equilibrium
738 isotope exchange between aqueous sulfate and H₂S at high temperatures $\geq 380 \text{ °C}$
739 (Ohmoto and Lasaga, 1982), and (3) disproportionation of magmatic SO₂ to yield sulfate
740 (Drummond, 1981; Kusakabe et al., 2000). Compositions of contemporary seafloor
741 hydrothermal fluids sampled from both PACMANUS and SuSu Knolls are inconsistent
742 with oxidation of H₂S during mixing of hydrothermal fluid and locally entrained seawater
743 at sites of anhydrite precipitation. Most vent fluids at PACMANUS and SuSu Knolls

744 contain measurable amounts of both H₂S and sulfate (Table 2), indicating that these
745 species have not come to chemical equilibrium and that H₂S oxidation has not occurred
746 (see Craddock et al., 2010). Kinetic considerations argue against sulfur isotopic
747 equilibrium exchange between sulfate and H₂S to explain isotopically–light δ³⁴S–SO₄
748 compositions. At PACMANUS and SuSu Knolls, measured temperatures of seafloor vent
749 fluids (Craddock et al., 2010; Reeves, 2010) and/or fluid inclusion studies of anhydrite
750 (Vanko et al., 2004) suggest maximum fluid temperatures at depths < 300 mbsf in the crust
751 between 360 and 400 °C, and precipitation of anhydrite from fluids with temperatures
752 mostly less than 350 °C. The Δ³⁴S_{SO₄–H₂S} ~19 ‰ difference between isotopically light
753 sulfate in anhydrite (δ³⁴S ~ +17 ‰) and H₂S in sampled Manus hydrothermal fluids (δ³⁴S ~
754 –1 to –3 ‰; Reeves, 2010) implies sulfur isotopic exchange at temperatures ~ 350 °C
755 (Ohmoto and Lasaga, 1982). At this range of temperatures, however, timescales of sulfur
756 isotopic equilibration between sulfate and H₂S are slow (> 50 to 70 hours) relative to that
757 expected for precipitation of anhydrite (e.g., Ohmoto and Lasaga, 1982).

758

759 We suggest that disproportionation of magmatic SO₂ is the likely source for isotopically
760 light δ³⁴S–SO₄ recorded in drill core anhydrite recovered from Snowcap, consistent with
761 the conclusions of Roberts et al. (2003) based on whole–rock sulfur isotopic analyses of
762 Snowcap anhydrite samples. Sulfur dioxide, which can be present and degassed from
763 shallow, water–rich felsic magmas at subduction–related oceanic and continental margins
764 (see review by Rye, 2005), can undergo disproportionation to yield both oxidized and

765 reduced forms of sulfur according to the following reactions (e.g., Holland, 1965;
766 Drummond, 1981);



769 Experimental data document large isotopic fractionations between sulfate and reduced
770 sulfur owing to SO_2 disproportionation, with sulfate enriched by +16 to +21 ‰ relative to
771 reduced sulfur (Kusakabe et al., 2000). For an initial bulk $\delta^{34}\text{S}$ of SO_2 in the magma $\sim 2 \pm 2$
772 ‰ (e.g., Deen, 1990), isotopic mass balance constrains the sulfur isotopic composition of
773 the resulting hydrothermal fluid to $\delta^{34}\text{S}\text{-SO}_4 \sim +6$ to +10 ‰ and $\delta^{34}\text{S}\text{-H}_2\text{S} \sim -6$ to -10 ‰.
774 The measured $\delta^{34}\text{S}$ of H_2S of most PACMANUS and SuSu Knolls fluids is in the range -1
775 to -3 ‰ (Reeves, 2010), which is consistent with that expected from hydrothermal
776 contributions of H_2S from magmatic SO_2 disproportionation. Similarly, $\delta^{34}\text{S}\text{-SO}_4$ ratios
777 recorded in anhydrite lighter than that of seawater is consistent with contribution of sulfate
778 derived from magmatic SO_2 disproportionation. Mixing between sulfate-bearing
779 magmatic-hydrothermal fluid ($\delta^{34}\text{S}\text{-SO}_4 \sim +6$ to +10 ‰) and contemporary seawater
780 ($\delta^{34}\text{S}\text{-SO}_4 \sim +21$ ‰) can yield a mixed fluid with a sulfate-sulfur isotopic ratio $\sim +14$ to
781 +18 ‰, similar to that recorded in some Snowcap drill-core anhydrites. The presence of
782 sulfate-rich fluids of magmatic origin (i.e., acid-sulfate fluids) at Snowcap is consistent
783 with our interpretations of REE signatures in the same anhydrites.

784

785 The absence of light $\delta^{34}\text{S}\text{-SO}_4$ ratios in anhydrite from Roman Ruins and Fenway at
786 PACMANUS and North Su at SuSu Knolls does not support acid-sulfate-type activity at

787 these vent areas. However, it does not exclude such activity. The isotopic fingerprint for
788 sulfate of magmatic origin can be diluted by large amounts of seawater–sulfate contributed
789 by local seawater entrainment or overprinted by sulfate reduction. The sulfur isotopic
790 evolution of sulfate during conservative mixing of magmatic-hydrothermal fluid and
791 seawater can be examined in Sr and S isotope space (Fig. 14). Dashed lines in Figure 14
792 are conservative mixing trends between contemporary seawater ($^{87}\text{Sr}/^{86}\text{Sr} = 0.70918$, $\delta^{34}\text{S}$ –
793 $\text{SO}_4 = +21$ ‰) and modeled magmatic–hydrothermal fluids ($^{87}\text{Sr}/^{86}\text{Sr} = 0.7042$, $\delta^{34}\text{S}$ –
794 $\text{SO}_4 = +8$ ‰) with a range of sulfate concentrations (0, 15 and 100 mmol/kg). The sulfur
795 isotopic composition of “magmatic” sulfate in these calculations (+8 ‰) is that measured
796 during experimental SO_2 disproportionation at temperatures ~ 300 °C (Kusakabe et al.,
797 2000) and calculated from isotopic mass balance above. A sulfate concentration of zero in
798 the endmember hydrothermal fluid implies complete absence of magmatic sulfate. Coupled
799 measurements of strontium and sulfur isotope ratios indicate that ~ 12 to 15 mmol/kg
800 magmatic sulfate is required in the endmember magmatic–hydrothermal fluid to preserve
801 light $\delta^{34}\text{S}$ – SO_4 compositions measured in drill–core anhydrite from Snowcap ($\sim +16$ to
802 $+17$ ‰) for the appropriate mixing proportions between seawater (50 to 70 vol. %) and
803 hydrothermal fluid (30 to 50 vol. %). The seawater–like $\delta^{34}\text{S}$ ratios of anhydrites from
804 neighboring Fenway and Roman Ruins may reflect much lower concentrations of
805 magmatic sulfate (< 1 to 3 mmol/kg) in the endmember hydrothermal fluid from which
806 anhydrite at these fields was precipitated and overprint of the small magmatic signature
807 owing to mixing with seawater as indicated by the range of strontium isotopic ratios
808 recorded in the same grains. Directly coupled REE data for the same anhydrites from

809 Roman Ruins and Fenway, as provided by novel microchemical analysis, bear information
810 on this discussion. The relatively uniform chondrite-normalized REE_N pattern of
811 anhydrites from Roman Ruins and Fenway, which is similar to that of mid-ocean ridge
812 hydrothermal fluids but markedly different to that of acid-sulfate fluids, argues against
813 acid-sulfate style hydrothermal fluids at Roman Ruins or Fenway in the past. Owing to the
814 several orders of magnitude higher concentrations of REEs in hydrothermal fluids versus
815 seawater (in contrast to abundant sulfate in seawater versus hydrothermal fluid), REE
816 signatures in anhydrite may be particularly diagnostic of magmatic-hydrothermal
817 processes occurring at depth, despite extensive influx and overprint by seawater near the
818 seafloor at sites of fluid and mineral sampling.

819

820

6. SUMMARY AND CONCLUSIONS

821

822 Coupled microchemical analysis of rare earth elements (REEs) and Sr and S isotopes in
823 seafloor and sub-seafloor anhydrites provides insights to processes governing the
824 formation and evolution of hydrothermal fluids in the subduction-related Manus Basin,
825 Papua New Guinea. Chondrite-normalized REE patterns recorded in anhydrites sampled at
826 the PACMANUS (Roman Ruins, Snowcap and Fenway) and SuSu Knolls (North Su) vent
827 fields show remarkable heterogeneity (light-REE enriched, heavy-REE enriched and flat
828 patterns with both positive and negative Eu anomalies) different to relatively uniform
829 REE_N patterns in anhydrites from mid-ocean ridge deposits. The range of REE_N patterns
830 documented in anhydrite is very similar to that observed in seafloor hydrothermal fluids

831 sampled from the same vent fields (Douville et al., 1999; Craddock et al., 2010). Magmatic
832 acid volatile input ($\text{H}_2\text{O}-\text{SO}_2-\text{CO}_2-\text{HCl}-\text{HF}$) significantly impacts the composition of
833 sampled black smoker-type and acid-sulfate-type fluids in the Manus Basin, which affects
834 the solubility of REEs during fluid-rock interaction (Craddock et al., 2010). The different
835 REE_N patterns recorded in anhydrite are interpreted as recording extended periods of
836 significant, but spatially and temporally variable, magmatic volatile degassing from felsic
837 magmas overlying the actively subducting slab. In particular, variable REE_N patterns
838 preserved in anhydrites sampled from beneath the Snowcap vent field record evidence for
839 acid-sulfate fluid activity at PACMANUS (very low pH and high sulfate concentrations
840 reflecting substantial input of magmatic SO_2) in the recent geologic past, which is not
841 manifest today. Past episodes of acid-sulfate activity at Snowcap was likely similar to that
842 on-going at the nearby SuSu Knolls hydrothermal system.

843

844 The REE data are complemented by sulfur and strontium isotopic data for the same
845 samples. Sulfate $\delta^{34}\text{S}$ ratios of most anhydrite grains cluster around that of contemporary
846 seawater (+21 ‰), indicating that sulfate was contributed primarily from seawater sulfate
847 owing to anhydrite precipitation at both PACMANUS and SuSu Knolls from a variable
848 mix of hydrothermal fluid and locally entrained seawater. Strontium isotopic ($^{87}\text{Sr}/^{86}\text{Sr}$)
849 ratios of the same anhydrites fall between that of contemporary seawater (= 0.70918) and
850 endmember hydrothermal fluids (~ 0.7042) supporting that anhydrite was deposited from a
851 mix of the two. Sulfate $\delta^{34}\text{S}$ isotope ratios extend to values lighter than that of seawater in
852 a few anhydrites recovered at depths ~300 mbsf beneath Snowcap. These light ratios

853 ($\delta^{34}\text{S}\text{-SO}_4 \sim +16$ to $+18$ ‰) are best explained by contribution of sulfur from magmatic
854 SO_2 and past existence of acid–sulfate fluids at Snowcap, consistent with that predicted
855 from REE data for the same anhydrites. The absence of anhydrite with light $\delta^{34}\text{S}\text{-SO}_4$
856 ratios sampled from either Roman Ruins or Fenway implies an absence of similar acid–
857 sulfate activity at these neighboring vent fields, although extensive entrainment and mixing
858 of sulfate–rich seawater with hydrothermal fluids within the Roman Ruins and Fenway
859 vent deposits may have overprinted evidence for such activity.

860

861 Microchemical REE, Sr isotope and S isotope data presented in this study can be compared
862 and contrasted with that obtained previously by whole–rock analyses of anhydrites
863 sampled at PACMANUS (Bach et al., 2003; Roberts et al., 2003; Bach et al., 2005).

864 Microchemical and whole–rock analyses yield broadly similar data and complementary
865 information. However, microchemical analyses reveal significant chemical and isotopic
866 heterogeneity at the sub–millimeter scale within individual grains that cannot be captured
867 by whole–rock studies. The fine spatial scale at which chemical and isotopic variability is
868 recorded in anhydrite highlights the dynamic nature of submarine hydrothermal activity in
869 the Manus Basin. Both high–temperature black smoker activity (characterized by
870 convective circulation of seawater–derived hydrothermal fluids) and acid–sulfate fluid
871 activity (reflecting significant contribution of degassing magmatic acid volatiles, $\text{H}_2\text{O}\text{-}$
872 $\text{SO}_2\text{-CO}_2\text{-HCl-HF}$, in the absence of typical convective hydrothermal fluid circulation)
873 can exist at a single vent field as demonstrated by grain–scale heterogeneity among
874 coupled REEs distributions and sulfur isotopic ratios. Further, the chemical and isotopic

875 heterogeneity preserved within individual grains records evidence of dramatic shifts
876 between alternating hydrothermal–dominant and seawater–dominant near–seafloor fluid
877 circulation, possibly reflecting pulsing of magmatic–hydrothermal fluid from depth and
878 changes in pathways for fluid flow within shallow crustal rocks. Micro–scale chemical and
879 isotopic analyses of hydrothermal minerals can provide critical insights to submarine
880 hydrothermal processes that evolve chemically over time and cannot otherwise be
881 constrained from the study of contemporary vent fluids.

882

883 **ACKNOWLEDGMENTS**

884

885 The authors thank the Captain and crew of the *R/V Melville* and *ROV Jason II* technical
886 group (cruise MGLN06MV) for a successful cruise and sample collection. This research
887 also used samples supplied by the Ocean Drilling Program (ODP). ODP is sponsored by
888 the US National Science Foundation (NSF) and participating countries under management
889 of Joint Oceanographic Institutions, Inc. (JOI). D. Vanko (University of Towson) is
890 acknowledged for generously preparing and providing a selection of drill core anhydrites
891 used in this study. M. Sulanowska and B. Schroeder (WHOI) assisted in the preparation of
892 massive anhydrite samples. L. Ball and D. Schneider (WHOI) provided technical support
893 for isotopic and elemental analysis. Constructive and thoughtful comments from four
894 anonymous reviewers significantly improved the clarity and presentation of our results and
895 ideas. Editorial assistance provided by AE J. Alt is gratefully acknowledged. This study
896 received financial support from an Ocean Drilling Program Schlanger Fellowship (P.R.C.),

897 NSF grant OCE-0327448 (W.B.), and DFG-Research Center/Excellence Cluster 'The
898 Ocean in the Earth System' (W.B.)

899

900 **REFERENCES**

901

902 Anders E. and Grevesse N. (1989) Abundances of the elements: Meteoritic and solar.

903 *Geochimica et Cosmochimica Acta* 53, 197-214.

904 Bach W., Roberts S., and Binns R. A. (2005) Data Report: Chemical and isotopic (S, Sr)

905 composition of anhydrite from ODP Leg 193, PACMANUS hydrothermal system,

906 Manus Basin, Papua New Guinea. In *Proceedings of the Ocean Drilling Program,*

907 *Scientific Results*, Vol. 193 (ed. F. J. A. S. Barriga, R. A. Binns, D. J. Miller, and P.

908 M. Herzig), pp. 1-23. Ocean Drilling Program, College Station, TX.

909 Bach W., Roberts S., Vanko D. A., Binns R. A., Yeats C. J., Craddock P. R., and

910 Humphris S. E. (2003) Controls of fluid chemistry and complexation on rare-earth

911 element contents of anhydrite from the Pacmanus seafloor hydrothermal

912 system, Manus Basin, Papua New Guinea. *Mineralium Deposita* 38(8), 916-935.

913 Belshaw N. S., Freedman P. A., O'Nions R. K., Frank M., and Guo Y. (1998) A new

914 variable dispersion double-focusing plasma mass spectrometer with performance

915 illustrated for Pb isotopes. *International Journal of Mass Spectrometry* 181, 51-58.

916 Binns R. A., Barriga F. J. A. S., and Miller D. J. (2007) Leg 193 synthesis: Anatomy of an

917 active felsic-hosted hydrothermal system, eastern Manus Basin, Papua New

918 Guinea. In *Proceedings of the Ocean Drilling Program, Scientific Results*, Vol. 193

919 (ed. F. J. A. S. Barriga, R. A. Binns, D. J. Miller, and P. M. Herzig), pp. 1-71.
920 Ocean Drilling Program, College Station, TX.

921 Binns R. A. and Scott S. D. (1993) Actively forming polymetallic sulfide deposits
922 associated with felsic volcanic rocks in the eastern Manus back-arc basin, Papua
923 New Guinea. *Economic Geology* 88, 2226-2236.

924 Binns R. A., Scott S. D., Gemmell J. B., Crook K. A. W., and Shipboard Scientific Party.
925 (1997) The SuSu Knolls hydrothermal field, eastern Manus Basin, Papua New
926 Guinea. *EOS Trans. AGU. Fall Meet. Suppl.*, 78(52), Abstract #V22E-02.

927 Bischoff J. L. and Dickson F. W. (1975) Seawater-basalt interaction at 200 °C and 500
928 bars: Implications for origin of seafloor heavy-metal deposits and regulations of
929 seawater chemistry. *Earth and Planetary Science Letters* 25, 385-397.

930 Bischoff J. L. and Seyfried W. E., Jr. (1978) Hydrothermal chemistry of seawater from 25°
931 to 350°C. *American Journal of Science* 278, 838-860.

932 Brimhall G. H., Jr. and Ghiorso M. S. (1983) Origin and ore-forming consequences of the
933 advanced argillic alteration process in hypogene environments by magmatic gas
934 contamination of meteoric fluids. *Economic Geology* 78, 73-90.

935 Butterfield D. A., Massoth G. J., McDuff R. E., Lupton J. E., and Lilley M. D. (1990)
936 Geochemistry of hydrothermal fluids from Axial Seamount Hydrothermal
937 Emissions Study vent field, Juan de Fuca Ridge: subseafloor boiling and
938 subsequent fluid-rock interaction. *Journal of Geophysical Research* 95(B8), 12895-
939 12921.

940 Chiba H., Uchiyama N., and Teagle D. A. H. (1998) Stable isotope study of anhydrite and
941 sulfide minerals at the TAG hydrothermal mound, Mid-Atlantic Ridge, 26 °N. In
942 *Proceedings of the Ocean Drilling Program, Scientific Results*, Vol. 158 (ed. P. M.
943 Herzig, S. E. Humphris, D. J. Miller, and R. A. Zierenberg), pp. 85-90. Ocean
944 Drilling Program.

945 Craddock P. R. (2009) Geochemical Tracers of Processes Affecting the Formation of
946 Seafloor Hydrothermal Fluids and Deposits in the Manus Back-arc Basin. Ph. D.
947 Thesis, Massachusetts Institute of Technology-Woods Hole Oceanographic
948 Institution, Woods Hole, MA, 370 pp.

949 Craddock P. R., Bach W., Seewald J. S., Rouxel O. J., Reeves E., and Tivey M. K. (2010)
950 Rare earth element abundances in hydrothermal fluids from the Manus Basin,
951 Papua New Guinea: Indicators of sub-seafloor hydrothermal processes in back-arc
952 basins. *Geochimica et Cosmochimica Acta* this issue.

953 Craddock P. R., Rouxel O. J., Ball L. A., and Bach W. (2008) Sulfur isotope measurement
954 of sulfate and sulfide by high-resolution MC-ICP-MS. *Chemical Geology* 253, 102-
955 113.

956 Davies H. L., Honza E., Tiffin D. L., Lock J., Okuda Y., Keene J. B., Murakami F., and
957 Kisimoto K. (1987) Regional setting and structure of the western Solomon Sea.
958 *Geo-Marine Letters* 7, 153-160.

959 Deen J. A. (1990) Hydrothermal ore deposition related to high-level igneous activity: a
960 stable-isotopic study of the Julcani mining district, Peru. Ph. D. Thesis, University
961 of Colorado, Boulder.

962 Douville E., Bienvenu P., Charlou J. L., Donval J. P., Fouquet Y., Appriou P., and Gamo
963 T. (1999) Yttrium and rare earth elements in fluids from various deep-sea
964 hydrothermal systems. *Geochimica et Cosmochimica Acta* 63(5), 627-643.

965 Drummond S. E., Jr. (1981) Boiling and Mixing of Hydrothermal Fluids: Chemical Effects
966 on Mineral Precipitation, The Pennsylvania State University.

967 Edmond J. M., Campbell A. C., Palmer M. R., German C. R., Klinkhammer G. P.,
968 Edmonds H. N., Elderfield H., Thompson G., and Rona P. (1995) Time series
969 studies of vent fluids from the TAG and MARK sites (1986, 1990) Mid-Atlantic
970 Ridge and a mechanism for Cu/Zn zonation in massive sulphide orebodies. In
971 *Hydrothermal Vents and Processes*, Vol. 87 (ed. L. M. Parson, C. L. Walker, and
972 D. R. Dixon), pp. 77-86. Geological Society Special Publication.

973 Gamo T., Okamura K., Charlou J. L., Urabe T., Auzende J. M., Ishibashi J.-I., Shitashima
974 K., Chiba H., Binns R. A., and Gena K. (1997) Acidic and sulfate-rich
975 hydrothermal fluids from the Manus back-arc basin, Papua New Guinea. *Geology*
976 25(2), 139-142.

977 Goldfarb M. S. (1982) Submarine Sulfide Deposits on the East Pacific Rise, 21 °N. Ph. D.
978 Thesis, Massachusetts Institute of Technology.

979 Hart S. R., Ball L., and Jackson M. J. (2005) Sr isotope by laser ablation PIMMS:
980 Application to Cpx from Samoan peridotite xenoliths. WHOI Plasma Facility Open
981 File Technical Report 11, pp. 15. Woods Hole Oceanographic Institution, Woods
982 Hole, MA.

983 Haymon R. M. (1983) Growth history of hydrothermal black smoker chimneys. *Nature*
984 301(5902), 695-698.

985 Hemley J. J., Hostetler P. B., Gude A. J., and Mountjoy W. T. (1969) Some stability
986 relations of alunite. *Economic Geology* 64, 599-612.

987 Holland H. D. (1965) Some applications of thermochemical data to problems of ore
988 deposits; [II] Mineral assemblages and the composition of ore forming fluids.
989 *Economic Geology* 60(6), 1101-1166.

990 Humphris S. E. (1998) Rare earth element composition of anhydrite: Implications for
991 deposition and mobility within the TAG hydrothermal mound. In *Proceedings of*
992 *the Ocean Drilling Program, Scientific Results*, Vol. 158 (ed. P. M. Herzig, S. E.
993 Humphris, D. J. Miller, and R. A. Zierenberg), pp. 143-159. Ocean Drilling
994 Program.

995 Humphris S. E. and Bach W. (2005) On the Sr isotope and REE compositions of
996 anhydrites from the TAG seafloor hydrothermal system. *Geochimica et*
997 *Cosmochimica Acta* 69, 1511-1525.

998 Humphris S. E., Herzig P. M., Miller D. J., Alt J. C., Becker K., Brown D., Brüggmann G.,
999 Chiba H., Fouquet Y., and Gemmell J. B. (1995) The internal structure of an active
1000 sea-floor massive sulphide deposit. *Nature* 377(6551), 713-716.

1001 Humphris S. E. and Thompson G. (1978) Hydrothermal alteration of oceanic basalts by
1002 seawater. *Geochimica et Cosmochimica Acta* 42(1), 107-125.

1003 Janecky D. R. and Shanks W. C., III. (1988) Computational modeling of chemical and
1004 sulfur isotopic reaction processes in seafloor hydrothermal systems: chimneys,

1005 massive sulfides, and subjacent alteration zones. *Canadian Mineralogist* 26, 805-
1006 825.

1007 Kent A. J. R., Jacobsen B., Peate D. W., Waight T. E., and Baker J. A. (2004) Isotope
1008 dilution MC-ICP-MS rare earth element analysis of geochemical reference
1009 materials NIST SRM 610, NIST SRM 612, NIST SRM 614, BHVO-2G, BHVO-2,
1010 BCR-2G, JB-2, WS-E, W-2, AGV-1 and AGV-2. *Geostandards and Geoanalytical
1011 Research* 28(3), 417-429.

1012 Kusakabe M., Komoda Y., Takano B., and Abiko T. (2000) Sulfur isotopic effects in the
1013 disproportionation reaction of sulfur dioxide in hydrothermal fluids: Implications
1014 for the $\delta^{34}\text{S}$ variations of dissolved bisulfate and elemental sulfur from active crater
1015 lakes. *Journal of Volcanology and Geothermal Research* 97(1-4), 287.

1016 Lackschewitz K. S., Devey C. W., Stoffers P., Botz R., Eisenhauer A., Kummetz M.,
1017 Schmidt M., and Singer A. (2004) Mineralogical, geochemical and isotopic
1018 characteristics of hydrothermal alteration processes in the active, submarine, felsic-
1019 hosted PACMANUS field, Manus Basin, Papua New Guinea. *Geochimica et
1020 Cosmochimica Acta* 68(21), 4405-4427.

1021 Marshall D. J. (1988) *Cathodoluminescence of Geological Materials*. Unwin Hyman Ltd.

1022 Martinez F. and Taylor B. (1996) Backarc spreading, rifting, and microplate rotation,
1023 between transform faults in the Manus Basin. *Marine Geophysical Researches* 18,
1024 203-224.

- 1025 Meyer C. A. and Hemley J. J. (1967) Wall-rock alteration. In *Geochemistry of*
1026 *Hydrothermal Ore Deposits, 1st Edition* (ed. H. L. Barnes), pp. 166-235. Holt,
1027 Rinehart and Winston.
- 1028 Mills R. A. and Elderfield H. (1995) Rare earth element geochemistry of hydrothermal
1029 deposits from the active TAG Mound, 26 °N Mid-Atlantic Ridge. *Geochimica et*
1030 *Cosmochimica Acta* 59, 3511-3524.
- 1031 Mills R. A., Teagle D. A. H., and Tivey M. K. (1998) Fluid mixing and anhydrite
1032 precipitation within the TAG mound. In *Proceedings of the Ocean Drilling*
1033 *Program, Scientific Results*, Vol. 158 (ed. P. M. Herzig, S. E. Humphris, D. J.
1034 Miller, and R. A. Zierenberg), pp. 119-127. Ocean Drilling Program.
- 1035 Mottl M. J. and Holland H. D. (1978) Chemical exchange during hydrothermal alteration
1036 of basalt by seawater--I. Experimental results for major and minor components of
1037 seawater. *Geochimica et Cosmochimica Acta* 42(8), 1103-1115.
- 1038 Ohmoto H. and Lasaga A. C. (1982) Kinetics of reactions between aqueous sulfates and
1039 sulfides in hydrothermal systems. *Geochimica et Cosmochimica Acta* 46(10), 1727-
1040 1745.
- 1041 Pearce N. J. G., Perkins W. T., Westgate J. A., Gorton M. P., Jackson S. E., Neal C. R.,
1042 and Chenery S. P. (1997) A compilation of new and published major and trace
1043 element data for NIST SRM 610 and NIST SRM 612 glass reference materials.
1044 *Geostandards Newsletter* 21(1), 115-144.
- 1045 Rees C. E., Jenkins W. J., and Monster J. (1978) The sulphur isotopic composition of
1046 ocean water sulphate. *Geochimica et Cosmochimica Acta* 42(4), 377-381.

1047 Reeves E. (2010) Laboratory and field-based investigations of subsurface geochemical
1048 processes in seafloor hydrothermal systems. Ph.D. Thesis, Massachusetts Institute
1049 of Technology-Woods Hole Oceanographic Institution, Woods Hole, MA.

1050 Roberts S., Bach W., Binns R. A., Vanko D. A., Yeats C. J., Teagle D. A. H., Blacklock
1051 K., Blusztajn J. S., Boyce A. J., and Cooper M. J. (2003) Contrasting evolution of
1052 hydrothermal fluids in the PACMANUS system, Manus Basin: The Sr and S
1053 isotope evidence. *Geology* 31(9), 805-808.

1054 Rye R. O. (2005) A review of the stable-isotope geochemistry of sulfate minerals in
1055 selected igneous environments and related hydrothermal systems. *Chemical*
1056 *Geology* 215, 5-36.

1057 Scott S. D. and Binns R. A. (1995) Hydrothermal processes and contrasting styles of
1058 mineralization in the western Woodlark and eastern Manus basins of the western
1059 Pacific. In *Hydrothermal Vent and Processes, Geological Society of London*
1060 *Special Publication*, Vol. 87 (ed. L. M. Parson, C. L. Walker, and D. R. Dixon), pp.
1061 191-205.

1062 Seewald J. S., Reeves E., Saccocia P., Rouxel O. J., Walsh E., Price R. E., Tivey M., Bach
1063 W., and Tivey M. (2006) Water-rock reaction, substrate composition, magmatic
1064 degassing, and mixing as major factors controlling vent fluid compositions in
1065 Manus Basin hydrothermal systems. *EOS Trans. AGU. Fall Meet. Suppl.*, 87(52),
1066 Abstract # B34A-02.

- 1067 Seyfried W. E., Jr. (1987) Experimental and theoretical constraints on hydrothermal
1068 alteration processes at mid-ocean ridges. *Annual Review of Earth and Planetary*
1069 *Sciences* 15, 317-335.
- 1070 Shanks W. C., III. (2001) Stable Isotopes in Seafloor Hydrothermal Systems: Vent fluids,
1071 hydrothermal deposits, hydrothermal alteration and microbial processes. *Reviews in*
1072 *Mineralogy and Geochemistry* 43, 469-525.
- 1073 Shanks W. C., III, Bischoff J. L., and Rosenbauer R. J. (1981) Seawater sulfate reduction
1074 and sulfur isotope fractionation in basaltic systems: Interaction of seawater with
1075 fayalite and magnetite at 200-350 °C. *Geochimica et Cosmochimica Acta* 45, 1977-
1076 1995.
- 1077 Shanks W. C., III, Bohlke J. K., and Seal R. R. (1995) Stable isotopes in mid-ocean ridge
1078 hydrothermal systems: Interaction between fluids, minerals and organisms. In
1079 *Seafloor Hydrothermal Systems: Physical, Chemical, Biological and Geological*
1080 *Interactions. Geophysical Monograph.*, Vol. 91 (ed. S. E. Humphris, R. A.
1081 Zierenberg, L. S. Mullineaux, and R. E. Thomson), pp. 194-221. American
1082 Geophysical Union.
- 1083 Sinton J. M., Ford L. L., Chappell B., and McCulloch M. T. (2003) Magma genesis and
1084 mantle heterogeneity in the Manus Back-Arc Basin, Papua New Guinea. *Journal of*
1085 *Petrology* 44, 159-195.
- 1086 Sverjensky D. A. (1984) Europium redox equilibria in aqueous solution. *Earth and*
1087 *Planetary Science Letters* 67, 70-78.
- 1088 Taylor B. (1979) Bismarck Sea; Evolution of a back-arc basin. *Geology* 7, 171-174.

1089 Teagle D. A. H., Alt J. C., Chiba H., and Halliday A. N. (1998) Dissecting an active
1090 hydrothermal deposit: The strontium and oxygen isotopic anatomy of the TAG
1091 hydrothermal mound - Anhydrite. In *Proceedings of the Ocean Drilling Program,*
1092 *Scientific Results*, Vol. 158 (ed. P. M. Herzig, S. E. Humphris, D. J. Miller, and R.
1093 A. Zierenberg), pp. 129-141. Ocean Drilling Program.

1094 Thompson G., Humphris S. E., Schroeder B., Sulanowska M., and Rona P. A. (1988)
1095 Active vents and massive sulfides at 26 °N (TAG) and 23 °N (Snakepit) on the
1096 mid-Atlantic Ridge. *Canadian Mineralogist* 26, 697-711.

1097 Tivey M. A., Bach W., Seewald J. S., Tivey M. K., Vanko D. A., and Shipboard Science
1098 and Technical Teams. (2007) Cruise Report R/V Melville, MAGELLAN-06.
1099 Hydrothermal systems in the Eastern Manus Basin: Fluid chemistry and magnetic
1100 structures as guides to seafloor processes, pp. 67. Woods Hole Oceanographic
1101 Institution.

1102 Tivey M. K., Humphris S. E., Thompson G., Hannington M. D., and Rona P. A. (1995)
1103 Deducing patterns of fluid flow and mixing within the TAG active hydrothermal
1104 mound using mineralogical and geochemical data. *Journal of Geophysical*
1105 *Research* 100(B7), 12527-12555.

1106 Tivey M. K., Mills R. A., and Teagle D. A. H. (1998) Temperature and salinity of fluid
1107 inclusions in anhydrite as indicators of seawater entrainment and heating within the
1108 TAG active mound. In *Proceedings of the Ocean Drilling Program, Scientific*
1109 *Results*, Vol. 158 (ed. P. M. Herzig, S. E. Humphris, D. J. Miller, and R. A.
1110 Zierenberg), pp. 179-190. Ocean Drilling Program.

1111 Vanko D. A., Bach W., Roberts S., Yeats C. J., and Scott S. D. (2004) Fluid inclusion
1112 evidence for subsurface phase separation and variable fluid mixing regimes beneath
1113 the deep-sea PACMANUS hydrothermal field, Manus Basin back arc rift, Papua
1114 New Guinea. *Journal of Geophysical Research* 109, B03201,
1115 doi:10.1029/2003JB002579.

1116 Von Damm K. L. (1995) Controls on the chemistry and temporal variability of seafloor
1117 hydrothermal fluids. In *Seafloor Hydrothermal Systems: Physical, Chemical,*
1118 *Biological and Geological Interactions. Geophysical Monograph.*, Vol. 91 (ed. S.
1119 E. Humphris, R. A. Zierenberg, L. S. Mullineaux, and R. E. Thomson), pp. 222-
1120 247. American Geophysical Union.

1121 Von Damm K. L., Buttermore L. G., Oosting S. E., Bray A. M., Fornari D. J., Lilley M.
1122 D., and Shanks W. C., III. (1997) Direct observation of the evolution of a seafloor
1123 "black smoker" from vapor to brine. *Earth and Planetary Science Letters* 149, 101-
1124 112.

1125 Yeats C. J., Bach W., Vanko D. A., Roberts S., Lackschewitz K. S., and Paulick H. (2001)
1126 Fluid-dacite interaction in the PACMANUS subseafloor hydrothermal system -
1127 preliminary results from secondary mineral chemistry and geochemical modeling.
1128 *EOS Trans. AGU. Fall Meet. Suppl.*, 82(47), Abstract # OS11A-0346.

1129 Yeats C. J., Binns R. A., and Parr J. M. (2000) Advanced argillic alteration associated with
1130 actively forming submarine polymetallic sulfide mineralization in the eastern
1131 Manus Basin, Papua New Guinea. *Geological Society of Australia Abstracts* 59,
1132 555.

1133

1134

Fig. 1. Regional tectonic setting of the Manus Basin, Papua New Guinea. Major plates and active plate motions are indicated (solid gray arrows). Seafloor spreading between the Willaumez and Djaul transform faults (Manus Spreading Center) is accommodated by eruption of oceanic crust of predominantly basaltic composition. Extension in the Eastern Manus Basin between the Djaul and Weitin transform faults is accommodated primarily by rifting of existing arc crust of predominantly felsic (andesite, dacite and rhyolite) composition. Locations of major active hydrothermal systems are shown by the yellow stars: Vienna Woods (Manus Spreading Center), and PACMANUS, DESMOS and SuSu Knolls (Eastern Manus Basin). Drilling of an active hydrothermal system in the Manus Basin was carried out by ODP Leg 193 at PACMANUS (Binns et al., 2007).

Fig. 2. Distribution of known vent deposits at PACMANUS (a) and SuSu Knolls (b). Yellow stars indicate vent areas from which anhydrite was sampled and analyzed for this study. Anhydrite samples were recovered from the sub-seafloor by drilling beneath Snowcap and Roman Ruins (ODP Leg 193). Seafloor surface massive anhydrite samples were recovered from Fenway and North Su by ROV operations. Seafloor bathymetry based on EM300 SeaBeam sonar (modified from Tivey et al., 2007).

Fig. 3. Photographs of (a) drill core sample showing 2 to 3 mm thick white anhydrite-pyrite vein cutting through altered volcanic rock. In many specimens, anhydrite veins are surrounded by alteration halos (dashed lines) consisting of cyclic layers of silica-clay (alternating layers with varying shades of gray reflecting different proportions of fine-grained silica and clay). Sample 193-1188F-2Z-1, 80-91 cm, 222.3 mbsf, Snowcap vent field,

PACMANUS. Modified after Binns et al (2007). (b) Typical massive anhydrite exposed on the seafloor at the Fenway active mound, PACMANUS. (c) Cross-section through crustiform massive anhydrite recovered from the North Su vent field, SuSu Knolls. Sample J2-227-7-R1. anh is anhydrite, py is pyrite, cpy is chalcopyrite.

Fig. 4. Chondrite-normalized REE_N patterns of anhydrite samples recovered beneath the Roman Ruins vent field, PACMANUS. (a) Sample 193-1189A-3R-1, 89-93 cm, 20 mbsf; (b) Sample 193-1189A-7R-1, 19-23 cm, 58 mbsf; (c) Sample 193-1189A-10R-1, 42-44 cm, 118 mbsf; (d) Sample 193-1189A-14R-2, 0-3 cm, 158 mbsf. Each data series (line connected symbols) represents a separate microchemical analysis. Data series with the same symbols are analyses from within the same grain. Different symbols denote microchemical analyses from different grains. REE_N patterns of most anhydrite grains are light-REE enriched with a positive Eu-anomaly. Note the pronounced negative Eu-anomaly of REE-rich anhydrite grains in sample 193-1189A-14R-2, 0-3 cm recovered from a depth \sim 158 mbsf (d). Chondritic values are from Anders and Grevesse (1989). For comparison REE_N patterns of contemporary hydrothermal fluids from Roman Ruins are illustrated in Fig. 12.

Fig. 5. Chondrite-normalized REE_N patterns of anhydrite samples recovered beneath the Snowcap vent field, PACMANUS. (a) Sample 193-1188A-7R-1, 66-68 cm, 50 mbsf; (b) Sample 193-1188A-15R-1, 14-20 cm, 126 mbsf; (c) Sample 193-1188A-16R-2, 109-111 cm, 137 mbsf; (d) Sample 193-1188A-17R-2, 6-9 cm, 146 mbsf; (e) Sample 193-1188F-1Z-2, 32-34 cm, 219 mbsf; (f) Sample 193-1188F-1Z-4, 100-104 cm, 223 mbsf; (g) Sample 193-1188F-23Z-2, 22-26 cm, 289 mbsf; (h) Sample 193-1188F-26Z-1, 62-69 cm, 300 mbsf. Each

data series (line connected symbols) represents a separate microchemical analysis. Data series with the same symbols are analyses from within the same grain. REE_N patterns range from light-REE enriched with a positive Eu-anomaly, to heavy-REE enriched with a positive Eu-anomaly, to relatively flat and uniformly REE-enriched with no clear Eu-anomaly. REE concentrations and REE_N patterns differ markedly among and within anhydrite samples from different depths and lithologies. Although there is no clear relationship between REE_N pattern type and either depth or alteration lithology, the wide range of REE_N patterns observed in Snowcap anhydrite samples is an indicator of highly variable hydrothermal conditions that is responsible for the range of alteration sequences observed in Snowcap drill core (see text for discussion). Chondritic values are from Anders and Grevesse (1989). For comparison REE_N patterns of contemporary hydrothermal fluids from Snowcap are illustrated in Fig. 12.

Fig. 6. Chondrite-normalized REE_N patterns of representative massive anhydrite samples exposed on the seafloor at the Fenway active mound, PACMANUS. (a) J2-210-8-R1; (b) J2-210-8-R2; (c) J2-216-1-R1. Each data series (line connected symbols) represents a separate microchemical analysis. Data series with the same symbols are analyses from within the same grain. All massive anhydrite samples recovered from Fenway have very similar REE_N patterns. Chondritic values are from Anders and Grevesse (1989). For comparison REE_N patterns of contemporary hydrothermal fluids from Fenway are illustrated in Fig. 12.

Fig. 7. Chondrite-normalized REE_N patterns measured in massive anhydrite (J2-227-7-R2) sampled at the North Su vent field, SuSu Knolls. Each data series (line connected symbols) represents a separate microchemical analysis. Data series with the same symbols are analyses

from within the same grain. Different symbols identify microchemical analyses from different grains in this sample. REE_N patterns are notable for their inter- and intra-grain variability. The range of REE_N patterns documented suggests that this sample records mineralization from hydrothermal fluids with varying compositions. See text for discussion. Chondritic values are from Anders and Grevesse (1989). For comparison REE_N patterns of contemporary hydrothermal fluids from North Su are illustrated in Fig. 12.

Fig. 8. Microchemical mapping of Roman Ruins drill-core anhydrite sample 1189B-14R-2, 0-3cm, 158 mbsf. (a) Cathodoluminescence (CL) imaging. Pink-tan and green colors designate grain domains with high ($\sum\text{REE} \geq 50$ ppm) and low concentrations ($\sum\text{REE} < 10$ ppm) of REEs, respectively. A grain identified for chemical and isotopic analysis is indicated by the thick dashed white line. Yellow stars record areas (spots 1–6) where microchemical analyses by laser ablation ICPMS and MC-ICPMS were performed. CL imaging reveals the sharp boundary between REE-rich (core) and REE-poor domains (rim). (b) Reflected light photomicrograph of the grain of interest after laser ablation analyses. The thick dashed white line designates the grain identified by CL in (a). Dashed white boxes show raster pits from laser ablation analyses. The gold coating is that used in preparation of this sample for an unrelated ion microprobe study. (c) Chondrite-normalized REE_N patterns obtained by microchemical analysis (spots 1-6) compared with the bulk (Bach et al. 2003). High REE concentrations in this sample (spots 3-5) are directly correlated with pink-tan colors in (a). Conversely, low REE concentrations (spots 1, 2 and 6) are correlated with green colors in (a). Note the significant intra-grain variability exhibited in this sample. (d) Strontium isotopic ratio of anhydrite grain as a function of distance from grain core. Bulk strontium isotopic

composition is shown for comparison (Bach et al. 2003). Strontium isotopic ratios of the grain core (spots 3 and 5) are similar to that of endmember hydrothermal fluid ($^{87}\text{Sr}/^{86}\text{Sr} \sim 0.7042$), whereas those of the grain rim (spots 1, 2 and 6) are closer to that of seawater ($^{87}\text{Sr}/^{86}\text{Sr} \sim 0.70918$). The transition from hydrothermal-dominant to seawater-dominant strontium isotopic ratios is sharp across the same boundary identified by CL in (a). (e) Relationship between measured REE concentration and strontium isotopic ratios in grain of interest. Hydrothermal-dominant domains (core) have high REE concentrations which is consistent with high REE concentrations in endmember hydrothermal fluid relative to that of seawater. Textural characteristics documented by CL and petrographic imaging, including regular grain structures and sharply bounded chemical domains, support primary growth of anhydrite without secondary alteration. There has not likely occurred any chemical and/or isotopic exchange of lattice bound trace elements (e.g., network-modifier REEs and Sr) that would compromise the primary composition of anhydrite.

Fig. 9. Microchemical mapping of Snowcap drill-core anhydrite sample 1188F-1Z-4, 100-104cm, 223 mbsf. (a) Cathodoluminescence (CL) imaging. Pink-tan and green colors designate anhydrite domains with high and low concentrations of REEs, respectively, as shown also in Fig. 8. Yellow stars record areas (spots 1–6, 20-25) where microchemical analyses by laser ablation ICPMS and MC-ICPMS were performed. CL imaging reveals the significant intra-grain variability in REE compositions and the sharp boundary between REE-rich and REE-poor domains. The chemical heterogeneity appears intrinsic to primary growth of anhydrite. (b) Reflected light photomicrograph of the grain of interest after laser ablation analyses. Dashed white boxes show raster pits from laser ablation analyses. The gold coating

is that used in preparation of this sample for an unrelated ion microprobe study. (c) Chondrite-normalized REE_N patterns obtained by microchemical analysis (spots 1-6, 20-25). Note the heterogeneous distribution of the REEs between adjacent anhydrite grains.

Fig. 10. Microchemical mapping of massive anhydrites from Fenway (a,b) and North Su (c,d). Cathodoluminescence (CL) imaging and microchemical analysis reveal significant differences between the growth histories of these samples. Massive anhydrites at Fenway are commonly coarse-grained with no distinct intra-grain chemical heterogeneity (a) and have very uniform chondrite-normalized REE_N patterns (b) similar to that of modern seafloor vent fluids sampled at this vent field. The data are interpreted as reflecting precipitation of anhydrite at Fenway from hydrothermal fluid having a stable composition over timescales of mineral deposition. In contrast, precipitation of anhydrite at North Su is more complex. Massive anhydrite sampled at North Su is characterized by composite banding with each band having distinct range of grain sizes and CL signatures (c). Grains within distinct composite bands have different chondrite-normalized REE_N patterns that show heterogeneity on the grain-scale (d). The REE_N patterns recorded in massive anhydrite are different to that of contemporary black smoker fluids sampled at North Su and are interpreted as reflecting deposition of anhydrite from hydrothermal fluids with very different compositions relative to modern. See text for detailed discussion.

Fig. 11. Strontium ($^{87}\text{Sr}/^{86}\text{Sr}$) and sulfur ($\delta^{34}\text{S}$) isotopic ratios measured in anhydrites from Roman Ruins, Fenway and Snowcap (PACMANUS) and North Su (SuSu Knolls). Data from this study are shown by gray (solid) diamonds and are compared to previous isotopic

measurements of the same samples (open diamonds) determined using bulk sample techniques (Roberts et al., 2003; Bach et al., 2005). Microchemical and whole-rock analysis of strontium (a) and sulfur isotopes (b) yield consistent and similar data, although microchemical analyses document a larger range of absolute isotopic heterogeneity and significant intra-grain isotopic variability that cannot be resolved by whole-rock analyses. Gray bars indicate the strontium and sulfur isotopic compositions of contemporary seawater (SW) and endmember hydrothermal fluids (HF) sampled at PACMANUS and SuSu Knolls.

Fig. 12. Chondrite-normalized REE_N patterns of modern seafloor hydrothermal fluids sampled from the PACMANUS and SuSu Knolls vent fields (data from Craddock et al., 2010). (a) Sampled vent fluids at PACMANUS (Roman Ruins, Fenway and Snowcap) are black- and gray-smoker fluids with REE_N patterns characterized by a light-REE enrichment and positive Eu anomaly. (b) Sampled vent fluids at SuSu Knolls (North Su) include both high-temperature black-smoker fluids and acid-sulfate fluids. Smoker fluids have a REE_N pattern characterized by a light-REE enrichment and positive Eu anomaly, similar to that measured in smoker fluids sampled at PACMANUS. Acid-sulfate fluids have different REE_N patterns that, in the most acidic fluids, are relatively flat without any REE anomalies. Also shown for comparison is the REE_N pattern of an atypical fluoride-rich low-temperature fluid sampled from the Suzette vent field adjacent to North Su. All REE concentrations, except for in acid-sulfate fluids, are endmembers extrapolated to zero Mg. Acid-sulfate REE concentrations are reported at the lowest measured Mg. See Table 2 for full fluid compositions. See text for discussion of the implications for the similar REE_N patterns documented in anhydrites and vent fluids sampled at PACMANUS and SuSu Knolls.

Fig. 13. La/Yb and Eu/Eu* ratios in anhydrite from Fenway (a), Roman Ruins (b), Snowcap (c) and North Su (d) normalized to REE compositions of contemporary hydrothermal fluid (black-/gray-smokers) sampled at the same vent fields. See Table 2 for fluid compositions. In each plot, symbols refer to data obtained for different samples. Bold black lines define $(La/Yb)_{Anh/BSF} = 1$ and $(Eu/Eu^*)_{Anh/BSF} = 1$ and identify where anhydrite samples would cluster if fluid and anhydrite REE compositions are the same. The REE compositions of Fenway massive anhydrites are most similar to that of contemporary smoker vent fluids and so cluster around $(La/Yb)_{Anh/BSF} = 1$ and $(Eu/Eu^*)_{Anh/BSF} = 1$. Drill-core anhydrites from Roman Ruins cluster about $(La/Yb)_{Anh/BSF} = 1$, but show a pronounced negative Eu-anomaly. Samples from both Snowcap and North Su have a range of REE compositions markedly different from that of contemporary smoker vent fluids and suggest a genetic disconnect between anhydrite and contemporary fluids.

Fig. 14. Sr versus S isotopic ratios measured in anhydrite samples from Roman Ruins (gray triangles), Fenway (hatched diamonds), Snowcap (gray circles) and North Su (crossed squares). The isotopic composition of seawater is shown by the black star ($^{87}Sr/^{86}Sr = 0.70918$, $\delta^{34}S = +21$ ‰). Sr and S isotopic data obtained by whole-rock analysis of the same samples are shown by the open symbols (Roberts et al. 2003). Dashed lines are conservative mixing trends between seawater and modeled magmatic-hydrothermal fluids with a range of “magmatic” sulfate concentrations. Checkmarks define the percent fraction of seawater in the mixed fluid (10% increments). Concentrations of Sr and sulfate in seawater are 91 $\mu\text{mol/kg}$ and 28.2 mmol/kg , respectively. Shown are two mixing lines between seawater and modeled

black smoker fluids containing 0 and 15 mmol/kg of magmatic sulfate with an isotopic composition of $\delta^{34}\text{S} = +8 \text{ ‰}$. The concentration and isotopic ratio of Sr in modeled black smoker fluids is 240 $\mu\text{mol/kg}$ and $^{87}\text{Sr}/^{86}\text{Sr} = 0.7042$. Also shown is projected mixing line for seawater and modeled acid-sulfate fluid containing 150 mmol/kg of sulfate with an isotopic composition of $\delta^{34}\text{S} = +8 \text{ ‰}$ (in the absence of typical high-temperature smoker fluid activity). The concentration and isotopic ratio of Sr in modeled acid-sulfate fluids is $< 50 \mu\text{mol/kg}$ and $^{87}\text{Sr}/^{86}\text{Sr} = 0.7042$. For comparison, see Table 2 for the compositions of sampled fluids. The Sr and S isotopic composition of most anhydrites can be explained by precipitation from a variable mix of seawater and hydrothermal fluid that contains trace or no sulfate. The light S isotopic ratios of some anhydrites from Snowcap are, however, best modeled by mixing between seawater and a hydrothermal fluid containing measurable ($\sim 15 \text{ mmol/kg}$) sulfate of magmatic origin. The presence of significant sulfate of magmatic origin in Snowcap fluids implies the existence of acid-sulfate type fluids at this vent field in the recent geologic past. See text for discussion.

Table 1. Typical operating parameters for laser ablation ICPMS and MC-ICPMS

	Rare Earth Elements	Sr Isotopes	S Isotopes
<i>Mass spectrometer setup</i>			
Instrument	Thermo Scientific ELEMENT2	Thermo Scientific NEPTUNE	Thermo Scientific NEPTUNE
RF Power	1200 W	1200 W	1200 W
Cooling gas	16 L/min, Ar	15 L/min, Ar	15 L/min, Ar
Auxiliary gas	1.0 L/min, Ar	0.8 L/min, Ar	0.8 L/min, Ar
Sample gas	0.8–0.9 L/min, Ar	0.8–0.9 L/min, Ar	0.8–0.9 L/min, Ar
Carrier (add.) gas	0.35–0.4 L/min, He	0.35–0.4 L/min, He	0.35–0.4 L/min, He
Interface cones	H-cones, Ni	X-cones, Ni	X-cones, Ni
Resolution mode	Low (400)	Low (400)	High (10,000)
Nebulizer	-	Elemental Scientific, Inc., PFA-50	Elemental Scientific, Inc., PFA-50
Introduction System	-	Elemental Scientific, Inc., Cyclonic spray chamber	Elemental Scientific, Inc., Cyclonic spray dual chamber
Sensitivity, laser	~ 10 ⁴ cps per ppm (¹³⁹ La)	~ 0.25 V per 100 ppm (⁸⁸ Sr)	~ 8 mV per 100 ppm (³² S)
<i>Data acquisition parameters</i>			
Counting mode	SEM	Analog, static amplifiers	Analog, static amplifiers
Method	30 cycles, 2 sec per cycle	20 cycles, 8.5 sec per cycle	20 cycles, 8.5 sec per cycle
Acquisition time	70 sec	170 sec	170 sec
Wash-out time	180 sec	240 sec	240 sec
<i>Laser setup</i>			
Laser	New Wave UP213 (quad Nd:YAG)	New Wave UP213 (quad Nd:YAG)	New Wave UP213 (quad Nd:YAG)
Carrier gas	He	He	He
Beam optics	Apertured	Apertured	Apertured
Beam diameter	30 μm	60 μm	60 μm
Pulse rate	10 Hz	10 Hz	10 Hz
Laser intensity	65 % (~ 0.4 mJ)	60 % (~ 0.3 mJ)	50–70 % (~ 0.3–0.4 mJ)
Scan mode	Raster	Raster	Raster
Raster parameters	area 180 x 80 μm, line spacing 15 μm	area 180 x 80 μm, line spacing 15 μm	area 180 x 80 μm, line spacing 15 μm
Scan speed	20 μm/sec	5 μm/sec	5 μm/sec
Pre-ablation	scan speed 60 μm/sec, intensity 40 %	scan speed 30 μm/sec, intensity 40 %	scan speed 30 μm/sec, intensity 40 %
Ablation time	20 sec (pre-ablation); 61 sec (ablation)	40 sec (pre-ablation); 244 sec (ablation)	40 sec (pre-ablation); 244 sec (ablation)

Table 2. Summary of hydrothermal fluid and seawater compositions sampled from Manus Basin, Papua New Guinea*

Sample	Vent Area	T _{max} (°C)	pH (25°C)	Mg _{min} (mM)	Cl (mM)	F (µM)	SO ₄ (mM)	H ₂ S (mM)	Sr (µM)	⁸⁷ Sr/ ⁸⁶ Sr	REE (pM)												
											La	Ce	Pr	Nd	Sm	Eu	Gd	Tb	Dy	Ho	Er	Yb	Lu
<i>Black/gray Smoker fluids</i>																							
RMR1	Roman Ruins	314	2.3	7.3	619	120	0.9	6.5	80	nd	8493	10417	837	2225	520	6848	187	27	132	21	57	65	nd
	Endmember			0.0	632	135	-	7.5	74	-	9918	12164	977	2599	607	7996	219	31	154	24	67	76	-
RMR4	Roman Ruins	341	2.6	3.6	650	125	0.4	6.3	87	0.70460	12500	22500	2830	10213	2075	11182	1324	154	685	97	228	191	nd
	Endmember			0.0	658	126	-	6.8	87	0.7042	13262	23871	3002	10835	2201	11863	1405	164	727	103	242	202	-
F2	Fenway	343	2.6	4.7	686	173	1.5	9.2	116	nd	19716	33980	3982	14465	2851	8514	1979	250	1210	165	405	314	nd
	Endmember			0.0	699	181	-	10.1	122	-	21528	37103	4348	15794	3113	9296	2161	273	1321	180	442	343	-
F3	Fenway	358	2.7	4.5	585	160	2.2	17.2	95	0.70428	15000	27172	3400	14000	3400	7750	2750	320	1500	205	470	290	nd
	Endmember			0.0	562	172	-	18.8	96	0.7042	16318	29560	3699	15230	3699	8431	2992	348	1632	223	511	315	-
SC1	Snowcap	152	4.6	30.8	500	128	11.4	2.9	43	nd	221	411	46	176	83	105	58	16	112	26	83	70	nd
	Endmember			0.0	441	220	-	7.0	-	-	499	928	103	396	186	237	130	35	251	58	188	158	-
SC2	Snowcap	180	3.4	24.2	531	170	5.5	0.5	56	0.70635	352	827	70	284	56	140	50	12	70	16	40	40	nd
	Endmember			0.0	526	259	-	1.9	25	-	619	1454	123	500	99	246	88	21	123	28	70	70	-
NS3	North Su	300	3.4	1.6	644	144	1.3	3.4	237	0.70444	10689	18408	2075	6913	840	3089	424	41	179	29	66	60	nd
	Endmember			0.0	647	144	-	3.4	238	0.7044	10689	18408	2075	6913	840	3089	424	41	179	29	66	60	-
SZ5	Suzette	249	2.3	6.4	610	480	3.0	4.8	234	0.70520	2400	4094	668	3979	2561	1304	4005	739	4637	864	2486	2076	nd
	Endmember			0.0	619	533	-	5.3	243	0.7049	2711	4625	755	4495	2893	1473	4525	834	5239	976	2808	2345	-
<i>Acid-sulfate fluids</i>																							
NS1	North Su	48	1.8	59.0	520	50	41	0.6	85	0.7089	10923	35507	4755	19616	4699	1782	4452	718	4452	876	2793	2846	nd
NS2	North Su	215	0.9	38.8	442	103	149	0.0	58	0.7087	25597	98058	16244	83537	25511	8865	26764	4323	26644	5155	15724	15225	nd
<i>Seawater</i>																							
Bottom seawater		2	8.1	52.7	543	66	28.2	0.0	91	0.70918	32.3	4.9		22.9	4.5	1.2	6.4		6.9		6.0	6.0	0.98

* Data for Mg, Sr, Cl, F, SO₄ and H₂S reported by Craddock (2009) and Reeves (2010). Data for rare earth elements in hydrothermal fluids reported by Craddock et al. (2010) and in seawater are averages of data reported by Mitra et al. (1994). Mg_{min} is the lowest measured Mg of fluids sampled in replicate from each vent orifice. pH (25 °C) is the lowest pH of fluid measured at room temperature. Endmember compositions for black/gray smoker fluids are sampled fluid compositions extrapolated to zero Mg. mM = mmol/kg, µM = µmol/kg, pM = pmol/kg, nd = no data.

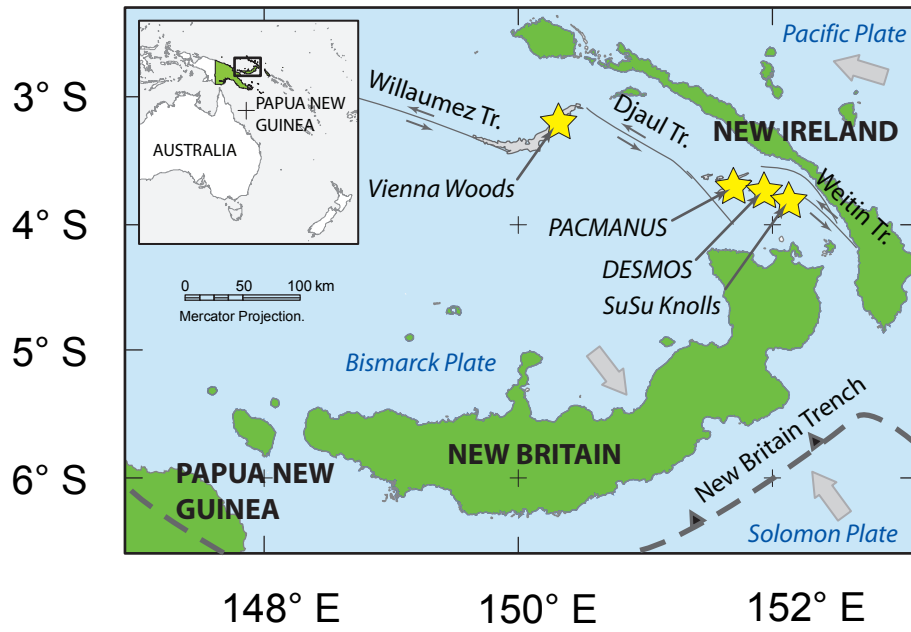


Fig. 1

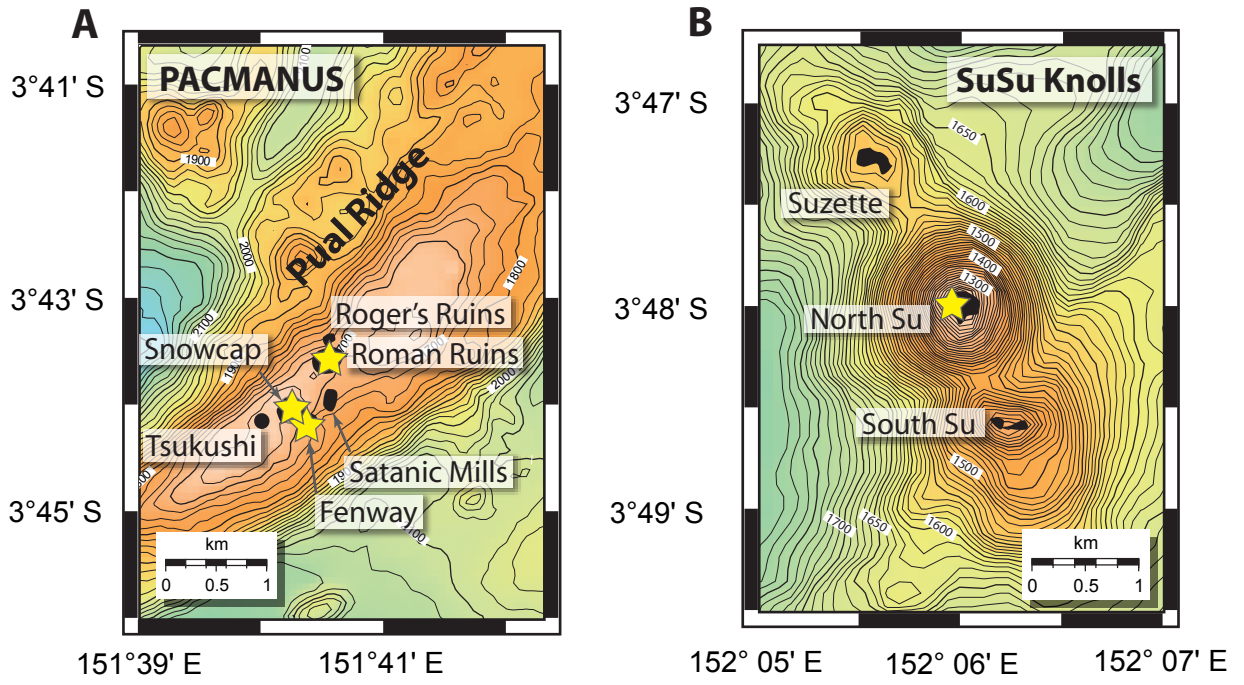


Fig. 2

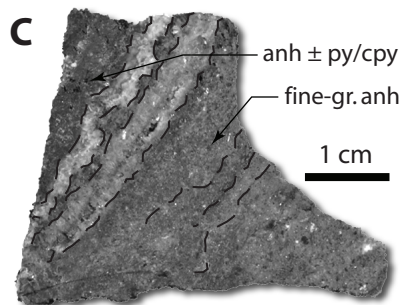
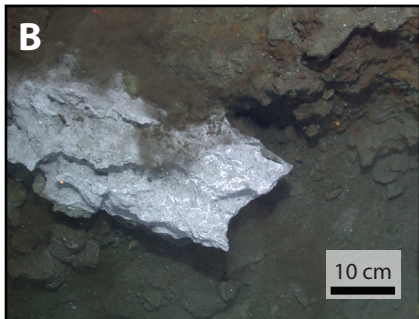
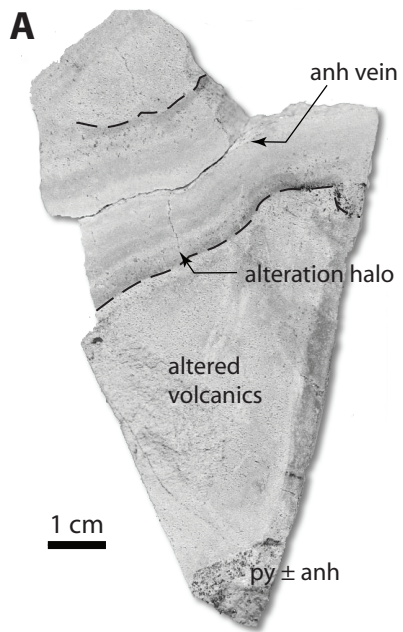


Fig. 3

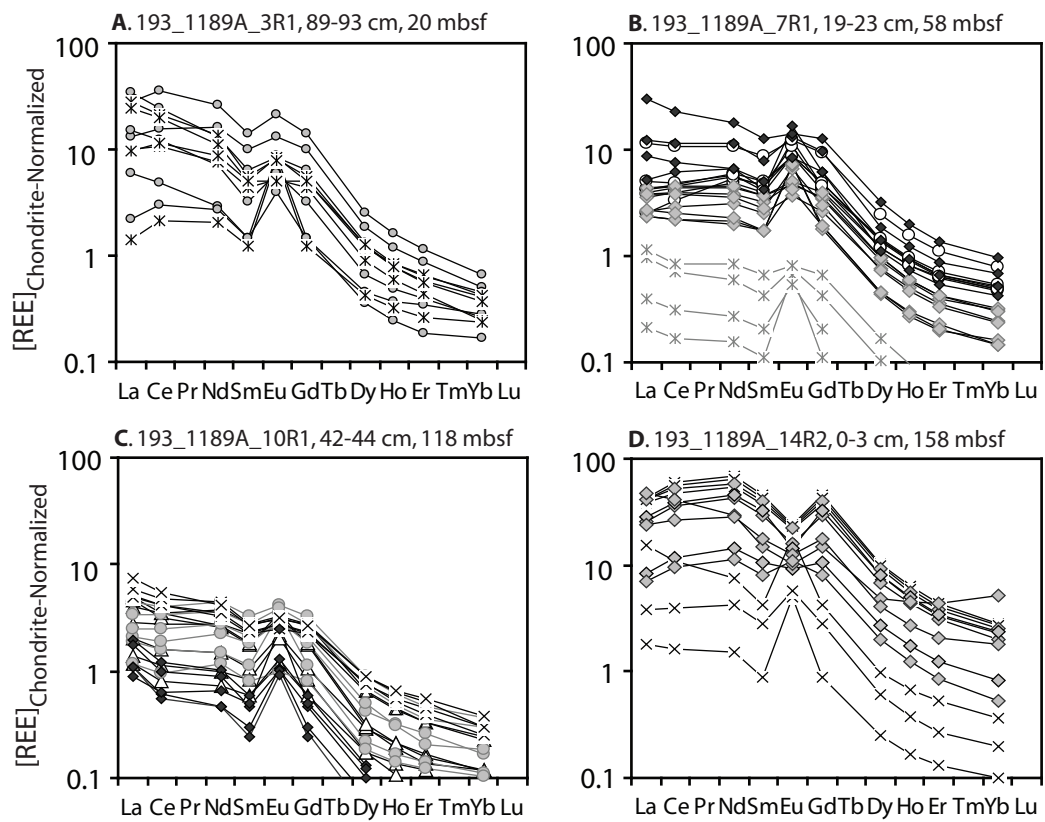


Fig. 4

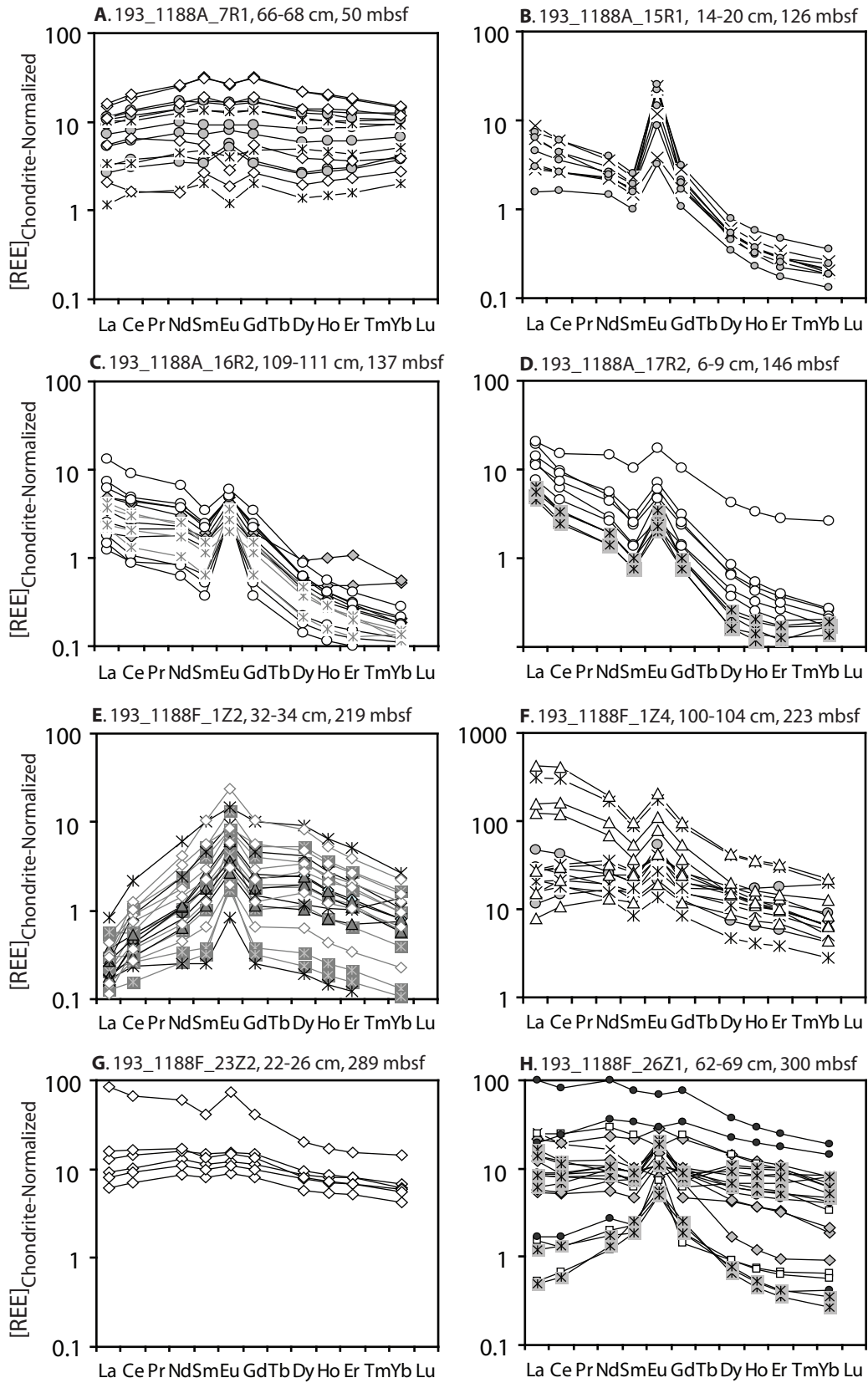


Fig. 5.

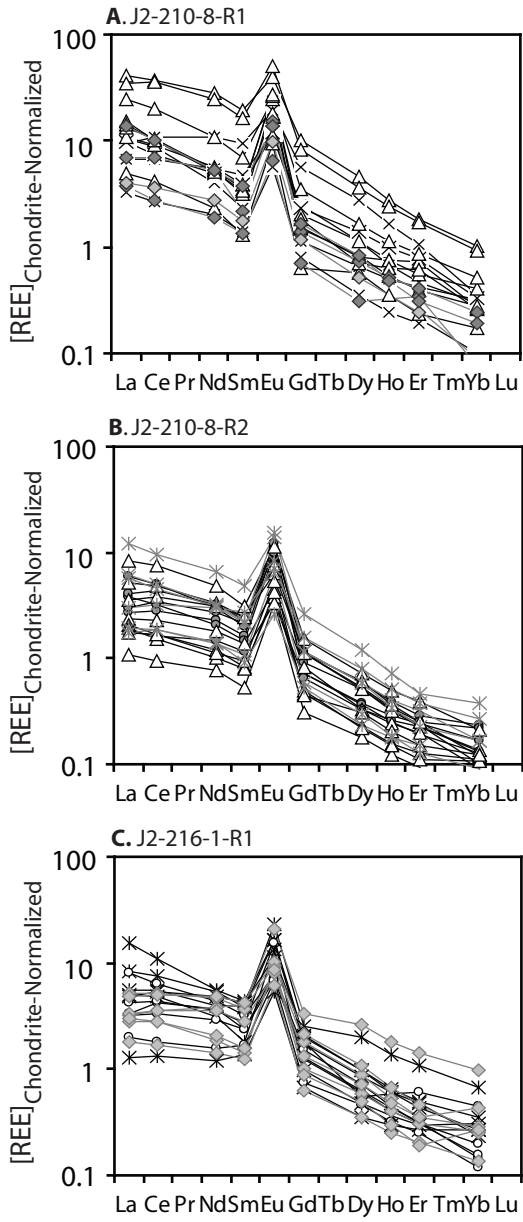


Fig. 6.

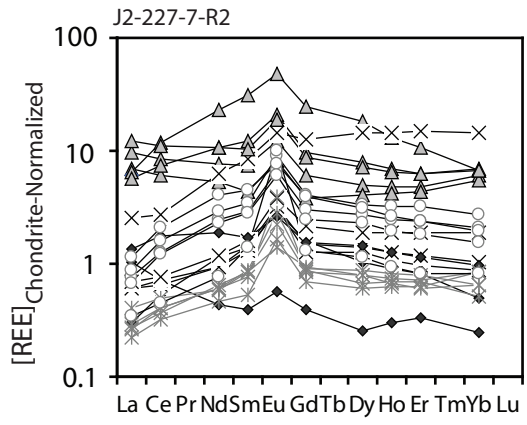


Fig. 7

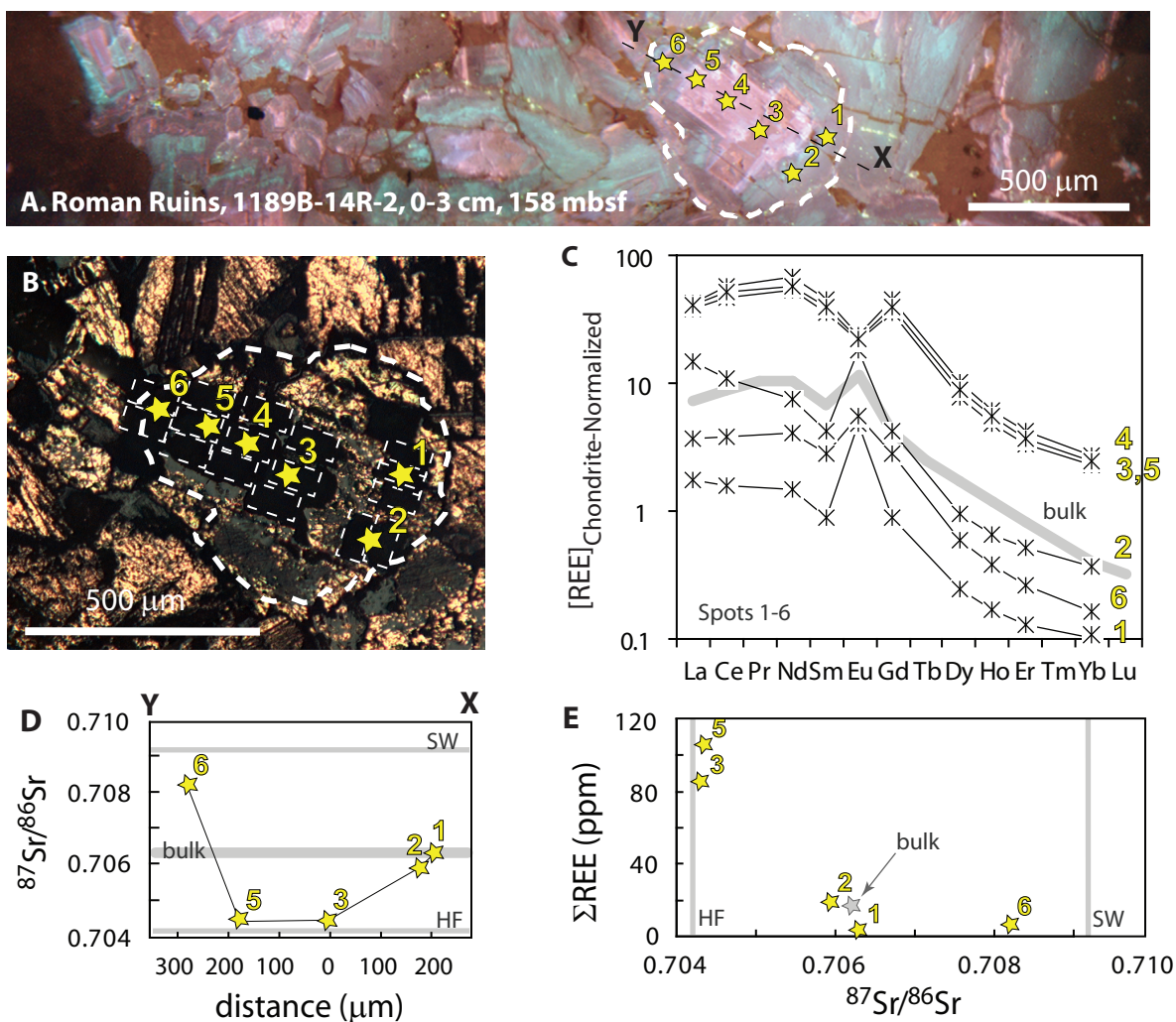


Fig. 8

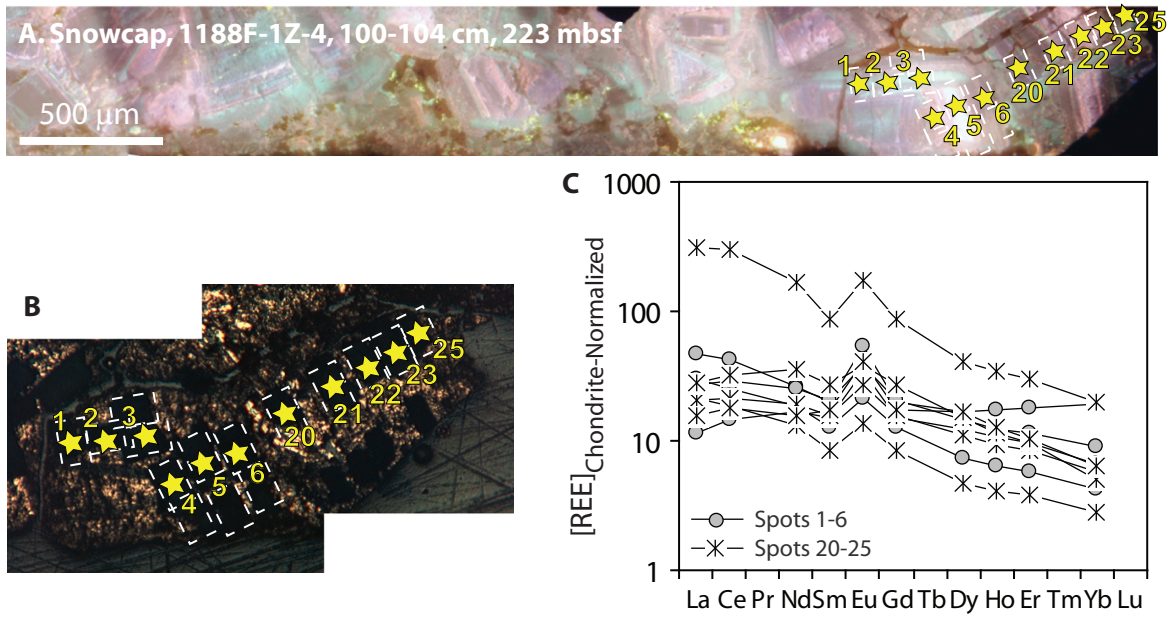


Fig. 9

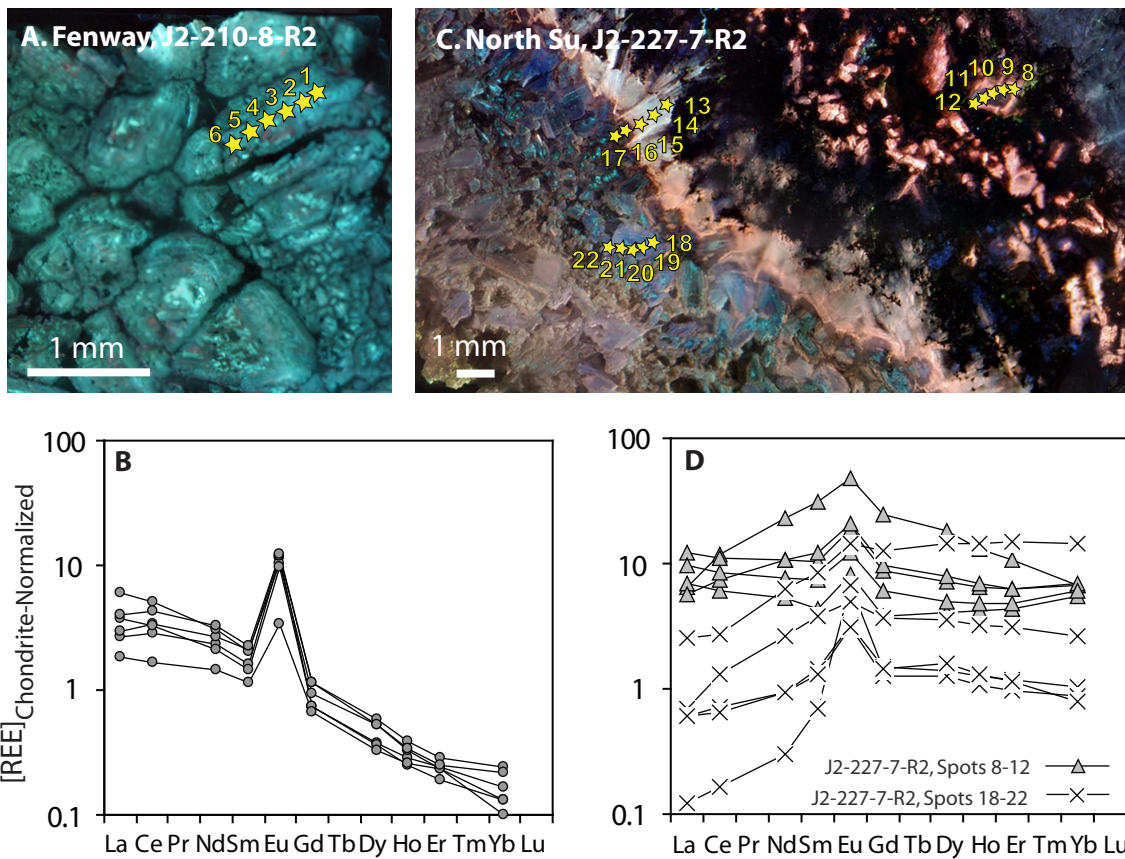


Fig. 10

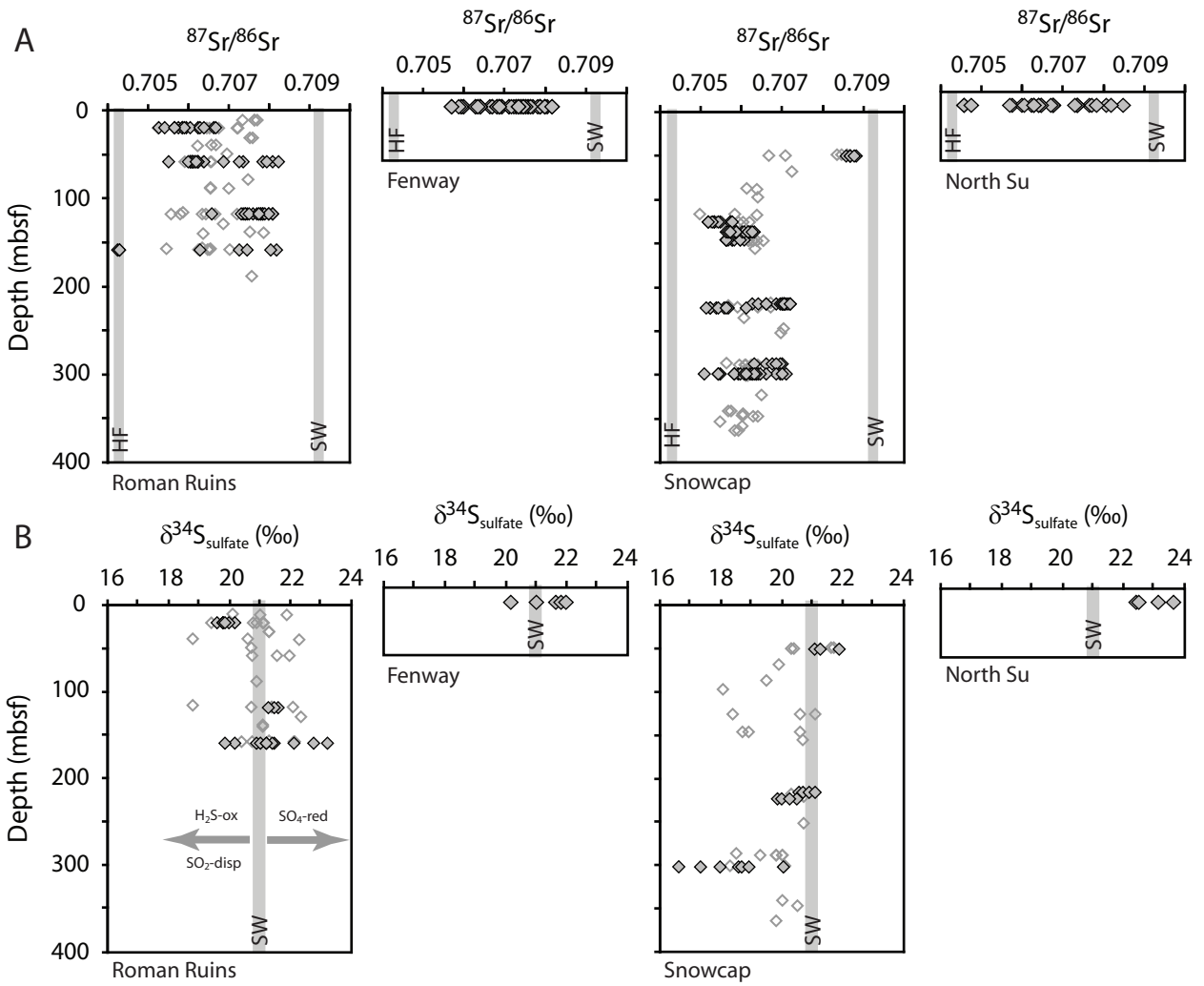


Fig. 11

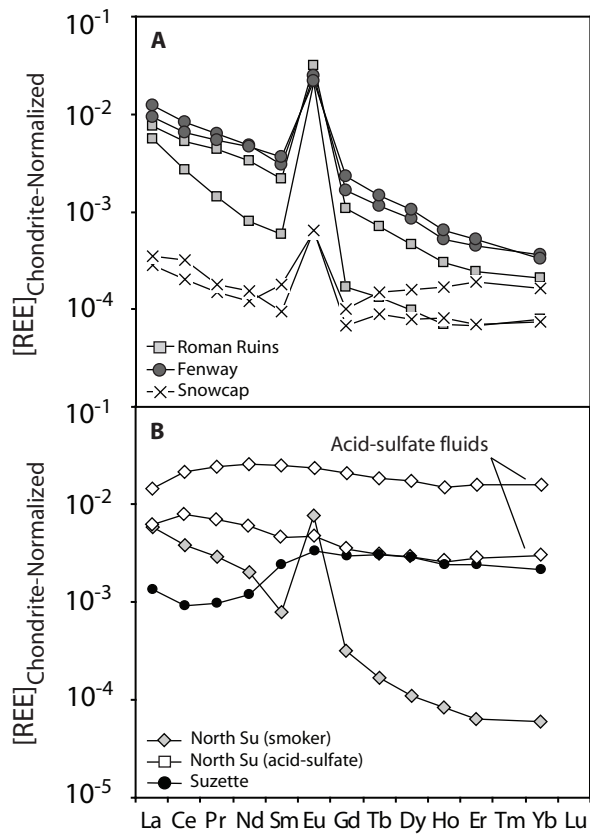


Fig. 12

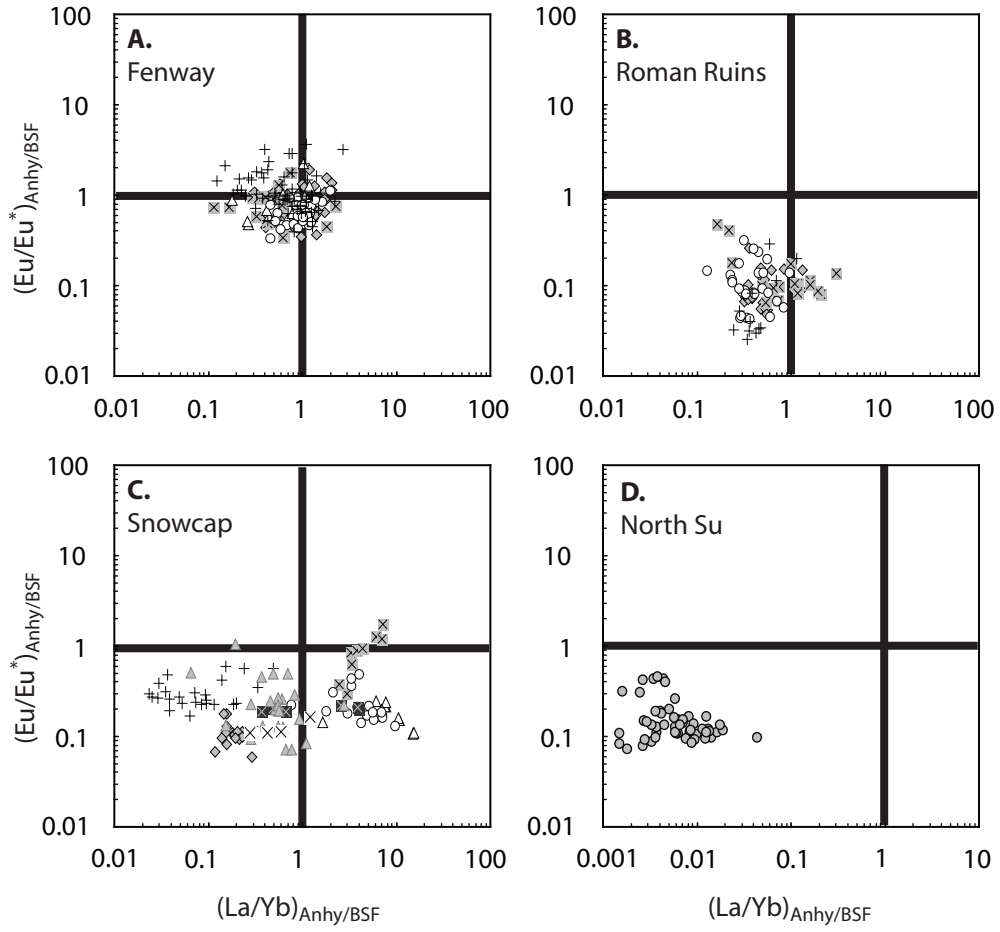


Fig. 13

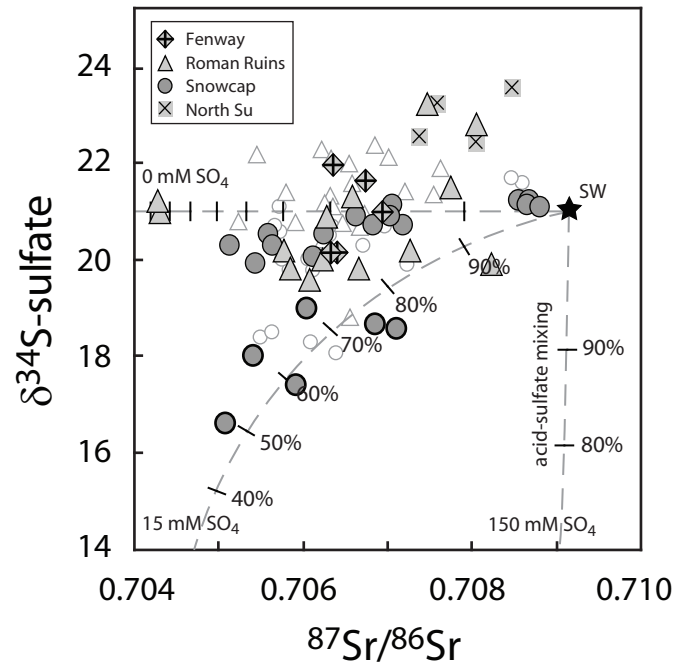


Fig. 14

Supporting Online Material to accompany Craddock P.R. and Bach W. Insights to Magmatic–Hydrothermal Processes in the Manus back–arc Basin as Recorded by Anhydrite

Table S1. Trace element (Sr, Mg, Ba, REE) and isotopic (Sr, S) compositions of anhydrites sampled in the Manus Basin, Papua New Guinea. Concentrations given in parts per million (ppm).

	Sr	Mg	Ba	La	Ce	Pr	Nd	Sm	Eu	Gd	Tb	Dy	Ho	Er	Yb	Lu	ΣREE	La _N /Yb _N	Sm _N /Yb _N	Eu _N /Eu* _N	⁸⁷ Sr/ ⁸⁶ Sr	δ ³⁴ S (‰)
Snowcap, 193_1188A_7R_1, 66-68cm, 50mbsf																						
Spot #1	2664	3	18	0.77	2.41	nd	1.96	0.57	0.33	0.84	nd	0.68	0.16	0.50	0.68	nd	9.0	0.8	0.9	1.6	0.70865	21.9
Spot #2	2689	9	23	0.65	1.98	nd	1.68	0.52	0.30	0.76	nd	0.65	0.16	0.48	0.62	nd	7.9	0.7	0.9	1.5	0.70856	21.2
Spot #4	3913	10	64	1.29	3.91	nd	3.53	1.11	0.47	1.64	nd	1.49	0.34	1.00	1.13	nd	16.0	0.8	1.1	1.1	0.70869	21.2
Spot #5	4930	28	115	2.27	6.91	nd	6.53	2.06	0.74	3.01	nd	2.74	0.59	1.69	1.76	nd	28.4	0.9	1.3	0.9	0.70866	21.1
Spot #6	4731	28	111	2.78	8.67	nd	8.10	2.59	0.89	3.79	nd	3.40	0.73	2.11	2.07	nd	35.3	0.9	1.3	0.9	0.70881	21.1
Spot #7	4919	32	103	1.75	5.15	nd	4.63	1.44	0.54	2.25	nd	2.13	0.48	1.43	1.57	nd	21.4	0.8	1.0	1.0	0.70879	
Spot #8	5003	35	94	2.34	6.79	nd	6.16	1.93	0.68	2.91	nd	2.67	0.59	1.70	1.73	nd	27.6	0.9	1.2	0.9		
Spot #19	nd	nd	nd	0.29	1.00	nd	0.80	0.31	0.07	0.46	nd	0.35	0.08	0.26	0.34	nd	4.0	0.6	1.0	0.6		
Spot #20	nd	nd	nd	0.83	2.19	nd	2.15	0.73	0.23	1.08	nd	1.25	0.26	0.73	0.83	nd	10.3	0.7	0.9	0.8		
Spot #21	nd	nd	nd	2.48	6.51	nd	6.06	2.08	0.77	3.06	nd	2.70	0.57	1.59	1.50	nd	27.3	1.1	1.5	1.0		
Spot #22	nd	nd	nd	2.57	7.46	nd	6.54	2.62	0.97	3.86	nd	3.25	0.68	1.85	1.75	nd	31.5	1.0	1.6	1.0		
Spot #23	nd	nd	nd	3.60	11.94	nd	11.83	4.85	1.51	7.14	nd	5.62	1.13	2.92	2.37	nd	52.9	1.0	2.2	0.8		
Spot #24	nd	nd	nd	3.98	12.96	nd	12.39	4.76	1.57	7.01	nd	5.62	1.15	3.06	2.43	nd	54.9	1.1	2.1	0.9		
Spot #25	nd	nd	nd	2.69	8.27	nd	7.51	2.93	0.92	4.32	nd	3.59	0.78	2.23	1.95	nd	35.2	0.9	1.6	0.8		
Spot #26	nd	nd	nd	0.51	1.04	nd	0.75	0.40	0.11	0.59	nd	0.49	0.12	0.39	0.46	nd	4.9	0.8	0.9	0.7		
Spot #27	nd	nd	nd	1.34	4.15	nd	2.86	0.84	0.16	1.23	nd	0.98	0.21	0.60	0.64	nd	13.0	1.4	1.4	0.5		
Snowcap, 193_1188A_15R_1, 14-20cm, 126mbsf																						
Spot #2	2891	4	6	0.68	1.67	nd	1.01	0.22	0.22	0.34	nd	0.13	0.02	0.05	0.03	nd	4.6	14.3	7.4	2.5	0.70570	
Spot #3	2601	14	186	1.51	2.81	nd	1.40	0.30	1.29	0.47	nd	0.13	0.02	0.05	0.03	nd	9.2	29.2	9.2	10.5	0.70532	
Spot #4	2525	12	1073	2.11	3.86	nd	1.71	0.35	1.43	0.57	nd	0.16	0.02	0.06	0.04	nd	11.5	33.3	8.7	9.8	0.70546	
Spot #5	2563	5	314	0.79	1.66	nd	1.06	0.26	0.68	0.35	nd	0.14	0.02	0.05	0.03	nd	5.6	15.6	8.3	6.8	0.70533	
Spot #15	2843	156	170	0.72	1.67	nd	1.10	0.26	0.50	0.34	nd	0.12	0.02	0.04	0.03	nd	5.3	16.0	9.2	5.1	0.70545	
Spot #16	1256	29	6	1.10	2.27	nd	1.22	0.29	0.85	0.43	nd	0.14	0.02	0.05	0.04	nd	7.3	18.2	7.7	7.3	0.70518	
Spot #17	1428	10	8	1.81	3.82	nd	1.85	0.39	1.27	0.63	nd	0.20	0.03	0.08	0.06	nd	11.4	20.7	7.1	7.7	0.70526	
Spot #18	3468	72	69	0.38	1.04	nd	0.68	0.15	0.19	0.22	nd	0.09	0.01	0.03	0.02	nd	3.0	11.9	7.6	3.1	0.70575	
Spot #19	3291	6	1288	1.58	2.76	nd	1.16	0.24	1.45	0.40	nd	0.11	0.02	0.04	0.03	nd	8.9	34.6	8.3	14.2	0.70520	
Snowcap, 193_1188A_17R_2, 6-9cm, 146mbsf																						
Spot #1	12013	5	57	2.93	3.93	nd	1.38	0.22	0.16	0.91	nd	0.11	0.02	0.04	0.03	nd	9.9	72.5	8.5	2.0	0.70599	
Spot #2	13380	5	105	4.65	6.16	nd	2.35	0.37	0.28	1.58	nd	0.17	0.03	0.06	0.04	nd	15.9	73.5	9.3	2.0	0.70604	
Spot #3	7415	7	223	3.40	5.75	nd	2.66	0.49	0.42	1.59	nd	0.22	0.03	0.07	0.04	nd	15.0	51.2	11.6	2.3	0.70578	
Spot #4	7537	7	180	2.68	4.63	nd	2.06	0.39	0.34	1.24	nd	0.16	0.02	0.05	0.04	nd	11.9	50.1	11.5	2.3	0.70577	
Spot #5	8966	5	196	1.86	2.86	nd	1.25	0.21	0.27	0.74	nd	0.09	0.01	0.03	0.03	nd	7.6	36.6	6.7	3.4	0.70583	
Spot #6	3555	1468	21	5.04	9.59	nd	6.93	1.60	0.99	3.61	nd	1.08	0.19	0.46	0.43	nd	30.7	7.9	4.0	1.6	0.70596	
Spot #9	5205	25	98	1.53	2.15	nd	0.92	0.15	0.17	0.46	nd	0.06	0.01	0.03	0.03	nd	5.7	35.9	5.6	3.1	0.70563	
Spot #10	5126	9	143	1.55	2.20	nd	0.90	0.15	0.20	0.49	nd	0.06	0.01	0.02	0.03	nd	5.8	36.7	5.6	3.6	0.70562	
Spot #11	4582	11	80	1.25	1.67	nd	0.67	0.12	0.14	0.30	nd	0.04	0.01	0.02	0.03	nd	4.4	29.2	4.4	3.1	0.70560	
Spot #12	3902	8	57	1.11	1.58	nd	0.68	0.12	0.12	0.32	nd	0.04	0.01	0.02	0.02	nd	4.1	33.5	5.7	2.6	0.70566	
Spot #13	3527	28	38	1.38	2.12	nd	0.92	0.15	0.13	0.43	nd	0.07	0.01	0.03	0.03	nd	5.4	29.1	5.1	2.3	0.70561	
Snowcap, 193_1188F_16R_2, 109-111cm, 137mbsf																						
Spot #1	4494	597	169	0.47	1.09	nd	0.85	0.20	0.23	0.58	nd	0.12	0.03	0.08	0.09	nd	4.0	3.7	2.5	3.0	0.70589	
Spot #2	4297	40	92	0.44	0.78	nd	0.49	0.15	0.21	0.55	nd	0.29	0.07	0.19	0.15	nd	3.5	1.9	1.0	3.8	0.70571	
Spot #3	5054	34	122	1.20	2.57	nd	1.44	0.30	0.30	0.89	nd	0.24	0.06	0.18	0.09	nd	7.6	8.8	3.5	2.6	0.70566	
Spot #4	3569	12	54	1.17	2.80	nd	1.74	0.37	0.28	0.88	nd	0.15	0.02	0.05	0.03	nd	7.8	23.4	11.7	2.0	0.70601	
Spot #5	5203	28	125	0.85	1.63	nd	1.08	0.26	0.25	0.63	nd	0.13	0.02	0.04	0.03	nd	5.2	18.7	9.1	2.5	0.70633	
Spot #6	5573	23	122	0.30	0.58	nd	0.40	0.10	0.16	0.29	nd	0.06	0.01	0.02	0.02	nd	2.1	10.2	5.2	4.3	0.70623	
Spot #7	5962	13	108	1.77	3.13	nd	1.92	0.37	0.29	0.96	nd	0.16	0.02	0.05	0.03	nd	9.0	34.5	11.6	2.0	0.70607	
Spot #8	6175	11	242	1.51	3.06	nd	1.75	0.35	0.33	0.83	nd	0.16	0.02	0.05	0.04	nd	8.5	24.5	9.0	2.5	0.70587	

Table S1. Trace element (Sr, Mg, Ba, REE) and isotopic (Sr, S) compositions of anhydrites sampled in the Manus Basin, Papua New Guinea. Concentrations given in parts per million (ppm).

	Sr	Mg	Ba	La	Ce	Pr	Nd	Sm	Eu	Gd	Tb	Dy	Ho	Er	Yb	Lu	ΣREE	La _N /Yb _N	Sm _N /Yb _N	Eu _N /Eu* _N	⁸⁷ Sr/ ⁸⁶ Sr	δ ³⁴ S (‰)
Snowcap, 193_1188F_16R_2, 109-111cm, 137mbsf (continued)																						
Spot #9	6192	17	156	0.44	0.69	nd	0.38	0.08	0.16	0.26	nd	0.05	0.01	0.02	0.02	nd	2.3	16.2	4.7	5.2	0.70616	
Spot #10	7204	16	497	0.36	0.56	nd	0.29	0.06	0.17	0.21	nd	0.04	0.01	0.02	0.01	nd	2.0	19.3	4.8	8.1	0.70618	
Spot #11	5551	12	153	1.50	2.85	nd	1.76	0.34	0.29	0.84	nd	0.16	0.02	0.05	0.03	nd	8.2	33.9	12.2	2.2	0.70585	
Spot #12	7298	13	62	3.17	5.70	nd	3.11	0.54	0.34	1.46	nd	0.22	0.03	0.07	0.05	nd	15.0	46.6	12.5	1.7	0.70564	
Spot #13	2842	13	4	0.62	1.34	nd	1.00	0.23	0.17	0.50	nd	0.11	0.02	0.04	0.03	nd	4.2	14.6	8.7	2.0	0.70628	
Spot #14	6559	57	248	0.53	0.83	nd	0.49	0.10	0.20	0.26	nd	0.05	0.01	0.02	0.02	nd	2.8	16.2	4.7	5.6	0.70581	
Spot #15	5364	14	40	1.02	2.02	nd	1.13	0.22	0.16	0.56	nd	0.10	0.02	0.03	0.03	nd	5.5	27.6	9.4	1.9	0.70567	
Spot #16	3375	0	4	0.57	1.31	nd	0.81	0.18	0.12	0.45	nd	0.09	0.02	0.04	0.02	nd	3.7	20.4	9.9	1.8	0.70589	
Spot #17	5340	4	192	0.91	1.89	nd	1.18	0.24	0.21	0.62	nd	0.12	0.02	0.03	0.02	nd	5.5	27.3	11.2	2.3	0.70574	
Snowcap, 193_1188F_1Z_2, 32-34cm, 219mbsf																						
Spot #1	3133	20	103	0.05	0.17	nd	0.16	0.06	0.10	0.16	nd	0.08	0.01	0.03	0.02	nd	1.0	1.6	2.9	4.6	0.70718	20.7
Spot #2	3303	62	103	0.03	0.10	nd	0.13	0.05	0.11	0.10	nd	0.06	0.01	0.03	0.02	nd	0.8	1.2	2.9	6.1	0.70707	21.1
Spot #3	7267	21	453	0.07	0.20	nd	0.28	0.16	0.35	0.29	nd	0.29	0.05	0.11	0.07	nd	2.3	0.7	2.5	6.0	0.70663	20.9
Spot #4	3058	8	27	0.13	0.67	nd	1.13	0.63	0.48	0.95	nd	0.90	0.13	0.29	0.16	nd	5.8	0.6	4.3	2.0	0.70683	20.7
Spot #5	2329	16	25	0.05	0.37	nd	0.99	0.82	0.77	1.31	nd	1.34	0.20	0.46	0.28	nd	7.2	0.1	3.2	2.5	0.70625	20.5
Spot #6	2649	351	48	0.14	0.35	nd	0.47	0.29	0.22	0.43	nd	0.47	0.08	0.19	0.10	nd	2.9	1.0	3.1	2.0	0.70704	20.9
Spot #7	3128	92	82	0.05	0.27	nd	0.50	0.30	0.25	0.48	nd	0.50	0.08	0.18	0.09	nd	2.9	0.4	3.4	2.2	0.70700	
Spot #8	3795	38	20	0.11	0.58	nd	1.08	0.62	0.48	0.99	nd	0.90	0.14	0.32	0.18	nd	5.7	0.4	3.8	2.1		
Spot #9	4858	30	80	0.14	0.53	nd	0.71	0.31	0.23	0.46	nd	0.39	0.07	0.16	0.10	nd	3.3	0.9	3.3	2.0		
Spot #10	2696	118	27	0.04	0.27	nd	0.52	0.36	0.33	0.59	nd	0.64	0.10	0.22	0.13	nd	3.4	0.2	2.8	2.4		
Spot #11	3444	571	35	0.04	0.19	nd	0.30	0.18	0.15	0.24	nd	0.26	0.05	0.12	0.12	nd	1.8	0.2	1.5	2.3		
Spot #12	3473	13	43	0.07	0.30	nd	0.51	0.27	0.21	0.39	nd	0.50	0.08	0.18	0.10	nd	2.7	0.5	3.0	2.0		
Spot #13	4926	17	55	0.09	0.34	nd	0.54	0.39	0.35	0.64	nd	0.62	0.09	0.21	0.13	nd	3.7	0.5	3.2	2.4		
Spot #14	4424	209	43	0.04	0.15	nd	0.12	0.04	0.05	0.03	nd	0.05	0.01	0.02	0.01	nd	0.6	2.3	3.5	3.4	0.70643	
Spot #15	2903	20	68	0.20	1.41	nd	2.83	1.58	0.85	2.24	nd	2.32	0.37	0.86	0.45	nd	13.6	0.3	3.8	1.4	0.70662	
Spot #16	2459	44	50	0.07	0.56	nd	1.15	0.71	0.54	1.05	nd	1.04	0.16	0.35	0.18	nd	6.2	0.3	4.3	2.0	0.70710	
Spot #17	3000	784	86	0.04	0.25	nd	0.38	0.23	0.19	0.25	nd	0.30	0.06	0.17	0.23	nd	2.2	0.1	1.1	2.2	0.70703	
Spot #20	3659	314	57	0.04	0.17	nd	0.22	0.10	0.11	0.10	nd	0.16	0.02	0.06	0.04	nd	1.1	0.7	3.0	3.0	0.70694	
Spot #21	2744	6034	36	0.01	0.15	nd	0.20	0.11	0.11	0.10	nd	0.17	0.03	0.07	0.04	nd	1.1	0.1	3.2	2.6	0.70700	
Spot #22	3709	8	136	0.11	0.57	nd	0.83	0.46	0.48	0.75	nd	0.87	0.14	0.34	0.21	nd	5.2	0.3	2.4	2.8	0.70699	
Spot #23	2838	21	50	0.03	0.24	nd	0.33	0.19	0.18	0.24	nd	0.40	0.07	0.18	0.11	nd	2.1	0.2	1.9	2.5	0.70707	
Spot #24	4986	70	184	0.10	0.48	nd	0.68	0.34	0.34	0.55	nd	0.69	0.12	0.30	0.16	nd	4.0	0.5	2.4	2.6	0.70717	
Spot #25	2971	5	4	0.08	0.81	nd	2.00	1.60	1.37	2.25	nd	2.08	0.30	0.64	0.38	nd	12.6	0.1	4.5	2.3	0.70706	
Spot #26	2130	42	19	0.07	0.66	nd	1.57	0.87	0.50	1.10	nd	1.23	0.19	0.45	0.26	nd	7.2	0.2	3.6	1.5	0.70718	
Spot #27	3281	513	46	0.04	0.24	nd	0.46	0.36	0.42	0.31	nd	0.40	0.07	0.20	0.16	nd	3.1	0.2	2.5	3.1		
Spot #28	1916	807	31		0.11	nd	0.31	0.22	0.31	0.11	nd	0.17	0.03	0.09	0.09	nd	1.7		2.6	3.6		
Snowcap, 193_1188F_1Z_4, 100-104cm, 223mbsf																						
Spot #1	3635	26	77	7.36	16.29	nd	8.92	1.95	1.22	3.54	nd	1.89	0.36	0.96	0.70	nd	44.1	7.1	3.0	1.7	0.70525	
Spot #2	3816	42	64	5.19	11.73	nd	6.27	1.31	0.80	2.25	nd	1.20	0.23	0.64	0.47	nd	30.6	7.5	3.0	1.6	0.70567	
Spot #4	3557	3146	2655	11.40	26.87	nd	12.28	3.03	3.17	5.72	nd	4.28	0.99	2.96	3.17	nd	75.5	2.4	1.0	2.8	0.70538	
Spot #5	3127	563	482	6.60	18.74	nd	12.17	3.14	2.19	4.99	nd	3.67	0.71	1.91	1.50	nd	57.1	3.0	2.2	1.9	0.70521	
Spot #6	2465	726	705	2.84	9.46	nd	7.83	2.35	2.03	3.36	nd	3.15	0.60	1.61	1.09	nd	35.5	1.8	2.3	2.3		
Spot #7	2381	123	64	1.90	6.85	nd	6.26	1.83	1.10	2.55	nd	2.21	0.42	1.12	0.72	nd	25.6	1.8	2.7	1.6	0.70612	20.0
Spot #8	4699	30	13	102.73	264.36	nd	92.09	14.90	11.76	29.45	nd	10.92	2.03	5.33	3.65	nd	547.1	19.0	4.4	2.1		20.0
Spot #10	5126	17	66	29.88	75.01	nd	32.45	5.76	4.54	10.36	nd	3.67	0.64	1.59	1.08	nd	168.8	18.6	5.7	2.1	0.70559	20.5
Spot #11	4489	17	82	6.66	19.08	nd	15.21	4.08	2.46	5.72	nd	4.49	0.83	2.18	1.41	nd	63.6	3.2	3.1	1.6	0.70515	20.3
Spot #12	3637	14	60	38.52	103.90	nd	45.91	8.21	6.42	13.57	nd	5.06	0.92	2.40	2.09	nd	232.6	12.5	4.2	2.1	0.70545	19.9
Spot #14	2855	351	328	3.73	13.53	nd	11.76	3.72	2.43	5.14	nd	3.89	0.67	1.67	1.06	nd	49.3	2.4	3.8	1.7	0.70563	20.3
Spot #20	3261	50	67	4.95	13.66	nd	9.03	2.38	1.54	3.64	nd	2.79	0.53	1.40	0.96	nd	41.9	3.5	2.7	1.7		
Spot #21	2468	14	14	6.76	20.71	nd	16.91	4.18	2.23	5.86	nd	3.86	0.65	1.59	0.82	nd	65.1	5.6	5.5	1.4		

Table S1. Trace element (Sr, Mg, Ba, REE) and isotopic (Sr, S) compositions of anhydrites sampled in the Manus Basin, Papua New Guinea. Concentrations given in parts per million (ppm).

	Sr	Mg	Ba	La	Ce	Pr	Nd	Sm	Eu	Gd	Tb	Dy	Ho	Er	Yb	Lu	ΣREE	La _N /Yb _N	Sm _N /Yb _N	Eu _N /Eu* _N	⁸⁷ Sr/ ⁸⁶ Sr	δ ³⁴ S (‰)
Snowcap, 193_1188F_1Z_4, 100-104cm, 223mbsf (continued)																						
Spot #22	4476	19	5	74.87	191.54	nd	78.15	13.60	10.08	26.41	nd	10.51	1.92	5.02	3.28	nd	423.6	15.4	4.4	2.0		
Spot #23	4766	18	222	7.16	12.85	nd	5.36	0.86	1.73	1.64	nd	0.42	0.08	0.19	0.18	nd	32.0	27.5	5.2	5.3		
Spot #25	3624	809	755	3.85	11.43	nd	7.30	2.63	2.37	5.16	nd	4.32	0.71	1.71	1.05	nd	41.8	2.5	2.7	2.4		
Snowcap, 193_1188F_23Z_2, 22-26cm, 289mbsf																						
Spot #1	2989	33	103	1.49	4.43	nd	4.15	1.24	0.52	2.18	nd	1.48	0.31	0.87	0.69	nd	17.5	1.5	1.9	1.1	0.70698	
Spot #2	2443	17	33	2.29	6.42	nd	6.18	1.76	0.70	3.16	nd	2.18	0.46	1.32	1.11	nd	25.8	1.4	1.7	1.1	0.70697	
Spot #3	2761	42	64	3.16	9.12	nd	7.57	2.28	0.89	3.77	nd	2.46	0.48	1.32	1.03	nd	32.5	2.1	2.4	1.0	0.70659	
Spot #4	2688	121	140	1.98	5.80	nd	5.20	1.55	0.63	2.78	nd	1.98	0.40	1.12	0.99	nd	22.6	1.4	1.7	1.1	0.70673	
Spot #5	3347	275	185	3.94	10.50	nd	8.15	2.05	0.86	3.66	nd	2.04	0.41	1.15	0.93	nd	34.0	2.9	2.4	1.1	0.70686	
Spot #6	2494	9222	3340	20.34	42.30	nd	28.61	6.30	4.25	12.93	nd	5.06	0.97	2.59	2.34	nd	128.3	5.9	2.9	1.8	0.70630	
Snowcap, 193_1188F_26Z_1, 62-69cm, 300mbsf																						
Spot #1	2577	65	63	0.14	0.66	nd	1.05	0.64	0.91	0.72	nd	0.98	0.18	0.49	0.30	nd	6.8	0.3	2.2	3.8	0.70642	
Spot #2	2103	45	50	5.41	13.16	nd	6.70	1.49	1.13	4.00	nd	1.95	0.40	1.11	0.80	nd	36.9	4.5	2.0	2.0	0.70614	
Spot #3	2347	7	23	3.86	8.04	nd	5.28	1.49	1.28	3.47	nd	2.60	0.56	1.59	0.99	nd	29.9	2.6	1.6	2.3	0.70508	16.6
Spot #4	2209	194	134	6.18	12.00	nd	7.76	1.55	0.97	4.31	nd	2.09	0.48	1.43	1.38	nd	38.5	3.0	1.2	1.7	0.70546	
Spot #5	2832	99	89	3.36	7.78	nd	5.91	1.59	0.46	3.24	nd	1.58	0.32	0.89	0.70	nd	26.0	3.2	2.4	0.8	0.70694	
Spot #6	2821	185	155	1.33	3.26	nd	2.60	0.71	0.67	1.23	nd	1.08	0.21	0.56	0.31	nd	12.4	2.9	2.5	2.5	0.70635	
Spot #7	2566	1098	41	5.33	12.53	nd	11.05	3.38	1.63	6.06	nd	3.65	0.69	1.85	1.35	nd	48.4	2.7	2.7	1.3	0.70592	17.4
Spot #8	2991	29	41	1.41	3.44	nd	3.44	1.16	1.01	1.69	nd	1.12	0.21	0.54	0.35	nd	15.1	2.7	3.5	2.2	0.70596	
Spot #9	2103	19	53	3.02	5.52	nd	4.37	1.08	0.86	1.84	nd	0.42	0.07	0.16	0.15	nd	18.3	13.4	7.6	2.1	0.70583	
Spot #10	1393	20	12	2.04	5.11	nd	3.62	0.94	0.73	1.85	nd	1.72	0.34	0.93	0.56	nd	18.2	2.5	1.8	2.1	0.70623	
Spot #11	2468	20	73	6.15	15.75	nd	14.07	3.71	1.03	7.15	nd	3.63	0.64	1.62	1.13	nd	55.2	3.7	3.5	0.7	0.70626	
Spot #12	2442	356	205	0.37	0.82	nd	0.95	0.35	0.42	0.29	nd	0.23	0.04	0.11	0.11	nd	4.0	2.4	3.5	3.9	0.70712	18.6
Spot #13	3316	10	106	0.13	0.43	nd	0.56	0.28	0.60	0.15	nd	0.23	0.04	0.10	0.09	nd	3.2	0.9	3.2	5.7	0.70581	
Spot #14	2516	338	157	2.19	5.67	nd	4.97	1.40	1.20	2.25	nd	1.37	0.27	0.75	0.68	nd	21.6	2.2	2.2	2.3	0.70625	
Spot #15	1928	24	52	24.56	51.94	nd	46.97	11.86	3.92	22.93	nd	9.38	1.65	4.18	3.14	nd	182.9	5.3	4.0	0.9	0.70542	18.0
Spot #16	2304	25	64	4.85	15.05	nd	16.92	5.22	1.70	8.29	nd	5.65	1.10	2.97	2.39	nd	64.7	1.4	2.3	0.9	0.70606	19.0
Spot #17	2768	29	21	0.41	1.06	nd	1.30	0.35	0.29	0.40	nd	0.18	0.03	0.07	0.07	nd	4.4	4.0	5.5	2.2	0.70686	18.7
Spot #18	3380	11	46	0.12	0.38	nd	0.64	0.39	0.32	0.15	nd	0.17	0.03	0.06	0.04	nd	2.6	1.8	9.2	2.2	0.70699	
Spot #19	2080	39	115	4.07	7.65	nd	4.39	1.13	1.19	2.94	nd	2.62	0.55	1.58	1.02	nd	27.7	2.7	1.2	2.8	0.70542	
Spot #20	2561	193	126	2.08	5.58	nd	5.08	1.38	0.63	2.30	nd	1.54	0.31	0.87	0.76	nd	20.8	1.8	1.9	1.2	0.70663	
Spot #21	2060	14	23	1.48	4.39	nd	4.72	1.44	0.64	2.16	nd	1.75	0.38	1.11	1.35	nd	19.7	0.7	1.1	1.2	0.70648	
Spot #22	1691	9	18	2.06	5.21	nd	3.99	1.19	1.08	2.40	nd	2.79	0.59	1.67	1.02	nd	22.5	1.4	1.3	2.4	0.70635	
Spot #23	1789	224	142	3.41	7.17	nd	4.96	1.37	1.09	2.95	nd	2.32	0.47	1.33	0.84	nd	26.4	2.7	1.7	2.1	0.70633	
Spot #24	2547	59	42	0.29	0.85	nd	0.83	0.29	0.29	0.14	nd	0.19	0.03	0.07	0.06	nd	3.3	3.4	5.4	2.6	0.70613	
Roman Ruins, 193_1189A_3R_1, 89-93cm, 20mbsf																						
Spot #1	2989	4	197	3.27	9.93	nd	7.66	1.52	0.75	1.36	nd	0.48	0.07	0.14	0.08	nd	26.0	27.0	19.9	1.3	0.70576	20.2
Spot #2	4127	1	170	8.35	15.59	nd	6.19	1.00	0.48	1.25	nd	0.33	0.05	0.11	0.08	nd	33.9	74.2	14.0	1.3	0.70586	19.8
Spot #3	3391	1	108	3.74	7.78	nd	3.35	0.49	0.34	0.63	nd	0.17	0.03	0.07	0.04	nd	17.0	57.8	12.1	1.8	0.70623	20.0
Spot #4	3267	3	75	1.44	3.09	nd	1.39	0.23	0.23	0.26	nd	0.09	0.01	0.03	0.03	nd	7.0	35.6	9.0	2.7	0.70594	
Spot #5	1378	5	28	6.85	22.45	nd	12.42	2.18	1.24	2.24	nd	0.65	0.09	0.19	0.11	nd	49.5	41.9	21.2	1.5	0.70527	
Spot #6	1820	4	30	0.54	1.94	nd	1.27	0.22	0.51	0.24	nd	0.11	0.02	0.06	0.05	nd	5.5	7.8	5.1	6.1	0.70565	
Spot #7	1819	4	147	0.66	2.44	nd	2.26	0.51	0.47	0.46	nd	0.24	0.04	0.08	0.05	nd	7.7	8.3	10.2	2.4	0.70607	19.6
Spot #8	615	4	1	1.42	4.55	nd	2.57	0.47	0.24	0.48	nd	0.22	0.03	0.07	0.04	nd	10.3	23.4	12.2	1.3	0.70666	19.8
Spot #9	872	3	24	0.86	2.41	nd	1.24	0.23	0.13	0.23	nd	0.09	0.01	0.02	0.02	nd	5.4	38.8	16.2	1.5		19.8
Spot #10	807	1	4	1.05	3.84	nd	2.36	0.54	0.29	0.53	nd	0.24	0.03	0.06	0.04	nd	9.2	17.5	14.5	1.4		19.9
Spot #11	2077	14	37	16.17	33.10	nd	11.67	2.17	1.80	2.74	nd	0.67	0.09	0.19	0.10	nd	70.5	107.7	23.0	2.2	0.70628	
Spot #12	620	1	4	1.56	5.58	nd	4.06	1.11	0.37	1.06	nd	0.44	0.06	0.10	0.06	nd	14.7	19.1	21.6	0.9	0.70544	
Spot #13	908	2	8	2.48	6.90	nd	3.59	0.67	0.30	0.71	nd	0.23	0.03	0.07	0.04	nd	15.3	41.9	17.9	1.2	0.70583	
Spot #14	3335	5	56	6.87	13.54	nd	6.41	0.86	0.47	1.18	nd	0.31	0.05	0.10	0.07	nd	30.2	69.2	13.7	1.5	0.70667	

Table S1. Trace element (Sr, Mg, Ba, REE) and isotopic (Sr, S) compositions of anhydrites sampled in the Manus Basin, Papua New Guinea. Concentrations given in parts per million (ppm).

	Sr	Mg	Ba	La	Ce	Pr	Nd	Sm	Eu	Gd	Tb	Dy	Ho	Er	Yb	Lu	ΣREE	La _N /Yb _N	Sm _N /Yb _N	Eu _N /Eu* _N	⁸⁷ Sr/ ⁸⁶ Sr	δ ³⁴ S (‰)
Roman Ruins, 193_1189A_3R_1, 89-93cm, 20mbsf (continued)																						
Spot #15	4124	1	282	5.88	12.52	nd	5.20	0.78	0.49	1.02	nd	0.30	0.05	0.11	0.07	nd	26.9	56.7	12.0	1.7	0.70591	
Spot #16	2046	1	40	2.34	7.36	nd	4.15	0.78	0.29	0.79	nd	0.32	0.04	0.09	0.06	nd	16.5	26.0	13.8	1.0	0.70637	
Spot #17	1579	1	26	0.34	1.34	nd	0.98	0.19	0.46	0.17	nd	0.11	0.02	0.04	0.04	nd	4.1	5.9	5.2	6.5	0.70565	
Roman Ruins, 193_1189A_7R_1, 19-23cm, 58mbsf																						
Spot #1	1629	11	124	0.93	2.55	nd	2.28	0.61	0.50	0.84	nd	0.30	0.05	0.10	0.08	nd	8.7	8.2	8.5	2.1	0.70610	
Spot #2	1477	3	137	1.03	2.94	nd	2.62	0.71	0.51	0.98	nd	0.35	0.05	0.11	0.08	nd	9.8	8.7	9.5	1.9	0.70612	
Spot #3	1582	3	151	1.03	3.04	nd	2.80	0.77	0.50	0.98	nd	0.36	0.05	0.11	0.08	nd	10.2	8.5	10.1	1.8	0.70604	
Spot #4	1613	4	147	0.61	2.14	nd	2.60	0.72	0.63	0.91	nd	0.37	0.05	0.12	0.09	nd	8.8	4.6	8.6	2.4	0.70604	
Spot #5	3203	2	211	1.21	3.13	nd	2.72	0.62	0.71	0.91	nd	0.30	0.05	0.11	0.08	nd	10.5	10.2	8.3	2.9	0.70611	
Spot #6	1855	2	48	2.78	6.89	nd	5.15	1.33	0.71	1.88	nd	0.62	0.09	0.18	0.13	nd	20.4	14.3	10.8	1.4	0.70611	
Spot #7	1026	2	11	0.65	1.87	nd	1.46	0.39	0.21	0.54	nd	0.19	0.03	0.06	0.04	nd	5.6	10.8	10.3	1.4	0.70617	
Spot #8	1300	1	70	0.88	2.51	nd	1.82	0.50	0.28	0.70	nd	0.23	0.03	0.07	0.05	nd	7.3	11.7	10.4	1.4	0.70626	
Spot #9	1269	1	30	0.96	2.78	nd	2.04	0.56	0.28	0.73	nd	0.25	0.03	0.07	0.05	nd	8.0	12.0	11.2	1.3	0.70611	
Spot #10	1356	2	51	1.08	2.90	nd	2.12	0.57	0.29	0.80	nd	0.24	0.03	0.07	0.05	nd	8.4	14.9	12.5	1.3	0.70606	
Spot #11	1515	3	199	0.95	2.44	nd	1.67	0.43	0.38	0.61	nd	0.19	0.03	0.06	0.04	nd	7.1	16.3	11.7	2.3	0.70608	
Spot #12	1751	4	264	0.58	1.39	nd	0.99	0.27	0.41	0.39	nd	0.12	0.02	0.04	0.02	nd	4.5	16.2	11.7	3.8	0.70617	
Spot #13	1879	3	233	0.58	1.41	nd	0.94	0.27	0.42	0.36	nd	0.11	0.02	0.03	0.03	nd	4.5	14.4	10.6	4.1		
Spot #14	1996	4	131	0.66	1.62	nd	1.08	0.27	0.24	0.39	nd	0.12	0.02	0.03	0.02	nd	4.6	18.4	11.9	2.3	0.70637	
Spot #15	2950	1	127	2.99	7.30	nd	5.43	1.20	0.78	1.97	nd	0.48	0.07	0.15	0.11	nd	21.1	17.7	11.3	1.5	0.70601	
Spot #16	2063	2	165	7.26	14.36	nd	8.41	1.96	0.83	3.56	nd	0.81	0.11	0.22	0.16	nd	38.3	30.4	13.0	1.1	0.70552	
Spot #17	4624	2	678	2.11	4.85	nd	3.12	0.65	0.98	1.26	nd	0.28	0.04	0.09	0.07	nd	14.2	20.3	9.8	3.3	0.70624	
Spot #18	1429	4	98	1.28	3.97	nd	3.19	0.77	0.49	1.25	nd	0.36	0.05	0.11	0.09	nd	12.0	10.1	9.8	1.5	0.70626	
Spot #19	3942	24	35	0.23	0.45	nd	0.28	0.07	0.04	0.14	nd	0.03	0.00	0.01	0.01	nd	1.3	20.6	9.2	1.8	0.70809	
Spot #20	2088	6	48	0.05	0.11	nd	0.07	0.02	0.04	0.03	nd	0.01	0.00	0.00	0.00	nd	0.4	11.4	6.0	6.0	0.70787	
Spot #21	2429	7	29	0.10	0.20	nd	0.13	0.03	0.03	0.05	nd	0.01	0.00	0.00	0.00	nd	0.6	34.6	18.4	2.6	0.70796	
Spot #22	2769	4	14	0.28	0.54	nd	0.39	0.10	0.05	0.17	nd	0.04	0.01	0.01	0.01	nd	1.6	25.6	14.7	1.2	0.70824	
Spot #23	2962	11	27	1.46	3.24	nd	2.36	0.62	0.18	0.91	nd	0.28	0.04	0.07	0.05	nd	9.4	21.4	14.4	0.8	0.70739	
Spot #24	1445	37	24	2.90	8.44	nd	7.11	2.04	0.57	2.93	nd	0.88	0.12	0.23	0.16	nd	25.9	12.3	13.8	0.7	0.70617	
Spot #25	1449	84	35	3.33	9.28	nd	7.44	1.94	0.57	3.06	nd	0.82	0.11	0.22	0.17	nd	27.4	13.1	12.2	0.8	0.70689	
Spot #26	1521	15	34	2.18	7.12	nd	6.36	1.81	0.51	2.60	nd	0.73	0.10	0.18	0.14	nd	22.1	10.4	13.8	0.7	0.70728	
Spot #27	1256	32	12	2.26	7.33	nd	6.47	1.69	0.53	2.69	nd	0.72	0.10	0.20	0.14	nd	22.6	10.5	12.6	0.8		
Roman Ruins, 193_1189B_10R_1, 42-44cm, 118mbsf																						
Spot #1	3063	46	144	0.99	2.27	nd	1.75	0.42	0.18	0.60	nd	0.17	0.03	0.06	0.04	nd	6.6	17.8	11.9	1.1	0.70786	
Spot #2	2810	30	126	0.69	1.76	nd	1.30	0.34	0.16	0.46	nd	0.16	0.02	0.06	0.04	nd	5.1	11.5	9.0	1.2	0.70781	
Spot #3	2884	27	145	0.50	1.02	nd	0.70	0.16	0.13	0.22	nd	0.07	0.01	0.03	0.02	nd	3.0	17.5	9.1	2.0	0.70778	
Spot #4	2439	34	54	0.28	0.52	nd	0.34	0.09	0.07	0.13	nd	0.04	0.01	0.02	0.01	nd	1.6	18.6	9.6	2.0	0.70786	
Spot #5	1996	12	125	0.34	0.72	nd	0.48	0.13	0.12	0.17	nd	0.04	0.01	0.01	0.01	nd	2.1	22.3	13.5	2.4	0.70762	
Spot #6	2493	7	184	1.12	2.01	nd	1.23	0.27	0.21	0.45	nd	0.08	0.01	0.02	0.02	nd	5.6	39.0	14.9	2.0	0.70736	
Spot #7	2955	12	160	1.19	2.23	nd	1.28	0.28	0.18	0.54	nd	0.08	0.01	0.03	0.02	nd	6.0	40.9	15.3	1.7	0.70744	
Spot #8	2781	34	203	0.47	1.01	nd	0.71	0.17	0.20	0.31	nd	0.06	0.01	0.02	0.02	nd	3.1	17.1	10.0	3.1	0.70791	
Spot #9	3170	24	185	0.52	1.20	nd	1.08	0.28	0.17	0.35	nd	0.11	0.02	0.04	0.03	nd	3.9	12.6	10.8	1.6		
Spot #10	2629	14	19	0.29	0.62	nd	0.55	0.12	0.06	0.21	nd	0.05	0.01	0.02	0.02	nd	2.0	11.4	7.7	1.2	0.70808	
Spot #11	2928	17	112	0.62	1.57	nd	1.30	0.32	0.16	0.49	nd	0.13	0.02	0.03	0.03	nd	4.8	13.8	11.4	1.3		
Spot #12	3122	26	181	1.11	2.56	nd	2.07	0.51	0.24	0.80	nd	0.23	0.03	0.08	0.06	nd	7.9	12.4	9.0	1.3	0.70773	
Spot #13	2898	17	174	0.83	2.13	nd	1.74	0.43	0.22	0.65	nd	0.18	0.03	0.06	0.05	nd	6.5	11.5	9.4	1.4	0.70774	
Spot #20	2411	24	8	1.23	2.62	nd	1.56	0.34	0.15	0.70	nd	0.20	0.03	0.07	0.04	nd	7.0	20.3	8.9	1.1	0.70734	
Spot #21	2206	52	10	1.23	2.66	nd	1.66	0.36	0.16	0.71	nd	0.19	0.03	0.07	0.05	nd	7.2	16.9	7.9	1.2	0.70742	
Spot #22	2381	14	7	1.42	3.07	nd	2.07	0.43	0.19	0.87	nd	0.23	0.04	0.09	0.05	nd	8.6	19.3	9.2	1.2	0.70742	
Spot #23	2940	46	14	1.82	3.49	nd	2.00	0.41	0.18	1.01	nd	0.23	0.04	0.09	0.06	nd	9.5	19.7	7.0	1.2	0.70752	
Spot #24	2635	11	69	0.27	0.38	nd	0.22	0.05	0.06	0.10	nd	0.02	0.00	0.01	0.01	nd	1.2	30.4	8.2	3.5	0.70800	

Table S1. Trace element (Sr, Mg, Ba, REE) and isotopic (Sr, S) compositions of anhydrites sampled in the Manus Basin, Papua New Guinea. Concentrations given in parts per million (ppm).

	Sr	Mg	Ba	La	Ce	Pr	Nd	Sm	Eu	Gd	Tb	Dy	Ho	Er	Yb	Lu	ΣREE	La _N /Yb _N	Sm _N /Yb _N	Eu _N /Eu* _N	⁸⁷ Sr/ ⁸⁶ Sr	δ ³⁴ S (‰)
Roman Ruins, 193_1189B_10R_1, 42-44cm, 118mbsf (continued)																						
Spot #25	2746	19	62	0.48	0.77	nd	0.49	0.09	0.08	0.21	nd	0.03	0.00	0.01	0.01	nd	2.2	37.0	11.2	2.2		21.6
Spot #26	2984	36	59	0.44	0.64	nd	0.42	0.07	0.06	0.18	nd	0.03	0.00	0.01	0.01	nd	1.9	46.1	12.1	2.2	0.70811	
Spot #27	2999	29	58	0.27	0.35	nd	0.22	0.04	0.05	0.10	nd	0.01	0.00	0.00	0.00	nd	1.1	47.8	10.7	3.7	0.70802	
Spot #28	3285	38	202	1.00	2.54	nd	2.08	0.53	0.26	0.82	nd	0.22	0.03	0.07	0.05	nd	7.8	13.7	11.5	1.3	0.70774	21.5
Spot #29	3162	22	194	0.22	0.41	nd	0.31	0.08	0.14	0.13	nd	0.03	0.00	0.01	0.01	nd	1.4	12.8	7.2	4.9	0.70659	21.3
Roman Ruins, 193_1189B_14R_2, 0-3cm, 158mbsf																						
Spot #1	2856	10	187	0.44	1.03	nd	0.71	0.14	0.29	0.24	nd	0.06	0.01	0.02	0.01	nd	3.2	21.2	10.5	5.6	0.70628	20.9
Spot #2	2479	9	261	3.71	7.07	nd	3.57	0.65	1.06	1.33	nd	0.25	0.04	0.09	0.06	nd	18.7	41.2	11.5	4.3	0.70427	
Spot #3	785	3	26	9.56	30.63	nd	25.82	5.65	1.25	8.28	nd	2.03	0.28	0.56	0.38	nd	85.4	17.0	15.9	0.6	0.70432	21.0
Spot #5	447	4	1	10.39	37.67	nd	32.62	7.15	1.39	10.46	nd	2.63	0.36	0.71	0.46	nd	104.9	15.2	16.6	0.5	0.70727	20.2
Spot #6	2291	32	68	0.93	2.51	nd	1.97	0.44	0.33	0.66	nd	0.16	0.02	0.04	0.03	nd	7.4	24.8	18.7	2.0	0.70822	19.9
Spot #7	1445	6	43	2.06	7.44	nd	6.82	1.62	0.54	2.31	nd	0.68	0.10	0.21	0.14	nd	22.4	10.2	12.7	0.9	0.70429	21.2
Spot #9	686	1	15	10.11	33.58	nd	27.82	6.11	1.31	8.90	nd	2.31	0.32	0.63	0.42	nd	92.5	16.3	15.7	0.6	0.70804	22.8
Spot #10	443	1	1	6.38	23.15	nd	20.01	4.54	0.91	6.46	nd	1.75	0.25	0.51	0.33	nd	65.0	12.9	14.6	0.5	0.70748	23.2
Spot #11	545	10	8	7.00	24.63	nd	21.30	5.09	0.84	7.18	nd	2.05	0.28	0.57	0.38	nd	69.9	12.3	14.2	0.4		21.5
Spot #12	263	723	41	11.39	26.65	nd	13.87	2.26	0.59	4.73	nd	1.22	0.26	0.72	0.87	nd	62.9	8.9	2.8	0.7		21.4
Spot #13	1818	270	68	5.87	17.04	nd	13.52	2.75	0.72	4.08	nd	1.04	0.16	0.34	0.30	nd	46.4	13.2	9.8	0.7		22.1
Spot #14	1900	12	47	1.75	6.01	nd	5.31	1.22	0.63	1.68	nd	0.50	0.07	0.14	0.09	nd	18.0	13.7	15.2	1.4		21.2
Fenway, J2_210_8_R1																						
Spot #1	842	2	93	2.59	5.57	nd	1.93	0.35	1.37	0.23	nd	0.17	0.03	0.07	0.05	nd	13.7	33.2	7.2	13.9		
Spot #2	2258	5	33	1.61	4.31	nd	2.56	0.73	0.67	0.51	nd	0.29	0.04	0.08	0.05	nd	11.5	21.9	15.7	3.2		
Spot #3	1417	112	217	2.34	6.79	nd	5.18	1.43	1.11	1.17	nd	0.70	0.09	0.18	0.06	nd	20.1	27.1	26.4	2.5		
Spot #4	2762	39	161	2.35	4.72	nd	2.33	0.59	0.70	0.47	nd	0.35	0.06	0.13	0.05	nd	12.4	29.0	11.6	4.0		
Spot #5	2447	9	73	0.80	1.68	nd	0.98	0.21	0.33	0.17	nd	0.09	0.01	0.03	0.01	nd	4.6	36.5	15.5	5.1		
Spot #7	1911	10	118	1.19	2.64	nd	1.10	0.20	0.54	0.13	nd	0.15	0.02	0.04	0.03	nd	6.5	27.8	7.3	9.7		
Spot #8	1703	4	531	2.66	5.73	nd	2.67	0.61	0.65	0.41	nd	0.29	0.04	0.09	0.07	nd	13.8	26.5	9.6	3.8		
Spot #9	1372	12	455	3.20	6.59	nd	2.47	0.49	1.06	0.31	nd	0.20	0.04	0.12	0.04	nd	15.6	48.9	11.8	7.8		
Spot #10	1423	18	560	6.00	12.89	nd	5.15	1.08	1.43	0.70	nd	0.42	0.06	0.14	0.08	nd	29.3	48.3	13.9	4.7		
Spot #11	1216	43	396	10.08	23.91	nd	13.45	3.01	2.29	2.07	nd	1.15	0.16	0.31	0.17	nd	58.8	40.2	19.0	2.7		
Spot #12	1098	7	81	8.47	22.64	nd	11.47	2.50	2.89	1.68	nd	0.93	0.13	0.29	0.15	nd	54.0	37.1	17.4	4.1		
Spot #13	1831	81	514	3.74	6.51	nd	2.63	0.54	1.55	0.37	nd	0.18	0.04	0.10	0.04	nd	17.2	58.0	13.2	10.0		
Spot #14	1654	199	626	3.47	6.42	nd	2.42	0.52	1.59	0.30	nd	0.21	0.03	0.06	0.05	nd	16.5	50.6	12.0	11.3		
Spot #15	2829	7	102	0.92	1.79	nd	0.89	0.20	0.38	0.14	nd	0.08	0.01	0.06	0.01	nd	4.8	49.5	17.4	6.4		
Spot #16	2630	22	123	3.41	6.50	nd	2.48	0.33	0.87	0.29	nd	0.18	0.03	0.07	0.04	nd	15.0	57.4	8.8	8.5		
Spot #17	1509	42	28	0.97	2.33	nd	1.29	0.28	0.57	0.24	nd	0.13	0.10	0.04	0.01	nd	6.4	48.0	21.6	6.7		
Spot #18	1437	52	31	1.71	4.40	nd	2.54	0.58	0.81	0.34	nd	0.21	0.03	0.05	0.03	nd	11.4	36.5	19.6	5.2		
Spot #19	2867	91	59	0.76	1.49	nd	0.83	0.18	0.31	0.14	nd	0.10	0.01	0.03	0.02	nd	4.2	27.7	10.4	5.9		
Fenway, J2_210_8_R2																						
Spot #1	2449	8	45	0.66	1.81	nd	1.09	0.25	0.66	0.15	nd	0.10	0.02	0.04	0.03	nd	5.5	16.3	9.8	9.6	0.70694	21.0
Spot #2	2245	73	75	0.73	2.18	nd	1.26	0.33	0.59	0.19	nd	0.13	0.02	0.04	0.02	nd	6.1	29.6	21.0	6.7		
Spot #3	2517	89	88	0.92	2.08	nd	0.99	0.22	0.57	0.15	nd	0.09	0.01	0.03	0.02	nd	5.6	29.1	11.3	9.0	0.70757	
Spot #4	2819	66	73	1.47	3.22	nd	1.44	0.31	0.70	0.23	nd	0.15	0.02	0.05	0.04	nd	8.3	25.4	8.5	7.6	0.70768	
Spot #5	3669	14	67	0.44	1.05	nd	0.69	0.18	0.19	0.13	nd	0.08	0.01	0.04	0.02	nd	3.0	13.8	8.7	3.7		
Spot #6	2162	66	64	0.99	2.74	nd	1.53	0.35	0.70	0.23	nd	0.13	0.02	0.04	0.04	nd	7.4	18.8	10.5	7.2	0.70763	
Spot #7	1762	5	50	2.07	4.81	nd	2.26	0.48	0.65	0.31	nd	0.18	0.03	0.06	0.03	nd	11.6	40.7	15.0	4.8	0.70673	21.7
Spot #8	2178	6	212	1.27	3.04	nd	1.60	0.37	0.44	0.22	nd	0.13	0.02	0.04	0.02	nd	7.6	38.6	18.0	4.3		
Spot #9	2447	75	134	0.58	1.46	nd	0.84	0.21	0.26	0.17	nd	0.08	0.01	0.03	0.02	nd	3.9	25.9	15.1	4.1	0.70806	
Spot #10	3059	11	352	0.51	1.08	nd	0.56	0.13	0.22	0.09	nd	0.06	0.01	0.02	0.02	nd	2.9	19.1	7.4	6.1		
Spot #11	2420	11	83	0.26	0.59	nd	0.37	0.08	0.19	0.06	nd	0.04	0.01	0.02	0.02	nd	1.8	8.7	4.2	7.9	0.70803	
Spot #12	2403	7	37	0.87	2.47	nd	1.46	0.37	0.37	0.23	nd	0.15	0.02	0.04	0.02	nd	6.4	30.1	20.5	3.6	0.70790	

Table S1. Trace element (Sr, Mg, Ba, REE) and isotopic (Sr, S) compositions of anhydrites sampled in the Manus Basin, Papua New Guinea. Concentrations given in parts per million (ppm).

	Sr	Mg	Ba	La	Ce	Pr	Nd	Sm	Eu	Gd	Tb	Dy	Ho	Er	Yb	Lu	ΣREE	La _N /Yb _N	Sm _N /Yb _N	Eu _N /Eu* _N	⁸⁷ Sr/ ⁸⁶ Sr	δ ³⁴ S (‰)
Fenway, J2_210_8_R2 (continued)																						
Spot #13	2379	7	119	0.47	0.98	nd	0.48	0.12	0.24	0.10	nd	0.06	0.01	0.02	0.02	nd	2.7	18.2	7.5	6.5		
Spot #14	2231	2	200	0.42	1.08	nd	0.53	0.15	0.31	0.09	nd	0.08	0.01	0.03	0.02	nd	3.0	13.8	7.6	7.7	0.70752	
Spot #15	2082	32	59	1.50	3.18	nd	1.54	0.34	0.90	0.24	nd	0.15	0.02	0.05	0.03	nd	8.8	37.4	13.5	9.2		
Spot #16	3047	139	159	1.39	2.85	nd	1.47	0.33	0.49	0.23	nd	0.15	0.02	0.04	0.03	nd	7.4	33.7	12.6	5.2		
Spot #17	2192	91	136	0.74	2.08	nd	1.44	0.42	0.41	0.33	nd	0.20	0.03	0.06	0.04	nd	6.1	11.4	10.1	3.3		
Spot #18	2617	44	82	0.47	1.18	nd	0.67	0.14	0.15	0.11	nd	0.06	0.01	0.03	0.01	nd	3.0	24.3	11.4	3.6		
Spot #19	2977	59	428	2.98	6.00	nd	3.12	0.74	0.80	0.54	nd	0.30	0.04	0.08	0.06	nd	15.4	31.9	12.5	3.7		
Spot #20	2591	37	122	0.42	1.21	nd	0.66	0.17	0.37	0.12	nd	0.08	0.01	0.02	0.01	nd	3.5	19.2	11.9	7.6		21.8
Fenway, J2_212_7_R1																						
Spot #1	3185	7	73	0.81	1.98	nd	1.12	0.24	0.33	0.22	nd	0.13	0.02	0.04	0.04	nd	5.2	12.2	5.9	4.4		
Spot #2	2900	30	44	1.03	2.72	nd	1.72	0.42	0.49	0.32	nd	0.19	0.03	0.07	0.04	nd	7.5	19.2	12.3	3.9		
Spot #3	2968	9	63	0.55	1.39	nd	1.11	0.30	0.31	0.22	nd	0.12	0.02	0.03	0.05	nd	4.4	7.5	6.6	3.5		
Spot #4	3174	191	147	1.70	3.39	nd	1.51	0.28	0.82	0.24	nd	0.23	0.03	0.05	0.03	nd	9.1	33.5	8.8	9.4		
Spot #5	3286	12	31	1.31	2.54	nd	1.08	0.19	0.94	0.15	nd	0.08	0.01	0.11	0.03	nd	7.3	28.4	6.6	16.4		
Spot #7	3096	29	76	1.61	3.52	nd	2.15	0.64	0.71	0.41	nd	0.23	0.03	0.07	0.03	nd	10.1	32.7	20.6	4.0	0.70762	
Spot #10	3359	34	68	0.41	0.98	nd	0.67	0.25	0.25	0.15	nd	0.11	0.01	0.02	0.04	nd	3.1	7.3	7.0	3.7	0.70789	
Spot #11	2524	475	30	0.71	1.79	nd	1.02	0.26	0.59	0.20	nd	0.13	0.02	0.05	0.03	nd	5.3	17.6	10.2	7.6	0.70785	
Spot #12	1904	128	26	0.36	1.03	nd	0.74	0.33	0.63	0.26	nd	0.25	0.02	0.23	0.05	nd	4.5	5.0	7.2	6.4	0.70746	
Spot #16	2232	24	39	1.47	4.11	nd	3.13	0.92	0.85	0.58	nd	0.36	0.03	nd	0.12	nd	12.4	8.3	8.2	3.3	0.70697	
Spot #17	2893	85	37	0.67	1.97	nd	1.49	0.47	0.59	0.30	nd	0.18	0.03	0.08	0.02	nd	6.3	21.6	24.1	4.5		
Spot #18	3484	7	110	0.68	1.66	nd	1.04	0.28	0.40	0.20	nd	0.15	0.03	0.06	0.04	nd	4.9	11.8	7.8	4.9	0.70732	
Fenway, J2_216_1_R1																						
Spot #1	2181	4	30	0.31	0.84	nd	0.56	0.21	0.31	0.14	nd	0.09	0.02	0.04	0.04	nd	2.8	4.7	5.0	5.3	0.70788	
Spot #2	2499	2	26	1.37	3.53	nd	1.84	0.61	1.34	0.52	nd	0.50	0.08	0.18	0.11	nd	11.3	8.3	5.9	7.1		
Spot #3	3315	1	97	3.72	6.97	nd	2.64	0.68	0.96	0.36	nd	0.22	0.03	0.08	0.04	nd	16.4	64.2	18.6	5.4	0.70736	
Spot #4	3232	50	87	2.06	4.86	nd	2.55	0.59	0.96	0.40	nd	0.25	0.04	0.08	0.06	nd	12.7	24.0	10.9	5.8	0.70664	
Spot #5	2144	3	19	1.18	3.41	nd	2.32	0.65	0.66	0.43	nd	0.25	0.03	0.07	0.04	nd	9.7	18.2	16.1	3.6		
Spot #6	1995	5	13	1.20	3.13	nd	1.46	0.28	0.77	0.20	nd	0.12	0.02	0.05	0.05	nd	8.1	16.0	5.9	9.6	0.70689	
Spot #8	2503	57	24	0.82	2.65	nd	1.76	0.37	0.41	0.27	nd	0.16	0.02	0.05	0.02	nd	6.9	23.4	16.6	3.9		
Spot #9	2615	15	236	1.94	4.06	nd	2.06	0.50	0.45	0.31	nd	0.18	0.03	0.05	0.03	nd	10.0	51.4	20.8	3.3		
Spot #10	2420	6	32	0.78	2.11	nd	1.35	0.37	0.47	0.26	nd	0.15	0.02	0.05	0.03	nd	6.0	16.2	12.2	4.5		
Spot #11	2708	8	34	0.50	1.15	nd	0.75	0.26	0.39	0.15	nd	0.12	0.02	0.04	0.02	nd	3.7	17.0	14.1	5.5		
Spot #12	2640	2	55	1.03	2.83	nd	1.67	0.42	0.91	0.37	nd	0.14	0.03	0.10	0.07	nd	8.5	9.6	6.2	6.9		
Spot #13	2822	11	82	0.78	2.24	nd	1.78	0.63	1.21	0.67	nd	0.67	0.10	0.24	0.16	nd	9.6	3.2	4.1	5.7		
Spot #14	3351	7	45	0.70	1.81	nd	0.88	0.22	0.53	0.21	nd	0.15	0.02	0.05	0.04	nd	5.1	11.0	5.6	7.4		
Spot #15	2673	8	39	1.26	3.30	nd	2.20	0.56	0.56	0.37	nd	0.23	0.03	0.06	0.07	nd	9.2	11.9	8.4	3.6		
Spot #16	2669	5	76	0.82	2.29	nd	1.69	0.44	0.48	0.27	nd	0.18	0.03	0.06	0.05	nd	6.7	11.7	9.9	3.9		
Spot #17	2247	5	126	1.19	3.20	nd	2.27	0.66	0.60	0.43	nd	0.28	0.04	0.08	0.04	nd	9.3	19.7	17.2	3.3		
Spot #18	2715	18	51	0.45	1.08	nd	0.67	0.19	0.35	0.13	nd	0.09	0.01	0.03	0.02	nd	3.4	13.6	9.1	6.6		
Spot #19	2486	10	34	0.74	1.81	nd	0.99	0.24	0.50	0.18	nd	0.13	0.02	0.03	0.04	nd	5.1	11.3	5.9	7.0		
Spot #20	2224	6	5469	2.73	5.53	nd	2.29	0.43	1.67	0.33	nd	0.23	0.04	0.12	0.09	nd	15.0	21.0	5.3	13.0	0.70686	
Spot #21	1980	7	18	1.93	4.62	nd	2.45	0.58	1.03	0.33	nd	0.24	0.04	0.10	0.07	nd	12.4	19.3	9.2	6.6		
Spot #22	1755	5	42	1.62	4.59	nd	3.02	0.80	1.00	0.59	nd	0.34	0.05	0.11	0.12	nd	13.1	9.2	7.2	4.3	0.70740	
Spot #23	2367	5	86	1.16	3.58	nd	2.68	0.82	0.59	0.60	nd	0.33	0.05	0.09	0.05	nd	10.5	17.3	19.4	2.5	0.70766	
Spot #24	2929	43	2017	1.48	2.95	nd	1.84	0.46	0.61	0.32	nd	0.20	0.03	0.05	0.03	nd	8.6	31.8	15.8	4.6		
Spot #25	2760	51	165	0.63	1.48	nd	0.83	0.23	0.69	0.15	nd	0.10	0.02	0.05	0.04	nd	4.9	11.2	6.3	10.8	0.70602	
Fenway, J2_216_5_R1																						
Spot #1	2038	19	227	1.65	3.85	nd	2.17	0.50	0.50	0.35	nd	0.23	0.03	0.07	0.04	nd	9.9	29.4	14.1	3.5	0.70672	
Spot #2	2537	8	77	0.87	2.34	nd	1.41	0.34	0.40	0.28	nd	0.16	0.02	0.05	0.04	nd	6.2	14.9	9.2	4.0		
Spot #3	1922	7	49	1.19	3.59	nd	2.67	0.85	0.58	0.59	nd	0.36	0.05	0.09	0.06	nd	10.6	12.8	14.5	2.4		

Table S1. Trace element (Sr, Mg, Ba, REE) and isotopic (Sr, S) compositions of anhydrites sampled in the Manus Basin, Papua New Guinea. Concentrations given in parts per million (ppm).

	Sr	Mg	Ba	La	Ce	Pr	Nd	Sm	Eu	Gd	Tb	Dy	Ho	Er	Yb	Lu	ΣREE	La _N /Yb _N	Sm _N /Yb _N	Eu _N /Eu* _N	⁸⁷ Sr/ ⁸⁶ Sr	δ ³⁴ S (‰)
Fenway, J2_216_5_R1 (continued)																						
Spot #4	2299	16	70	1.21	3.57	nd	2.84	0.75	0.77	0.60	nd	0.31	0.04	0.06	0.05	nd	10.9	17.2	17.0	3.4	0.70685	
Spot #6	1674	9	18	2.44	6.39	nd	3.99	1.12	1.08	0.77	nd	0.48	0.07	0.14	0.09	nd	17.6	19.3	14.1	3.4	0.70714	
Spot #7	1980	7	65	0.76	1.78	nd	1.03	0.31	0.30	0.21	nd	0.13	0.02	0.04	0.02	nd	4.9	25.0	16.3	3.4	0.70754	
Spot #8	2123	2	99	0.92	2.25	nd	1.35	0.28	0.41	0.23	nd	0.14	0.02	0.04	0.04	nd	6.1	15.5	7.6	4.7	0.70749	
Spot #9	2291	4	143	0.54	1.31	nd	0.81	0.21	0.37	0.12	nd	0.09	0.01	0.03	0.01	nd	3.8	25.7	15.9	6.6		
Spot #11	2657	4	148	1.00	2.03	nd	0.72	0.14	0.37	0.13	nd	0.07	0.01	0.01	0.01	nd	4.9	56.9	12.9	8.3		
Spot #13	3131	9	89	0.90	2.33	nd	1.36	0.46	0.60	0.20	nd	0.14	0.02	0.05	0.02	nd	6.7	35.3	28.6	5.2		
Spot #14	2581	21	125	0.79	1.84	nd	0.80	0.21	0.30	0.11	nd	0.06	0.01	0.03	0.02	nd	4.5	29.2	12.3	5.5		
Spot #15	2004	4	94	0.80	1.94	nd	1.03	0.25	0.32	0.17	nd	0.10	0.01	0.03	0.02	nd	5.0	34.2	17.1	4.6	0.70730	
Spot #16	2165	3	34	0.56	1.43	nd	0.86	0.18	0.31	0.14	nd	0.10	0.01	0.02	0.02	nd	3.9	24.1	12.5	5.8		
Spot #17	2128	6	38	0.81	2.01	nd	1.11	0.26	0.32	0.16	nd	0.12	0.02	0.05	0.02	nd	5.2	31.1	15.7	4.5	0.70742	
Spot #18	3015	7	60	1.02	2.20	nd	0.96	0.25	0.43	0.14	nd	0.07	0.01	0.04	0.03	nd	5.5	20.9	8.1	6.6		
Spot #19	2713	4	37	0.72	1.81	nd	1.06	0.32	0.50	0.20	nd	0.12	0.02	0.04	0.02	nd	5.3	27.7	19.5	5.6	0.70713	
Spot #20	2255	8	254	1.02	2.23	nd	1.07	0.26	0.41	0.14	nd	0.10	0.02	0.05	0.01	nd	5.7	46.3	19.0	5.9		
Spot #21	2017	11	150	1.41	3.63	nd	1.75	0.40	0.47	0.27	nd	0.16	0.02	0.05	0.03	nd	8.6	33.0	14.7	4.1		
Spot #22	2969	11	57	1.07	2.41	nd	1.37	0.35	0.34	0.18	nd	0.13	0.02	0.05	0.05	nd	6.3	14.6	7.6	3.7		
Spot #23	2310	3	31	1.98	5.94	nd	3.41	0.80	0.70	0.58	nd	0.31	0.04	0.08	0.08	nd	14.5	16.8	10.7	3.0	0.70725	
Spot #24	2146	4	55	0.81	2.26	nd	1.24	0.33	0.39	0.21	nd	0.12	0.02	0.05	0.02	nd	5.8	25.4	16.4	4.2		
Spot #25	2618	4	60	1.14	2.89	nd	1.51	0.40	0.42	0.30	nd	0.16	0.02	0.05	0.03	nd	7.3	22.9	12.9	3.5	0.70745	
Spot #26	2346	2	209	0.60	1.55	nd	0.96	0.34	0.27	0.18	nd	0.12	0.02	0.04	0.02	nd	4.4	25.7	22.8	3.0		
Spot #27	1983	5	59	0.66	2.15	nd	1.58	0.48	0.75	0.32	nd	0.21	0.03	0.05	0.03	nd	7.0	12.9	15.0	5.6	0.70802	
Spot #28	2156	5	35	0.86	2.12	nd	1.03	0.27	0.30	0.25	nd	0.13	0.02	0.04	0.02	nd	5.3	33.0	16.3	3.5		
Spot #29	2207	5	58	0.75	1.77	nd	0.94	0.23	0.24	0.17	nd	0.11	0.01	0.03	0.01	nd	4.5	35.0	16.8	3.7		
Spot #30	3194	7	56	1.89	4.45	nd	2.15	0.46	0.48	0.31	nd	0.16	0.03	0.06	0.04	nd	10.5	28.8	11.2	3.7		
Spot #31	2638	5	136	1.58	3.42	nd	1.78	0.42	0.50	0.28	nd	0.17	0.03	0.05	0.04	nd	8.7	28.8	12.2	4.1		
Spot #32	2919	3	91	2.83	5.46	nd	2.20	0.39	0.70	0.25	nd	0.18	0.03	0.07	0.05	nd	12.9	38.5	8.5	6.4		
Fenway, J2_216_12_R1																						
Spot #1	2746	197	35	0.73	2.14	nd	1.44	0.40	0.81	0.30	nd	0.18	0.03	0.07	0.05	nd	6.9	10.5	9.1	6.9	0.70816	
Spot #2	2544	14	27	0.64	1.74	nd	0.95	0.23	0.47	0.16	nd	0.10	0.02	0.03	0.02	nd	4.9	27.6	15.9	7.1		
Spot #3	2377	71	2361	1.01	2.02	nd	1.09	0.31	0.43	0.21	nd	0.11	0.02	0.04	0.02	nd	5.6	41.8	20.0	5.0	0.70797	
Spot #4	1774	70	239	1.06	2.29	nd	1.06	0.24	0.51	0.15	nd	0.10	0.01	0.02	0.02	nd	5.9	43.8	15.7	7.6	0.70716	
Spot #5	2726	140	62	1.61	3.93	nd	2.36	0.61	0.65	0.42	nd	0.22	0.03	0.06	0.03	nd	10.5	35.8	21.5	3.7		
Spot #6	1435	70	21	2.73	8.52	nd	4.97	1.21	1.26	0.80	nd	0.46	0.06	0.12	0.06	nd	21.5	31.4	22.2	3.7	0.70683	
Spot #7	2100	11	32	1.07	3.41	nd	2.40	0.66	0.90	0.44	nd	0.25	0.03	0.06	0.02	nd	10.1	30.1	29.3	4.8		
Spot #8	2547	4	39	0.16	0.29	nd	0.11	0.02	0.08	0.04	nd	0.04	0.02	0.01	0.02	nd	2.5				0.70819	
Spot #9	2493	44	45	0.68	1.82	nd	1.23	0.35	0.71	0.23	nd	0.15	0.02	0.04	0.03	nd	5.9	14.7	12.0	7.2		
Spot #10	2575	50	45	0.56	1.47	nd	0.84	0.27	0.62	0.23	nd	0.16	0.03	0.06	0.05	nd	4.9	7.0	5.3	7.5		
Spot #11	3074	23	66	0.98	2.46	nd	1.40	0.36	0.73	0.24	nd	0.14	0.02	0.05	0.04	nd	7.1	18.5	10.9	7.1		
Spot #12	2812	8	118	2.15	4.06	nd	1.78	0.43	0.84	0.25	nd	0.12	0.02	0.04	0.04	nd	10.5	35.0	11.1	7.2		
Spot #13	3705	20	99	1.51	3.37	nd	1.70	0.42	0.76	0.21	nd	0.16	0.02	0.04	0.03	nd	8.9	35.8	15.9	6.9		
Spot #14	1618	2	59	1.35	4.31	nd	3.23	0.88	1.13	0.57	nd	0.32	0.05	0.10	0.05	nd	13.0	19.8	20.5	4.6		
Spot #15	1747	6	25	0.66	2.46	nd	1.90	0.58	0.62	0.37	nd	0.20	0.03	0.08	0.04	nd	7.5	12.0	17.0	3.8		
Spot #16	3331	4	94	2.19	5.85	nd	3.64	0.93	0.86	0.64	nd	0.30	0.04	0.08	0.04	nd	15.4	36.1	24.2	3.2		
Spot #17	2563	8	143	1.29	2.95	nd	1.78	0.38	0.56	0.27	nd	0.16	0.03	0.07	0.04	nd	8.0	24.6	11.5	5.1		
Spot #18	2411	15	30	0.60	1.63	nd	0.98	0.28	0.59	0.18	nd	0.12	0.03	0.07	0.03	nd	5.1	14.4	10.4	7.6		
Spot #19	2177	72	78	0.37	1.19	nd	0.95	0.28	0.61	0.20	nd	0.12	0.02	0.06	0.03	nd	4.4	9.1	10.7	7.6		
Spot #20	2676	39	84	0.64	1.58	nd	0.81	0.23	0.35	0.15	nd	0.09	0.01	0.03	0.02	nd	4.2	26.8	15.0	5.4		
Spot #21	2771	226	54	1.32	4.09	nd	2.73	0.72	1.07	0.41	nd	0.26	0.03	0.06	0.03	nd	11.8	26.6	23.1	5.5		
Spot #22	2630	20	81	0.59	1.55	nd	0.91	0.21	0.32	0.14	nd	0.10	0.01	0.03	0.02	nd	4.2	22.1	12.5	5.4		
Spot #23	2782	7	134	1.53	4.02	nd	2.39	0.66	0.52	0.41	nd	0.21	0.03	0.07	0.04	nd	10.4	23.1	15.8	2.9		

Table S1. Trace element (Sr, Mg, Ba, REE) and isotopic (Sr, S) compositions of anhydrites sampled in the Manus Basin, Papua New Guinea. Concentrations given in parts per million (ppm).

	Sr	Mg	Ba	La	Ce	Pr	Nd	Sm	Eu	Gd	Tb	Dy	Ho	Er	Yb	Lu	ΣREE	La _N /Yb _N	Sm _N /Yb _N	Eu _N /Eu* _N	⁸⁷ Sr/ ⁸⁶ Sr	δ ³⁴ S (‰)
Fenway, J2_216_12_R1 (continued)																						
Spot #24	2469	4	72	1.69	4.46	nd	2.65	0.66	0.83	0.41	nd	0.25	0.03	0.07	0.04	nd	11.8	27.5	16.9	4.6		
Spot #25	3605	1	125	1.83	4.71	nd	2.76	0.72	0.90	0.41	nd	0.19	0.03	0.07	0.03	nd	12.5	35.5	22.2	4.6		
Spot #27	2178	5	37	0.57	1.68	nd	1.09	0.33	0.49	0.22	nd	0.13	0.02	0.03	0.04	nd	5.1	9.0	8.3	5.2		
Spot #29	2350	4	44	0.41	0.82	nd	0.47	0.11	0.25	0.09	nd	0.07	0.01	0.03	0.04	nd	2.5	6.9	3.0	7.3		
Spot #31	2780	13	505	0.52	1.56	nd	0.94	0.28	0.53	0.19	nd	0.10	0.02	0.04	0.02	nd	4.7	19.3	16.3	6.7		
Fenway, J2_216_14_R1																						
Spot #1	2065	55	379	0.37	1.38	nd	0.78	0.24	0.79	0.13	nd	0.09	0.02	0.05	0.02	nd	4.5	10.5	10.7	12.7		
Spot #2	1488	23	105	0.86	3.21	nd	1.66	0.41	1.51	0.28	nd	0.15	0.02	0.06	0.03	nd	9.6	21.8	16.7	12.9	0.70635	22.0
Spot #3	2305	81	192	0.56	1.79	nd	1.23	0.29	0.98	0.22	nd	0.13	0.02	0.05	0.05	nd	6.3	7.4	6.0	11.5		
Spot #4	2537	86	358	0.64	1.98	nd	1.35	0.39	1.26	0.26	nd	0.16	0.02	0.05	0.04	nd	7.4	10.9	10.6	11.4	0.70592	
Spot #5	2971	336	113	0.91	2.44	nd	1.29	0.28	0.67	0.22	nd	0.13	0.02	0.04	0.02	nd	6.6	26.4	12.8	8.0	0.70679	
Spot #6	2365	160	325	0.40	1.20	nd	0.88	0.20	0.73	0.17	nd	0.11	0.02	0.04	0.02	nd	4.4	17.7	14.2	11.8		
Spot #7	2401	239	171	0.60	1.80	nd	1.23	0.32	1.00	0.25	nd	0.19	0.02	0.04	0.12	nd	6.6	17.2	14.5	10.5	0.70600	
Spot #8	2693	5	234	1.12	3.65	nd	2.45	0.55	1.32	0.36	nd	0.26	0.04	0.09	0.04	nd	11.2	21.6	16.9	8.5		
Spot #9	2048	111	481	0.90	3.47	nd	2.80	0.81	1.57	0.47	nd	0.26	0.03	0.06	0.03	nd	11.9	19.3	27.6	7.2		
Spot #10	2068	7	242	0.93	3.85	nd	2.95	0.74	1.57	0.54	nd	0.27	0.04	0.08	0.05	nd	12.6	12.2	15.5	7.2		
Spot #11	1851	105	410	0.35	1.20	nd	0.75	0.21	0.75	0.11	nd	0.08	0.01	0.01	0.02	nd	4.2	11.9	11.3	13.7	0.70592	
Spot #12	2202	314	496	0.86	3.32	nd	2.25	0.66	1.16	0.36	nd	0.17	0.02	0.05	0.03	nd	10.2	20.2	24.6	6.7		
Spot #16	2398	3	110	1.09	2.31	nd	0.85	0.42	0.67	0.16	nd	0.08	0.01	0.04	0.05	nd	6.4	14.4	8.9	6.6	0.70642	20.1
Spot #17	1624	7	44	0.53	0.90	nd	0.23	0.09	0.55	0.05	nd	0.05	0.02	0.05	0.03	nd	3.1	11.1	3.1	22.6		
Spot #18	1352	28	72	0.59	1.57	nd	0.63	0.14	0.84	0.10	nd	0.07	0.01	0.03	0.02	nd	4.8	20.2	7.4	21.0		
Spot #20	3509	9	165	1.86	3.45	nd	0.89	0.16	0.56	0.12	nd	0.10	0.02	0.08	0.03	nd	7.8	39.2	5.3	12.0		
Spot #21	2157	115	73	3.43	6.64	nd	1.37	0.23	1.60	0.17	nd	0.07	0.01	0.04	0.03	nd	15.1	76.0	8.2	23.7	0.70641	
Spot #22	2315	2	31	0.31	0.97	nd	0.46	0.10	0.55	0.06	nd	0.03	0.01	0.02	0.01	nd	3.0	21.6	11.2	20.5		
Spot #23	2348	0	52	1.25	3.18	nd	0.68	0.09	1.58	0.05	nd	0.04	0.01	nd	0.03	nd	8.5	29.6	3.4	65.9	0.70571	
Spot #24	3546	2	181	0.32	0.41	nd	0.14	0.04	0.15	0.02	nd	0.01	0.00	0.00	0.01	nd	1.3	29.7	5.6	15.4	0.70589	
Spot #25	2343	0	68	0.74	1.16	nd	0.33	0.05	0.50	0.06	nd	0.03	0.01	0.02	0.02	nd	3.4	30.6	3.4	28.1		
Spot #26	1898	31	88	1.82	4.90	nd	1.69	0.38	1.08	0.22	nd	0.16	0.02	0.05	0.04	nd	11.3	31.9	10.6	10.4	0.70632	20.2
Spot #27	1263	54	126	0.86	2.35	nd	0.73	0.22	0.84	0.07	nd	0.05	0.01	0.02	0.05	nd	6.0	12.3	5.0	16.1		
Spot #28	2041	109	181	0.11	0.19	nd	0.09	0.19	0.25	0.02	nd	0.02	0.01	0.01	0.01	nd	1.2	5.1	13.8	6.6	0.70568	
Spot #29	1777	13	139	0.35	0.98	nd	0.39	0.06	0.37	0.04	nd	0.06	0.01	0.01	nd	nd	2.6	nd	nd	22.3		
Spot #30	4990	5	109	0.13	0.46	nd	0.38	0.12	0.13	0.13	nd	0.18	0.04	0.13	0.11	nd	1.9	0.8	1.2	3.0	0.70630	
Spot #31	2610	167	441	1.10	4.09	nd	2.78	0.66	1.23	0.43	nd	0.27	0.04	0.07	0.04	nd	11.8	17.5	16.8	6.6		
Spot #32	2801	137	349	1.14	3.91	nd	2.52	0.59	1.09	0.40	nd	0.26	0.04	0.08	0.04	nd	11.2	18.4	15.0	6.5		
Spot #33	2624	216	522	0.58	1.93	nd	1.35	0.32	0.76	0.23	nd	0.14	0.02	0.06	0.07	nd	6.2	5.7	5.0	8.3		
Spot #34	2428	99	394	0.42	1.49	nd	1.12	0.32	0.74	0.21	nd	0.15	0.02	0.06	0.05	nd	5.2	6.3	7.5	8.3		
Spot #35	1849	94	198	0.38	1.22	nd	0.89	0.24	0.78	0.17	nd	0.14	0.02	0.04	0.04	nd	4.7	6.1	6.1	11.1		
Spot #36	2440	123	70	0.23	0.76	nd	0.63	0.16	0.55	0.08	nd	0.08	0.01	0.03	0.02	nd	3.1	9.1	10.3	12.9		
Spot #38	2115	29	117	0.23	1.11	nd	1.70	0.46	1.91	0.28	nd	0.17	0.03	0.06	0.04	nd	7.9	4.2	13.0	15.2	0.70639	
Spot #39	3395	24	93	1.94	3.27	nd	1.34	0.32	0.51	0.17	nd	0.12	0.02	0.04	0.02	nd	8.3	61.9	16.0	6.0	0.70686	
Spot #40	2154	4	82	1.01	3.31	nd	2.24	0.60	0.99	0.37	nd	0.22	0.03	0.06	0.02	nd	9.8	30.6	28.8	6.0		
Spot #41	2000	15	94	0.83	2.73	nd	2.17	0.54	1.05	0.39	nd	0.31	0.03	0.04	0.02	nd	9.2	31.3	32.6	6.7	0.70633	
Spot #42	2124	44	207	0.25	0.74	nd	0.62	0.17	0.63	0.17	nd	0.08	0.01	0.02	0.02	nd	3.3	8.0	8.9	11.2		
Spot #43	2159	70	102	0.70	2.22	nd	1.37	0.37	0.63	0.23	nd	0.11	0.02	0.03	0.02	nd	6.3	22.7	19.1	6.2	0.70733	
Spot #44	2015	13	78	0.58	1.60	nd	0.99	0.24	0.39	0.17	nd	0.09	0.01	0.03	0.02	nd	4.5	15.7	10.3	5.7		
Spot #45	2090	14	378	0.37	1.32	nd	0.98	0.26	0.66	0.16	nd	0.10	0.01	0.03	0.01	nd	4.5	16.9	18.8	9.3	0.70736	
North Su, J2_227_7_R2																						
Spot #1	5826	31	57	0.25	0.46	nd	0.20	0.02	0.03	0.08	nd	0.06	0.02	0.05	0.04	nd	1.2	4.2	0.6	2.0	0.70805	22.4
Spot #3	3626	111	107	nd	nd	nd	nd	nd	nd	nd	nd	nd	nd	nd	nd	nd	nd	nd	nd	nd	0.70845	23.6
Spot #4	3539	17	50	0.33	1.11	nd	0.89	0.27	0.16	0.31	nd	0.37	0.07	0.19	0.16	nd	3.9	1.4	1.8	1.6	0.70763	23.2

Table S1. Trace element (Sr, Mg, Ba, REE) and isotopic (Sr, S) compositions of anhydrites sampled in the Manus Basin, Papua New Guinea. Concentrations given in parts per million (ppm).

	Sr	Mg	Ba	La	Ce	Pr	Nd	Sm	Eu	Gd	Tb	Dy	Ho	Er	Yb	Lu	ΣREE	La _N /Yb _N	Sm _N /Yb _N	Eu _N /Eu* _N	⁸⁷ Sr/ ⁸⁶ Sr	δ ³⁴ S (‰)
North Su, J2_227_7_R2 (continued)																						
Spot #5	2342	9	13	0.07	0.34	nd	0.54	0.21	0.17	0.32	nd	0.26	0.05	0.14	0.08	nd	2.3	0.6	2.8	1.9		22.5
Spot #8	2799	3	39	1.58	7.43	nd	10.85	4.79	2.77	4.99	nd	4.65	0.74	1.75	1.12	nd	42.7	1.0	4.6	1.7		
Spot #9	2255	1	192	1.39	4.73	nd	5.01	1.90	1.20	1.98	nd	2.02	0.39	1.04	1.16	nd	21.7	0.8	1.8	1.9		
Spot #10	3967	1	758	2.36	5.40	nd	3.61	1.15	0.72	1.22	nd	1.27	0.28	0.79	1.00	nd	18.2	1.6	1.2	1.8		
Spot #11	3009	5	583	1.68	3.85	nd	2.55	0.68	0.48	0.78	nd	1.04	0.24	0.72	0.90	nd	13.1	1.3	0.8	2.0		
Spot #12	3885	1	898	3.02	7.16	nd	5.08	1.59	1.09	1.81	nd	1.83	0.37	1.04	1.10	nd	24.8	1.8	1.5	2.0	0.70649	
Spot #13	3872	23	33	0.25	0.62	nd	0.58	0.21	0.25	0.31	nd	0.36	0.08	0.25	0.14	nd	3.2	1.2	1.6	3.0	0.70640	
Spot #14	3989	10	73	1.48	5.99	nd	7.46	2.67	1.40	2.74	nd	2.47	0.46	1.21	0.83	nd	27.6	1.2	3.4	1.6		
Spot #15	3621	20	90	0.70	2.86	nd	3.73	1.48	0.81	1.64	nd	1.67	0.32	0.84	0.64	nd	15.2	0.7	2.5	1.6	0.70675	
Spot #16	3543	14	81	1.56	7.07	nd	9.60	3.78	2.21	3.55	nd	3.30	0.54	1.27	0.80	nd	35.4	1.3	5.1	1.8		
Spot #17	3650	0	118	0.58	1.71	nd	1.45	0.61	0.64	0.79	nd	0.91	0.18	0.49	0.49	nd	8.3	0.8	1.3	2.8	0.70627	
Spot #18	2748	15	44	0.62	1.72	nd	2.98	1.31	0.83	2.55	nd	3.64	0.83	2.44	2.36	nd	19.3	0.2	0.6	1.4	0.70675	
Spot #19	3218	12	714	0.17	0.48	nd	0.56	0.25	0.22	0.44	nd	0.49	0.11	0.31	0.31	nd	3.4	0.4	0.9	2.0		
Spot #20	3092	14	505	0.15	0.41	nd	0.44	0.20	0.18	0.26	nd	0.32	0.06	0.16	0.14	nd	2.4	0.7	1.5	2.4	0.70578	
Spot #21	3226	9	102	0.15	0.46	nd	0.45	0.23	0.19	0.30	nd	0.36	0.07	0.20	0.17	nd	2.7	0.6	1.4	2.2	0.70600	
Spot #22	2963	2	95	0.17	0.82	nd	1.25	0.58	0.29	0.75	nd	0.91	0.18	0.51	0.44	nd	6.1	0.3	1.4	1.4		
Spot #23	3301	1	89	0.51	1.54	nd	1.09	0.29	0.22	0.37	nd	0.44	0.10	0.28	0.31	nd	5.3	1.1	1.0	2.1	0.70679	
Spot #24	3495	1	34	0.18	0.54	nd	0.58	0.29	0.37	0.40	nd	0.53	0.12	0.35	0.31	nd	3.9	0.4	1.0	3.3		
Spot #25	4166	0	69	0.32	0.91	nd	0.99	0.35	0.52	0.55	nd	0.75	0.16	0.45	0.45	nd	5.8	0.5	0.8	3.6	0.70624	
Spot #26	4632	2	111	0.16	0.50	nd	0.40	0.12	0.11	0.17	nd	0.21	0.05	0.15	0.12	nd	2.1	0.9	1.1	2.4		
Spot #28	4371	29	159	0.10	0.31	nd	0.28	0.13	0.13	0.17	nd	0.20	0.04	0.10	0.11	nd	1.7	0.6	1.3	2.7		
Spot #29	3393	76	117	0.06	0.26	nd	0.29	0.13	0.16	0.18	nd	0.22	0.05	0.13	0.11	nd	1.7	0.4	1.3	3.2	0.70818	
Spot #30	3644	31	105	0.05	0.20	nd	0.22	0.08	0.10	0.14	nd	0.16	0.04	0.10	0.14	nd	1.3	0.3	0.6	2.7		
Spot #31	3124	16	59	0.07	0.24	nd	0.30	0.13	0.08	0.19	nd	0.20	0.04	0.12	0.14	nd	1.6	0.3	1.0	1.5		
Spot #32	3425	8	74	0.18	0.81	nd	1.16	0.45	0.39	0.62	nd	0.69	0.14	0.39	0.35	nd	5.4	0.4	1.4	2.3	0.70736	
Spot #33	3533	4	40	0.22	1.01	nd	1.36	0.54	0.53	0.83	nd	0.84	0.18	0.53	0.46	nd	6.8	0.3	1.3	2.4		
Spot #34	4456	3	55	0.28	1.31	nd	1.93	0.69	0.44	0.79	nd	0.79	0.15	0.39	0.32	nd	7.4	0.6	2.3	1.8	0.70734	
Spot #35	3213	10	53	0.17	0.79	nd	1.08	0.44	0.35	0.51	nd	0.59	0.11	0.30	0.25	nd	4.8	0.4	1.8	2.3		
Spot #36	3153	38	77	0.09	0.29	nd	0.36	0.21	0.58	0.26	nd	0.29	0.05	0.14	0.14	nd	2.9	0.4	1.7	7.6		
Spot #37	2413	5	35	0.08	0.30	nd	0.32	0.22	0.76	0.38	nd	0.42	0.08	0.19	0.16	nd	3.6	0.3	1.5	8.0	0.70671	
Spot #38	2859	8	56	0.12	0.40	nd	0.46	0.32	1.17	0.56	nd	0.53	0.09	0.24	0.22	nd	5.2	0.4	1.6	8.4	0.70461	
Spot #39	2787	12	67	0.09	0.28	nd	0.17	0.20	0.59	0.31	nd	0.33	0.06	0.16	0.13	nd	2.9	0.4	1.7	7.2		
Spot #40	2140	1	55	0.26	0.97	nd	0.90	0.44	0.61	0.66	nd	0.73	0.16	0.46	0.51	nd	6.1	0.3	0.9	3.4	0.70729	
Spot #41	4316	38	217	0.38	1.23	nd	1.17	0.43	0.43	0.56	nd	0.59	0.12	0.33	0.37	nd	5.9	0.7	1.2	2.7		
Spot #42	3283	7	182	0.16	0.70	nd	1.04	0.46	0.26	0.51	nd	0.58	0.12	0.34	0.31	nd	4.6	0.3	1.6	1.6		
Spot #44	3632	11	94	0.87	3.27	nd	3.17	1.13	0.60	1.27	nd	1.33	0.27	0.76	0.64	nd	13.6	0.9	1.9	1.5		
Spot #45	3876	3	124	0.11	0.67	nd	1.94	0.95	0.47	1.12	nd	1.19	0.23	0.60	0.52	nd	8.1	0.1	2.0	1.4		
Spot #46	3586	22	80	0.94	3.60	nd	3.55	1.38	0.69	1.54	nd	1.72	0.33	0.89	0.75	nd	15.7	0.9	2.0	1.4		
Spot #47	4491	5	161	0.07	0.67	nd	2.69	1.44	0.69	1.49	nd	1.49	0.26	0.66	0.48	nd	10.4	0.1	3.2	1.4		
Spot #48	2833	76	233	0.11	0.34	nd	0.33	0.17	0.18	0.23	nd	0.25	0.05	0.12	0.13	nd	2.0	0.6	1.3	2.9	0.70649	
Spot #49	4583	10	190	0.17	0.67	nd	1.01	0.35	0.23	0.53	nd	0.70	0.14	0.37	0.42	nd	4.6	0.3	0.9	1.6	0.70643	
Spot #51	3394	5	69	0.16	0.71	nd	0.96	0.39	0.26	0.44	nd	0.46	0.09	0.22	0.19	nd	4.0	0.6	2.2	1.9	0.70771	
Spot #52	1691	2	6	0.08	0.36	nd	0.49	0.24	0.69	0.52	nd	0.54	0.12	0.35	0.23	nd	4.2	0.2	1.1	5.9	0.70456	
Spot #53	1887	0	24	0.10	0.40	nd	0.56	0.44	1.40	0.71	nd	0.66	0.12	0.30	0.27	nd	6.3	0.3	1.8	7.6	0.70477	
Spot #54	1306	1	45	0.03	0.11	nd	0.14	0.11	0.39	0.30	nd	0.40	0.07	0.19	0.13	nd	2.2	0.2	0.9	6.2	0.70569	
Spot #55	1503	2	10	0.12	0.57	nd	0.84	0.51	0.41	0.81	nd	0.92	0.19	0.52	0.55	nd	5.7	0.1	1.0	2.0	0.70783	
Spot #56	3965	573	100	1.20	4.69	nd	5.02	1.95	1.63	2.43	nd	2.51	0.48	1.27	1.27	nd	23.5	0.6	1.6	2.3	0.70604	
Spot #57	3712	85	50	0.83	3.51	nd	3.86	1.37	1.03	1.78	nd	1.64	0.31	0.84	0.66	nd	16.5	0.8	2.2	2.0		
Spot #58	4807	11	59	1.45	5.27	nd	5.78	2.02	1.24	2.11	nd	2.21	0.40	1.04	0.80	nd	23.2	1.2	2.7	1.8	0.70631	
Spot #59	4097	15	27	0.24	0.77	nd	0.76	0.27	0.24	0.37	nd	0.41	0.07	0.19	0.09	nd	3.6	1.7	3.1	2.3		